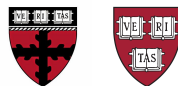


**Linking Climate Change with  
Ozone Loss over the US in Summer:  
New Instrument for the Detection of HCl in the Stratosphere**



Harvard University  
ES96 Spring 2016

Charles Alver, Rosa Bonilla, Kairn Brannon, James Conatser, Jon Cruz, Nick Holmes, Adam Jiang, Jack Kelly, Brian Krentz, Michael Lessard, Stancellous Matoreva, Tim McNamara, Vinh Nguyen, Carolina Pena, Dhruv Pillai, Eric Rodrigo, Dallas Schray, Simon Shuham, Jüri-Mikk Udam, Daniel Wang, Charles Wehr

## TABLE OF CONTENTS

<u>SECTION</u>	<u>PAGE</u>
TABLE OF CONTENTS .....	
<b>1. SCOPE</b>	
<b>1.1 Purpose.....</b>	<b>5</b>
<b>1.2 Applicability.....</b>	<b>5</b>
<b>2. GENERAL SCIENTIFIC REQUIREMENTS</b>	
<b>2.1 General environmental conditions.....</b>	<b>6</b>
2.1.1                 Chemical composition	
2.1.2                 Temperature	
2.1.3                 Pressure	
2.1.5                 Moisture	
<b>2.2 HCl molecular characteristics.....</b>	<b>7</b>
2.2.1                 Atomic structure	
2.2.2                 Atomic Energy and IR spectrum	
2.2.3                 Reactivity	
2.2.4                 Stratospheric mixing ratio	
<b>2.3 Stratospheric ozone depletion.....</b>	<b>9</b>
2.3.1                 Antarctic ozone hole	
2.3.1.1                 Mechanism	
2.3.2                 Arctic measurements	
2.3.2.1                 Adapted mechanism	
2.3.3                 Conditions for chlorine activation	
2.3.3.1                 Sulfate aerosols	
2.3.3.2                 Temperature	
2.3.3.3                 Water vapour concentration	
<b>2.4 Scientific background.....</b>	<b>14</b>
2.4.1                 Convective storms	
2.4.1.1                 NEXRAD	
2.4.2                 Anticyclonic monsoon flow	
2.4.3                 Current observations	

2.4.4	Verifying the chemistry with observations	
<b>2.5</b>	<b>ASC<sup>5</sup>ENA Proposal.....</b>	<b>17</b>
2.5.1	Long Duration Pumpkin Balloon	
2.5.2	Stratocruiser Drive Module	
2.5.3	Suspended Payload	
<b>2.6</b>	<b>System Overview.....</b>	<b>19</b>
2.6.1	Introduction to Molecular Detection Method	
2.6.2	Instrument Sensitivity and Performance	
2.6.3	Accuracy and Precision	
2.6.4	Integrated Cavity Output Spectroscopy (ICOS) System Diagram	
2.6.4.1	Laser and Fore-optics	
2.6.4.2	Cavity	
2.6.4.3	Pump System	
2.6.4.3	Detector System	
2.6.4.4	Flight Computer	

### 3. ENGINEERING DESIGN SPECIFICATIONS

<b>3.1</b>	<b>System-wide requirements.....</b>	<b>23</b>
3.1.1	Payload integration	
3.1.2	Power, Mass, and Volume Budgets	
3.1.3	Flight software and data storage	
3.1.3.1	System inputs and outputs	
<b>3.2</b>	<b>Flow Control System Design.....</b>	<b>26</b>
3.2.1	Pump	
3.2.1.1	Pump Design Requirements	
3.2.1.1.1	Flow Rate	
3.2.1.1.2	Vacuum Pressure	
3.2.1.1.3	Maximum Pressure Differential	
3.2.1.1.4	Power Usage	
3.2.1.1.5	Weight Limit	
3.2.1.1.6	Motor Type	
3.2.1.1.7	Flow Type	
3.2.1.2	Pump Selection	
3.2.1.3	Pump Testing	
3.2.2	Tubing	

3.2.2.1	Port connections
3.2.3	Orifice Control
3.2.3.1	Ball valve
3.2.3.2	Servo motor
3.2.3.3	Feedback and Control
3.2.4	Temperature Control
3.2.4.1	Heating element
3.2.4.2	Feedback and Control
<b>3.3</b>	<b>ICOS Cavity Design and Optics .....49</b>
3.3.1	ICOS system
3.3.1.1	Effective pathlength
3.3.1.2	Mirror reflectivity
3.3.1.3	Optical configuration
3.3.1.4	Optics specifications and re-injection
3.3.2	Cavity
3.3.2.1	Material & Structure
3.3.2.2	Coating & Bonding
3.3.2.3	Size
3.3.3	End caps
3.3.3.1	Structure
3.3.3.2	Materials
3.3.3.3	Sealing
3.3.3.4	Sealing test
3.3.3.5	Interface with cavity
3.3.4	Ports and sensors
3.3.4.1	Inlets & outlets
3.3.4.2	Temperature sensor (exterior)
3.3.4.3	Cavity heating
3.3.4.4	Temperature sensors (interior)
3.3.4.5	Pressure sensor
<b>3.4</b>	<b>ICOS Laser and Forward Optics</b>
3.4.1	Laser Wavelength Choice
3.4.2	Laser Choice
3.4.2.1	Collimator
3.4.3	Forward Optics
3.4.3.1	Telescope
3.4.3.2	Polarizer and Quarter Wave Plate

3.4.3.3	Beam Splitter	
3.4.3.4	Cage System	
3.4.4	Laser Driver	
3.4.4.1	Design and Schematic	
3.4.4.2	PCB Layout	
<b>3.5</b>	<b>Detector Systems.....</b>	<b>83</b>
3.5.1	Subsystems	
3.5.1.1	Optical Alignment	
3.5.2	Etalon Detector	
3.5.2.1	Design Requirements	
3.5.2.1.1	Wavelength Sensitivity	
3.5.2.1.2	Speed	
3.5.2.2	Detector Selection	
3.5.2.3	Characterization	
3.5.3	Post-Cavity Detector	
3.5.3.1	Design Requirements	
3.5.3.1.1	Wavelength Sensitivity	
3.5.4.1.2	Speed	
3.5.3.2	Detector Selection	
3.5.3.3	Characterization	
3.5.3.4	Signal Amplification	
3.5.3.4.1	Design Schematic	
3.5.3.4.2	Condensed Schematic	
3.5.3.5	Thermal Management	
3.5.3.6	Post-Cavity Optics	
<b>4.</b>	<b>IMPROVEMENTS AND NEXT STEPS</b>	
<b>4.1</b>	<b>Improvements.....</b>	<b>95</b>
<b>4.2</b>	<b>Future Steps.....</b>	<b>95</b>
<b>5.</b>	<b>APPENDIX</b>	
<b>5.1</b>	<b>Endcap Drawings.....</b>	<b>97</b>

# AIRBORNE HCl DETECTION UNIT

## 1. SCOPE

### 1.1 Purpose

The purpose of this documentation is to establish requirements and technical standards for design and fabrication of a flight instrument to measure atmospheric hydrochloric acid (HCl) concentrations. The flight instrument is to be integrated to assist the Airborne Stratospheric Climate Coupled Convective Catalytic Chemistry Experiment North America (ASC<sup>5</sup>ENA) mission and future programs/projects in providing robust, reliable, maintainable, supportable, and cost-effective atmospheric HCl measurements.

### 1.2 Applicability

**NASA Commercial Applications.** The standards and guidelines described hereinafter are applicable to integration within the Airborne Stratospheric Climate Coupled Convective Catalytic Chemistry Experiment North America (ASC<sup>5</sup>ENA) mission proposed by Aurora Flight Sciences and Harvard University. The StratoCruiser will be useful for a broad array of scientific studies dealing with the climate, atmospheric chemistry, weather, land usage, and astronomy.

## 2. GENERAL SCIENTIFIC REQUIREMENTS

### 2.1 General environmental conditions

The stratosphere is a cold region of the atmosphere (~215K) with a small temperature gradient (especially in the lower stratosphere), that remains relatively dry due to the lack of weather penetration. Our instrument will have to be able to withstand these conditions along with a low pressure as well as conditions associated with a convective storm penetrating the lower stratosphere.

#### 2.1.1 Chemical composition

The chemical composition of the stratosphere is very similar to the troposphere with most of the air being present as  $N_2$  (78%) or  $O_2$  (21%). But these are stable gases, and our instrument has to be able to detect trace amount of HCl without interference. This means it will have to be unreactive with HCl while ensuring that it can withstand all other trace gases, such as Argon,  $NO_x$ ,  $SO_x$ , Helium, Methane, Hydrogen, etc.

#### 2.1.2 Temperature

The temperature range that our system will have to endure ranges from the maximum it will see on the ground to the lowest it will see in the atmosphere. The highest it will see on the ground is ~322K and the lowest it will see is at the tropopause, which is ~200K. Our system must be able to survive in these temperatures plus some additional safety factor for abnormal conditions.

#### 2.1.3 Pressure

As pressure decreases exponentially with height, the system must be able to operate at the highest altitude the system will reach. If the system operates between the region of 10-25 km then the pressure will range from ~265-25 mbar. Since this range is an overestimate, if it can operate in these conditions as well as withstand ground pressure of 1014 mbar, then it will be sufficient.

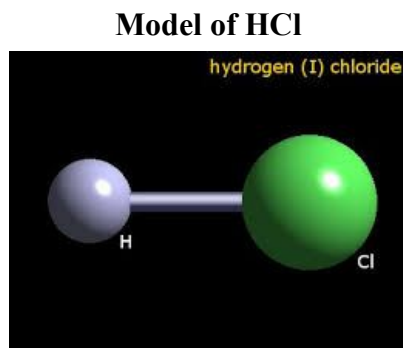
#### 2.1.4 Moisture

Gaseous H<sub>2</sub>O concentrations are extremely low in the lower stratosphere. Studies using balloon-borne frost point balloon across an expansive geographic range have shown mixing ratios as low as  $2 \times 10^{-6}$ . Through observations, we have seen that the usual concentration of water vapour is 5 ppmv which is then used as a background concentration value in simulations.

## 2.2 HCl molecular characteristics

### 2.2.1 Atomic structure

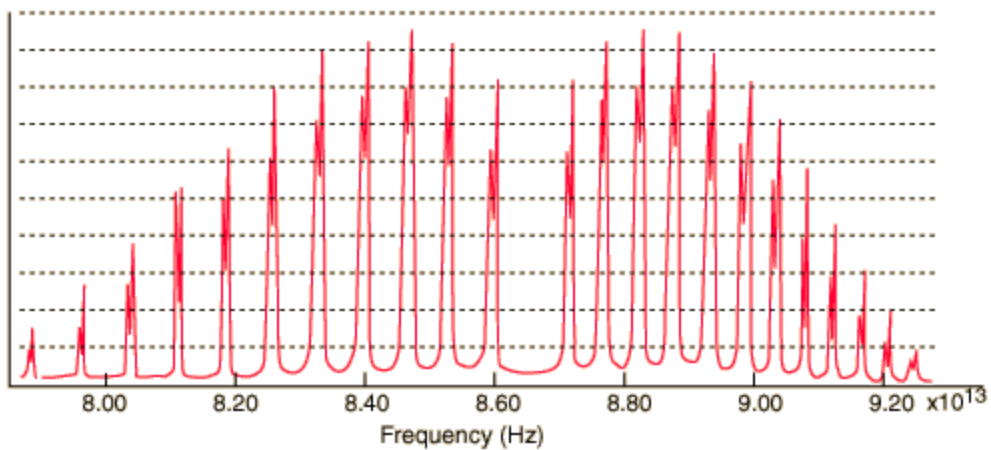
Hydrogen Chloride (HCl) is a single molecule of covalently bonded Hydrogen and Chlorine with a bond length of 127.4 pm. The molecule also has a dipole moment of 1.05D, with a partial negative charge on the chlorine and partial positive charge on the hydrogen. This is caused by the difference in the electronegativities of Chlorine (3.16D) and Hydrogen (2.20D) atoms individually.



[https://www.webelements.com/\\_media/compounds/H/Cl1H1-7647010.jpg](https://www.webelements.com/_media/compounds/H/Cl1H1-7647010.jpg)

### 2.2.2 Atomic Energy and IR spectrum

**IR Vibration and Rotation Spectrum of HCl**



<http://hyperphysics.phy-astr.gsu.edu/hbase/molecule/vibrot.html>

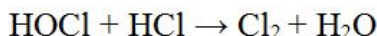
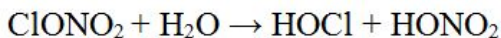
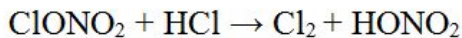
Vibration and rotational energy of the bond in HCl can be used to gain information about the chemical species and identify it in mixtures of molecules. Absorption lines in the IR spectra represent the bond energy of a molecule. Incident light to the bond gets absorbed when it matches the energy of the bond, elevating the energy level of the bond. The elevated bond then releases the energy and returns to its base energy level. The H-Cl bond in HCl has a specific set

of absorption lines based on the energy of this bond. As such its relative occurrence in the atmosphere can be observed by IR spectroscopy of atmospheric air.

### 2.2.3 Reactivity

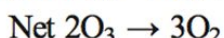
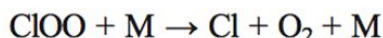
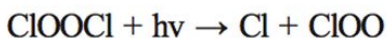
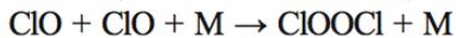
HCl by itself is not reactive in the conversion of O<sub>3</sub> into O<sub>2</sub>. Instead it relies on a variety of other atmospheric chemical species to be converted into a more reactive form—Cl. Chlorine nitrate (ClONO<sub>2</sub>) along with HCl, are the key reactants in the generation of active inorganic chlorine. In the atmosphere, HCl reacts directly with chlorine nitrate to form Cl<sub>2</sub> and nitric acid (HONO<sub>2</sub>). Chlorine nitrate indirectly affects HCl conversion through another reaction in which chlorine nitrate reacts with water vapor to create hypochlorous acid as well as nitric acid. The hypochlorous acid is then able to react with HCl forming Cl<sub>2</sub> and water vapor. These reactions are limited by their requirement of occurring on a particulate surface, such as sulfates. Cl<sub>2</sub> must then be photolyzed in order to split the diatomic chlorine and generate the chlorine radicals that will react to convert O<sub>3</sub> to O<sub>2</sub>.

#### Summary of Reaction Pathway to Reactive Chlorine Radicals



Chlorine radicals formed in the activation pathway are then able to interact with O<sub>3</sub> (ozone) to form chlorine monoxide (ClO) as well as O<sub>2</sub>. ClO collides with another molecule of ClO and a third body in order to form a ClO dimer (ClOOCl). The third body allows this reaction to proceed by serving as a sink for the ClO particle's momentum. The ClO dimer can be photolyzed to free a chlorine radical and generate ClOO. This particle can then be split apart into a chlorine radical and O<sub>2</sub>. This reaction pathway is catalytic; the only species that is consumed by the reaction is the O<sub>3</sub> molecules, while the chlorine radicals are regenerated.

#### Summary of Catalytic Conversion of O<sub>3</sub> to O<sub>2</sub> with Chlorine Radicals



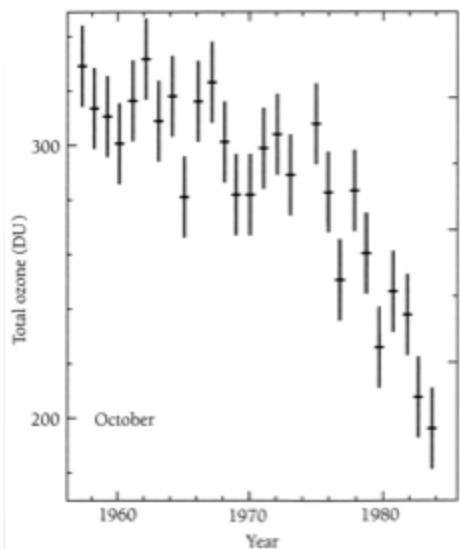
## 2.2.4 Stratospheric mixing ratio

Current research has shown the unperturbed stratosphere to have HCl mixing ratios of around 900 pptv. However, it is theorized and predicted by computer models that changes to atmospheric conditions can drop this to around 200 pptv.

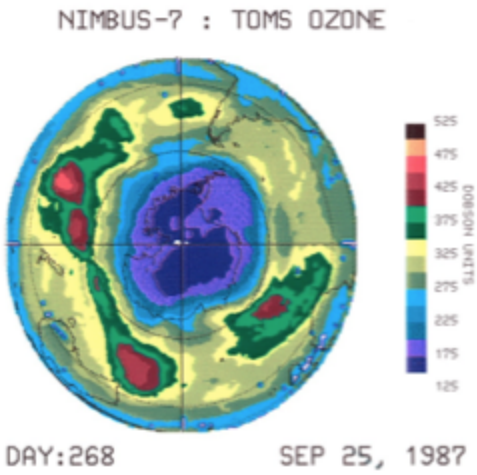
## 2.3 Stratospheric ozone depletion

### 2.3.1 Antarctic ozone hole

In the early 1980s, the Antarctic Ozone hole was first noticed by on ground observations taken by the British Antarctic Survey. The data from this can be seen in the image below:

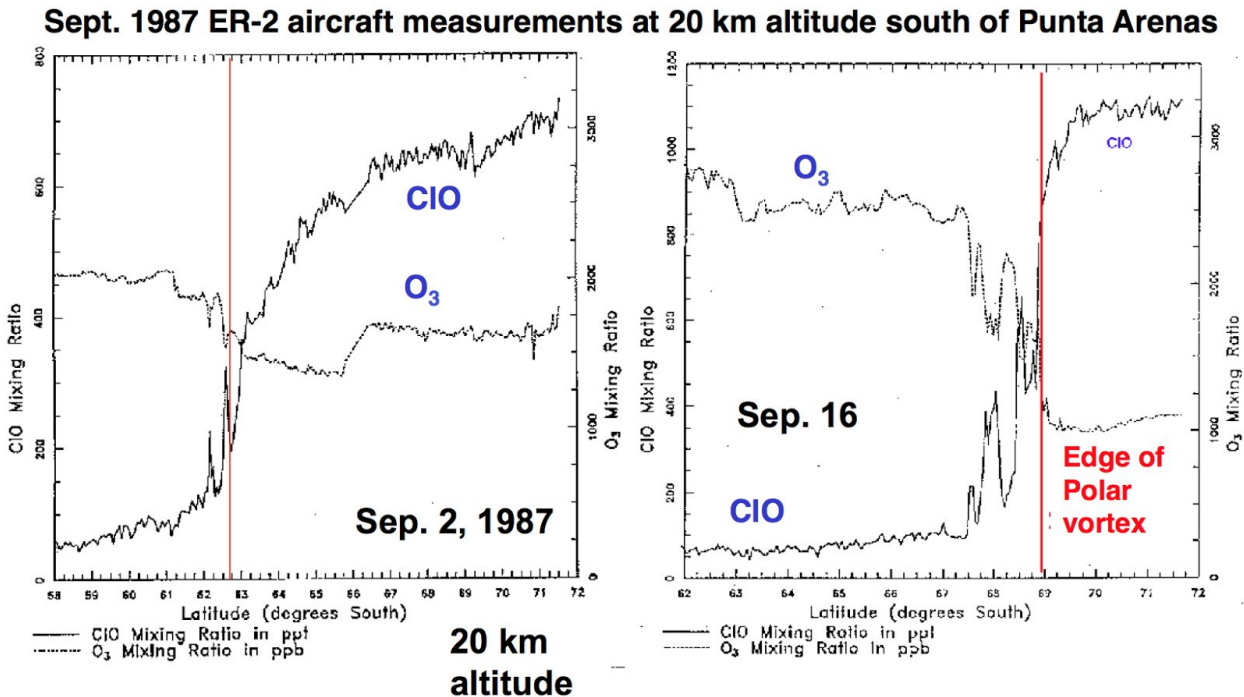


As it turns out, NASA had this data available to them from their satellite monitoring the Antarctic but had not processed the data and reported the ozone depletion. However, once the ozone hole was reported in Nature in 1985, this information was then confirmed by the NASA satellite data:



### 2.3.1.1 Mechanism

After discovery of the Antarctic ozone hole, a lot of research went into defining the mechanism for this destruction and finding the most critical molecules that control it. Professor Jim Anderson from Harvard and his group took in situ measurements in an ER-2 aeroplane over the area in 1987, which resulted in defining chlorine as the most important molecule in the ozone destruction cycle. This was demonstrated by the direct anticorrelation between the concentration of ClO and ozone:

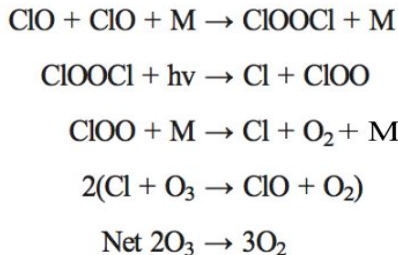


The significance of the polar vortex here was that the proposed mechanism was said to have been occurring only on polar stratospheric clouds (PSCs). The PSCs provide ice crystals to

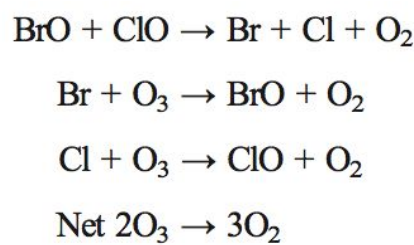
concentrate chlorine reservoirs and increase the rate of reactions converting them to  $Cl_2$  which then can be photolysed to form chlorine radicals and ultimately ClO. The conversion of heterogeneous chlorine to radical chlorine mechanism was defined as:

While the chlorine and bromine catalytic ozone destruction cycles were identified as:

**Catalytic Cycle 1**

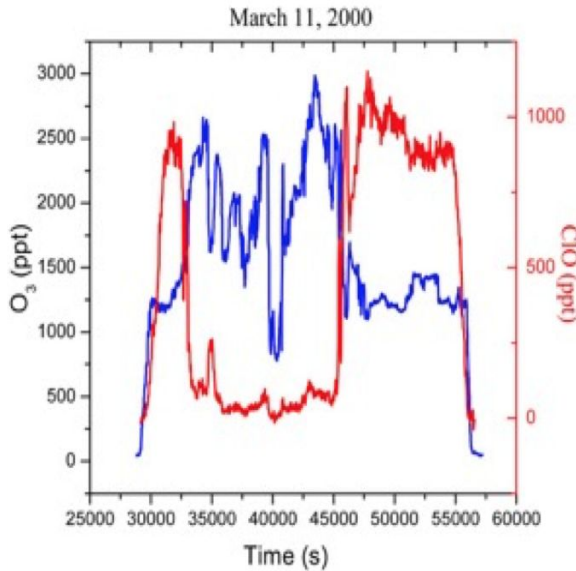


**Catalytic Cycle 2**



### 2.3.2 Arctic measurements

A major distinction was later discovered that showed that activation of chlorine could happen on liquid sulfate-water aerosols. This was crucial because sulfate aerosols are ubiquitous in the stratosphere, meaning that ozone depletion could theoretically happen anywhere around the globe. This is, if all other required conditions are satisfied simultaneously. This distinction was also backed up by further in situ measurements taken from the ER-2 over the Arctic by the Anderson group, that also showed the anticorrelation between the concentration of ClO and ozone:

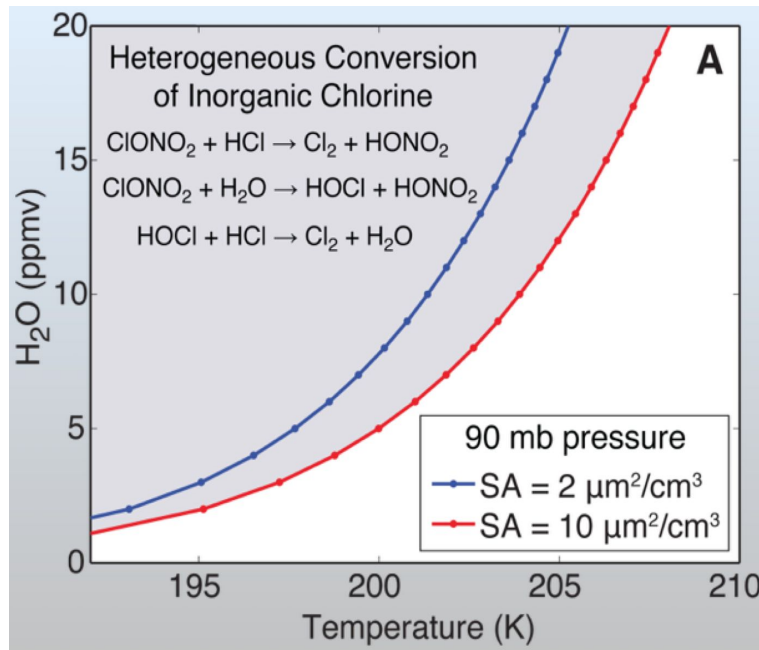


### 2.3.2.1 Adapted mechanism

Following this scientific breakthrough, the same two catalytic cycles were responsible for ozone depletion, but now this could happen anywhere, so long as sulfate aerosols are present. Knowing this, it then begged the question, what are the other conditions for chlorine activation and are they present anywhere else other than the Antarctic?

### 2.3.3 Conditions for chlorine activation

The development of the dependence on sulfate aerosols allowed threshold conditions to be created that showed when chlorine activation would occur. The three conditions it depended on was the concentration of sulfate aerosols, temperature and the concentration of water vapour. The three conditions can be displayed in the graph below, where the grey area is where chlorine activation occurs and the y-axis is water vapour concentration (ppmv), x-axis is temperature (K) and the threshold boundaries are different concentrations of sulfate aerosols.



### 2.3.3.1 Sulfate aerosols

Using the threshold conditions graph shown above, we can see that as the concentration of sulfate aerosols increase, the area in which chlorine is activated increases. This makes sense, because the conversion of inorganic chlorine actually occurs on these aerosols, so it is more likely to occur when there is more sulfate present.

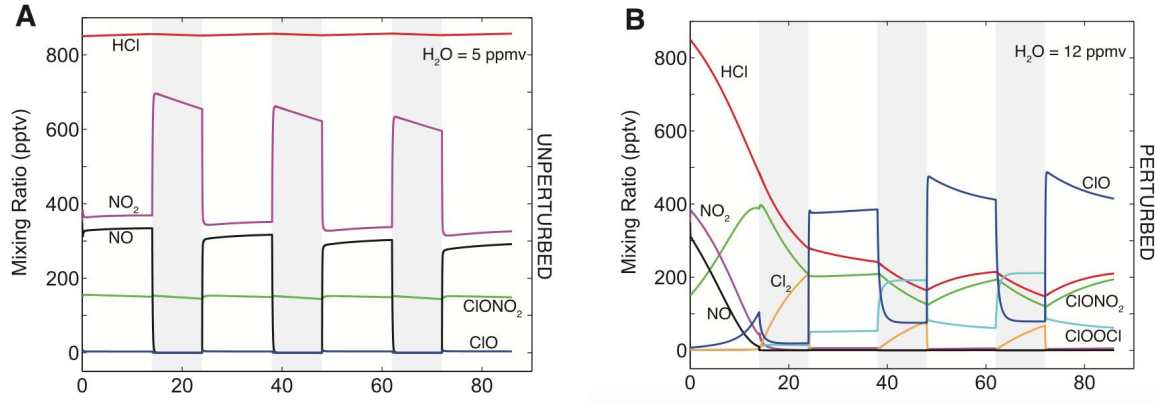
### 2.3.3.2 Temperature

We can also see that this reaction is very sensitive to temperature. As the temperature decreases, we are more likely to cross over the threshold conditions. This can explain why this reaction readily occurs in Antarctica, because as the temperature gets well below 200K, there needs to be very little water present for this reaction to occur. This is also important because in the summertime, stratospheric temperatures actually get colder, so chlorine activation is more likely to occur over the summertime.

### 2.3.3.3 Water vapour concentration

Furthermore, we can see from our threshold conditions graph above that chlorine activation is more likely to occur as the concentration of water vapour increases. The background water vapour concentration in the stratosphere over the United States is 5ppmv and the temperature is ~205-210K, so the threshold conditions aren't crossed, but if water was to be injected to the stratosphere then ozone depletion could occur above the US during the summertime. Seen below is two simulations that were run through a diurnal cycle, with the catalytic chemistry described above occurring, the only difference is the concentration of water vapour. We can see that when the concentration of water vapour is elevated (12ppmv), then our

predominant reservoir species, HCl is depleted and ClO is formed, whereas when the concentration of water vapour is at background levels (5ppmv) then our system is in balance and the chlorine stays in reservoir forms. This highlights the significance of the water vapour concentration and how depended this chlorine activation is on it.



## 2.4 Scientific background

**Conditions over US summer.** The conditions over the US during the summertime are unique, in that they do allow for threshold conditions to be met, and therefore ozone can be destroyed. The concentration of sulfate aerosols remains at the background concentration of  $2 \mu\text{m}^2/\text{cm}^3$  and while temperature gets colder over the summer, increasing the chance of chlorine activation, it is set by position rather than anything spectacular happening over the US. The important parameter that changes a lot over the US is the concentration of water vapour, that is increased by convective storms.

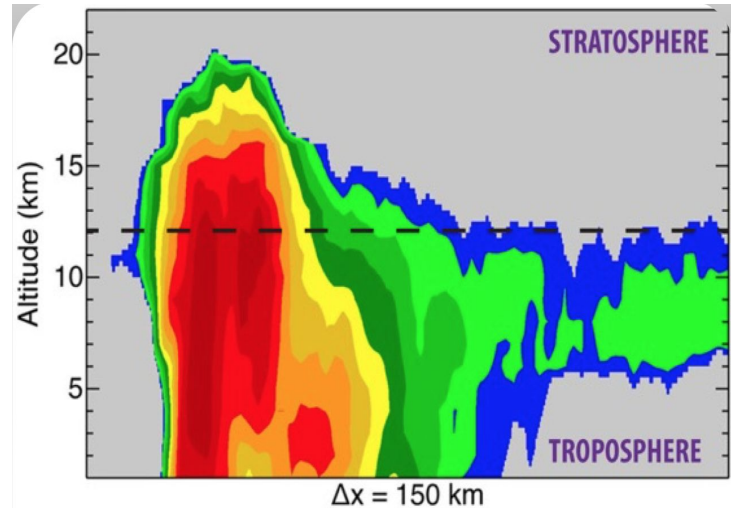
### 2.4.1 Convective storms

The US is unique because it is the only place in the world where convective storms are powerful enough to penetrate the tropopause and increase the concentration of water vapour over the US. This is purely because of geography, warm water from the gulf of mexico is evaporated, creating air with a lot of energy once the latent heat of condensation is released. This happens when this air parcel is lifted over the inland mountains in central USA causing rapid convection and heat release that is not stopped until the cold and relatively dry conditions of the stratosphere are reached. Storms are known to reach 19-20 km altitude which means that they must penetrate the tropopause with a velocity of 80 m/s. This was previously believed to be impossible, before observations were taken in 2004 from the Next Generation Radar (NEXRAD) system that showed 3-D images of these storms.

#### 2.4.1.1 NEXRAD

NEXRAD is a system of 160 radars across the US that are operated by the National Weather Service (NWS), an agency of the National Oceanic and Atmospheric Administration

(NOAA). The system covers the entire US and has provided us with 3-D images of convective storms reaching an altitude of 19km:



The system also has allowed us to see that stratospheric convective injection reaches 19km over the central US 40-50 times per year in June-August. This is critical because it allows the concentration of water vapour over the US during this time to increase.

#### 2.4.2 Anticyclonic monsoon flow

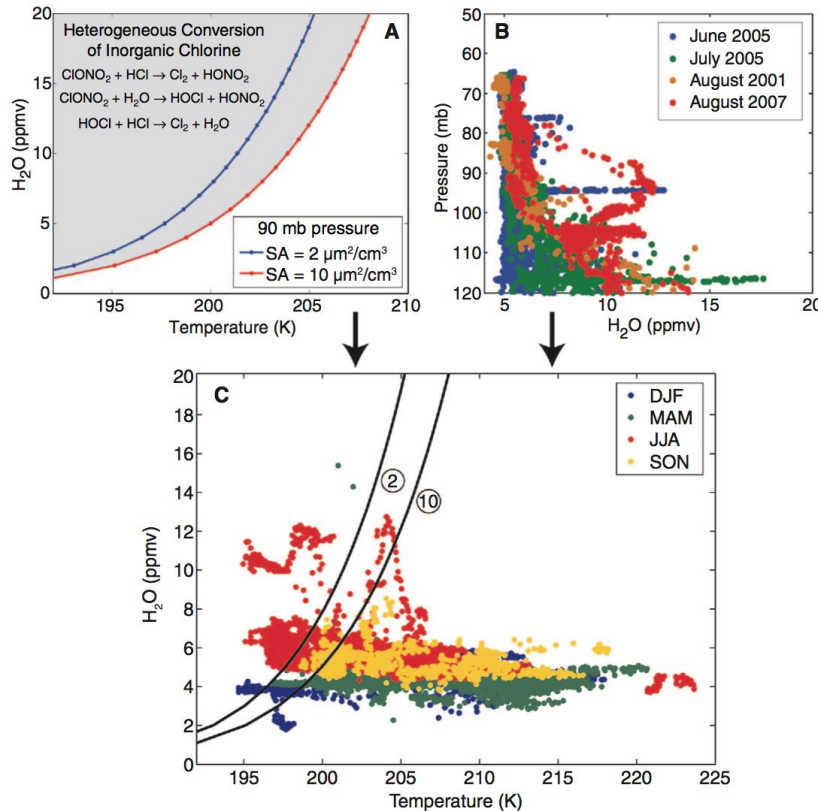
As shown above, the conditions for chlorine activation over the US during the summer can be achieved due to increased water vapour concentrations. But this would dilute relatively quickly if it wasn't for the anticyclonic monsoon flow that prevails over the US during the summertime:



This flow can trap air over the central US for a period of 10-14 days allowing the conditions to be held. This means that if the conditions are such that chlorine activation is occurring, then ozone depletion can occur while this anticyclonic flow is occurring and water vapour concentrations are held elevated.

### 2.4.3 Current observations

While observations of ozone depletion over central US during the summertime have not been taken, we know that the conditions have been met for ozone destruction to occur. We know this by compiling water vapour concentration data based on altitude and plotting this on our threshold conditions graph:



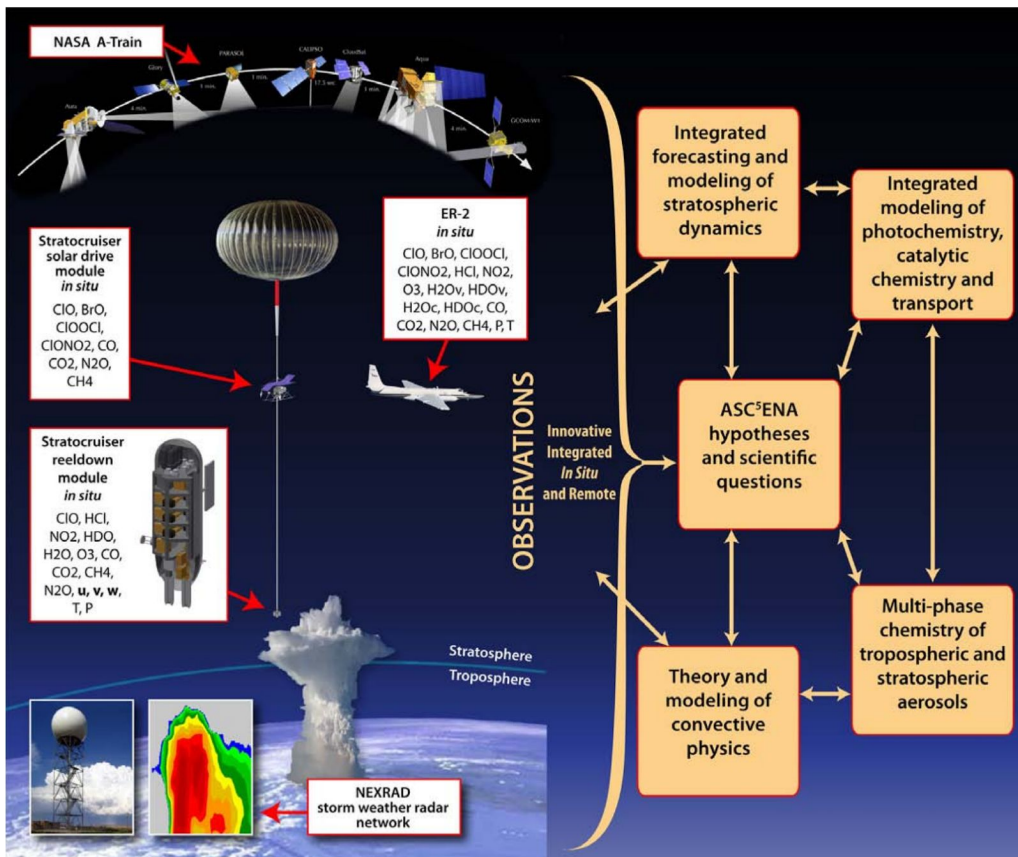
This result shows us that through June, July and August, there are significant amounts of times where water vapour levels are elevated at a temperature which would result in chlorine activation and ozone loss.

### 2.4.4 Verifying the chemistry with observations

So we have observations of the conditions being met and a general understanding of how the chemistry works - what comes next? This project looks at obtaining a vertical concentration of HCl profile in unperturbed conditions, to see where the potential for activation is, and also serves to observe chlorine activation over the US during the summertime. This is important, because it could verify the chemistry behind the problem as well as give us permanent data that this is occurring and is a serious issue.

## 2.5 ASC<sup>5</sup>ENA Proposal

The ASC<sup>5</sup>ENA Proposal is a long-term scientific mission to measure the concentrations of key molecules in the lower stratosphere. The mission plans to send up a host of instrumentation equipment onto a payload that will be moved over convective storms in the United States during the summer to take *in situ* measurements. There are three major components to the ASC<sup>5</sup>ENA Proposal: the long duration pumpkin balloon, the StratoCruiser drive module, and the suspended payload.



### 2.5.1 Long Duration Pumpkin Balloon

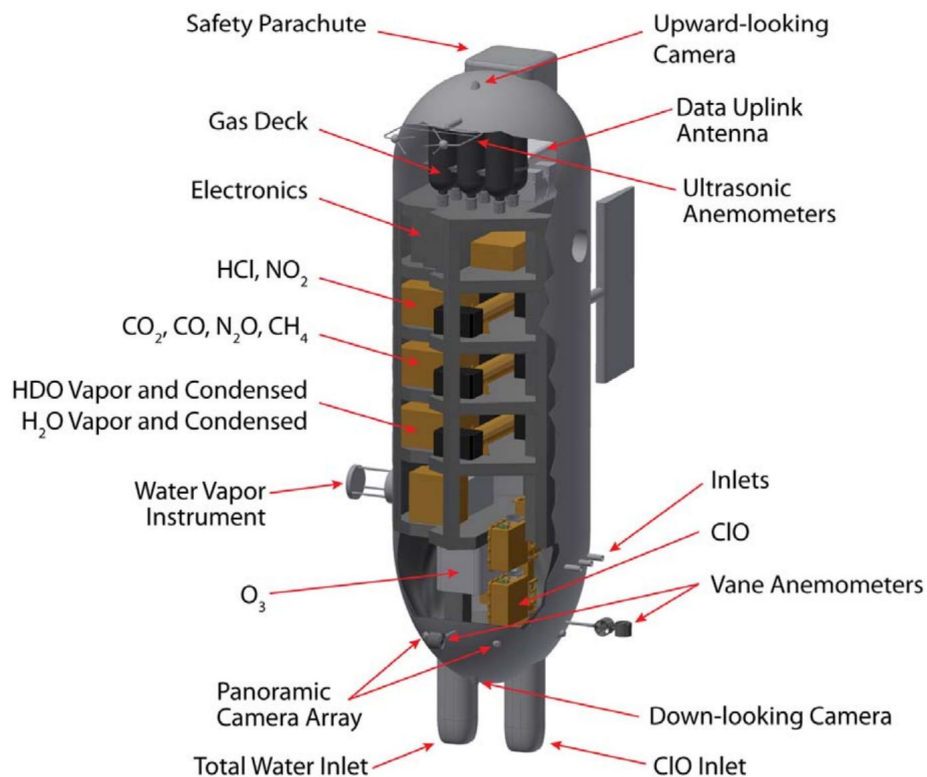
The long duration pumpkin balloon will provide the necessary lift to bring the entire system into the lower stratosphere and keep it suspended there for the duration of the trip. This type of balloon will float at 65000ft and be able to support 1600kg of mass. The conditions in the lower stratosphere can vary greatly during the summer months over the United States. The strong amount of sunlight can heat the balloon and there are cold storms that move through that altitude during the daytime. The volume for the balloon is going to be  $1.067 \times 10^6 \text{ ft}^3$ .

## 2.5.2 Stratocruiser Drive Module

The main purposes of the drive module are to provide navigation and to generate/store energy for the entire system. To propel the balloon, the StratoCruiser has efficient electric propulsion propellers that are optimized for high-altitude conditions. This propulsion system enables the module to achieve distances over 500km per day and speeds around 8 m/2. The drive module will also be able to generate energy from the use of 50m<sup>2</sup> of solar panels that are attached. The maximum storage capacity for the batteries is 25 kW-hr. Minus the energy needed for the motors, the remaining power (continuous) for the payload is 5.3kW/hr during the day and 2.0 kW/hr during the night.

## 2.5.3 Suspended Payload

The suspended payload is connected to the StratoCruiser drive module by a winch system (unique to Harvard). The winch allows for the payload to be raised and lowered 10km at speeds of 5m/s. This will allow for the creation of a detailed vertical composition of the molecules being brought up to the lower stratosphere during convective storms. The molecules that are to be measured *in situ* are: HCl, NO<sub>2</sub>, CO<sub>2</sub>, CO, N<sub>2</sub>O, CH<sub>4</sub>, O<sub>3</sub>, and ClO. These will each require specialized scientific instruments and have to be small enough to fit into the dimensions of the payload. In addition to the scientific instruments, the payload is equipped with upward-looking and downward-looking cameras. Data from the suspended payload will be sent via Iridium Satellite Data-link to a science control station on the ground.

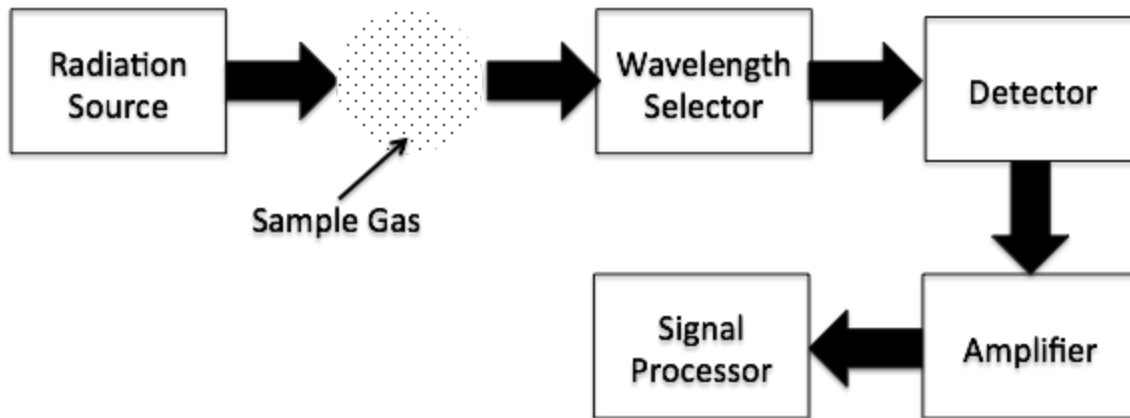


Many of the design considerations that went into the HCl instrument came from the limitations made on the payload. For instance, the maximum weight for all the instruments is 200kg so a lighter design would be needed. Additionally, the volume is very constrained, so having the smallest cavity length while still being able to produce long path lengths is essential.

## 2.6 System Overview

### 2.6.1 Introduction to Molecular Detection Method

Thus, in order to detect HCl at the required sensitivity of approximately 10 pptv, we elected to use an Integrated Cavity Output Spectroscopy (ICOS) system. ICOS, as the name implies, is a specialized method of absorption spectroscopy. The diagram below is a generalized, basic absorption spectroscopy system, displaying the principles of how our system functions.



As can be seen above, a radiation source such as a laser is directed through a sample gas. As the beam of photons passes through the sample gas, some of the photons will be absorbed by the gas, depending on the properties of the photons and the electron states of the sample gas. The intensity of photons that passes through the sample gas at the specified wavelength will be picked up by a detector system. This intensity is then translated by the detector into an electrical signal, amplified, then processed for analysis. As mentioned earlier, although our ICOS system is far more complex than the displayed diagram, it operates under these basic principles.

### 2.6.2 Instrument Sensitivity and Performance

Thus, the ICOS system, like other spectroscopy systems, also obeys Beer's law, displayed below.

$$\ln\left(\frac{I}{I_0}\right) = -n\sigma L$$

*I* = post cavity intensity

*I<sub>0</sub>* = initial intensity

*n* = concentration

$$\sigma = \text{absorption cross section}$$

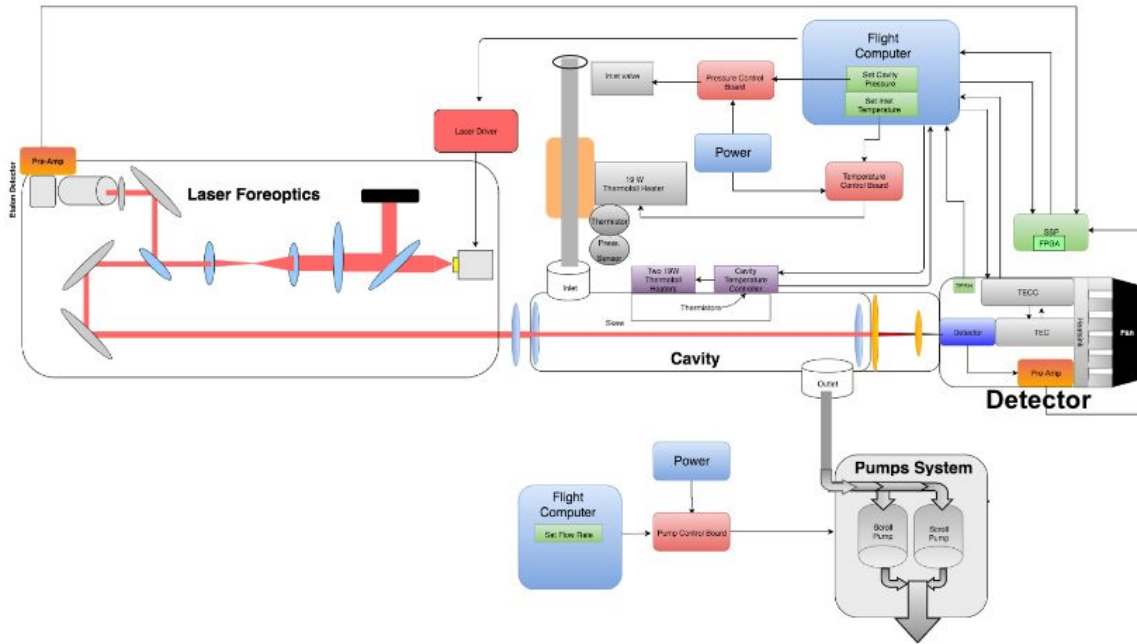
$$L = \text{path length}$$

As can be seen from Beer's Law, if  $I_0$ ,  $n$ , and  $\sigma$  are held constant then as path length,  $L$ , increases,  $I$ , the final measured intensity, must necessarily fall. In other words, as path length increases, more photons will be absorbed by the sample gas, even if the sample gas is held at the same concentration. Given that the absorption properties of the sample gas are known, then, a greater amount of absorption allows for a greater magnitude of sensitivity. For example, the photons of a laser passed through a short, 1 meter cell with trace amounts of HCl may show no absorption when detected on the other side, falsely indicating that there is no HCl within the cell. However, the same photons when passed through a much longer, 5km cell with the same concentration of HCl is much more likely to be partially absorbed, thus indicating presence of HCl and allowing for calculation of its concentration within the sample gas based on the properties of the laser and HCl itself. This is critical, because what makes the ICOS system so unique is that it utilizes a set of highly-reflective mirrors to greatly increase the effective path length of a gas cell, allowing for much more sensitive detection of HCl, on the order of parts per trillion.

### 2.6.3 Accuracy and Precision

We define accuracy as how close our measurement is to the true value, and we define precision as how close repeated measurements are to each other, or to the noise level on repeated measurements. Thus, for our purposes, we considered accuracy to be a measure of bias and precision to be a measure of spread, in part defined by the detection limit, which is the smallest quantity the instrument is able to detect. In order to maintain scientific validity, we wanted to ensure that our accuracy was within 10% of our lower expected range, and our precision was within 5% of our lower expected range. In other words, for our expected range of HCl in the lower troposphere and upper stratosphere of 50 pptv - 1.5 ppbv, wanted to ensure an accuracy of being within 5 pptv of the true and a precision of ~2 pptv for repeated measurements of the same value. This factored greatly into our choice to use the ICOS system to detect HCl, as simulations utilizing Beer's Law, our research, and previous research and tests completed by the Harvard Anderson Group all indicated that this level of accuracy and precision would be achievable by the ICOS system.

## 2.6.4 Integrated Cavity Output Spectroscopy (ICOS) System Diagram



Displayed above is the final system diagram for our ICOS system. As can be seen, the system is composed of five main components -- the laser, the cavity, the pump system, the detector, and the flight computer. Each system will be briefly described below in order to give the reader a better understanding of how the ICOS system works together as a whole. For more detailed explanations of each subsystem, please refer to the appropriate section within this document.

### 2.6.4.1 Laser and Foreoptics

The radiation source of our ICOS system comes from a laser driver, which generates the photons that form our laser beam. This laser beam is then narrowed and polarized by a set of foreoptics, and then passes through a beam splitter, splitting the beam of photons in two. Ideally, we wanted approximately 8% of the photons to be reflected into an etalon detector, and the rest to pass through into the cavity itself. We selected the wavelength of our laser to be specific to the absorption properties of HCl (and thus not absorbed by other atmospheric gases). This selection process is further explained within the laser sub-section.

### 2.6.4.2 Cavity

After the laser passes through the foreoptics subsystem, it enters the cavity. The cavity is the cell that contains our sample gas, and so constantly draws air from the environment via our pump system. In addition, in order to keep readings consistent, it is maintained at a specific

pressure and temperature. Finally and most importantly, in order to greatly increase the effective path length, the cell is equipped with a set of highly reflective mirrors and a re-injection mirror. Thus, as the photons from our laser enter the cell, they are reflected repeatedly thousands of times, increasing the effective path length of our system from the order of magnitude of one meter to approximately five kilometers.

#### **2.6.4.3 Pump System**

Our pump system is a set of four scroll pumps placed at the outlet of our cell system. As mentioned previously, the main job of our pump system is to maintain the cavity at a specific pressure while continuously drawing air from the environment in order to be sampled. The pump system utilizes a sub-system of controlled valves in order to maintain pressure at a given setpoint, explained in greater detail within the pump section. The scroll pumps in our system represent an innovation discovered this year, as they are much lighter and more efficient than previous pumps that have been used in similar ICOS systems.

#### **2.6.4.3 Detector System**

The detector system is composed of two detectors -- the etalon detector and the cooled detector. As mentioned earlier, the etalon detector is placed prior to the cavity, whereas the cooled detector is placed after the cavity. The cooled detector is our main system detector, as it measures the post-cavity photon intensity of the laser, and thus allows us to calculate the concentration of HCl in the gas sample. Thus, in order for this highly-sensitive detector to operate properly, it must be kept within its own pressurized and heated housing, known as the detector pressure vessel.

After this cooled detector is struck by the photons that have passed through the cavity, it translates this intensity into an electrical signal, which is amplified by a pre-amp and passed to a signal processing board. After the signal is processed, it is then passed to the flight computer for data storage.

#### **2.6.4.4 Flight Computer**

The flight computer manages all of the command and control and data acquisition for our ICOS system. While much of the hardware and software subsystems for the flight computer had already been developed through the hard work of the Harvard Anderson Group in the last decade, we were responsible for adapting the existing systems to our specific ICOS instrument, such as by adjusting our hardware diagram, re-wiring connectors, and rewriting computer data displays.

SCIENTIFIC REQUIREMENTS & ENGINEERING DESIGN SPECIFICATIONS

### 3. ENGINEERING DESIGN SPECIFICATIONS

#### 3.1 System-wide requirements

##### 3.1.1 Payload integration

The HCl detection instrument will be integrated into a payload capsule to be suspended from a gondola below the StratoCruiser balloon.

##### 3.1.2 Power, Mass, and Volume Budgets

Since the HCl instrument is only one of a number tools that will ultimately be included in the suspended payload, the instrument must minimize use of energy, mass and volume. Early in the design, we set out design goals for these limited resources. Below is a table summarizing the goals for these budgets and a system-by-system breakdown estimating the energy, mass, and volume usage:

System	Power Est (W)	Mass Est (kg)	Volume Est (L)
Pump	215	3.10	2.26
Cavity	39	1.20	2.50
Laser (Driver)	1	0.23	0.02
Laser (Fore-optics)	0	2.27	8.85
Detector	1	2.60	4.56
Additional Housings	0	10.00	2.00
Total (41 not incl pump)	256	19.40	20.19
Design Goals (60 not incl. pump)	<500	<25 kg	<25 L

As the table shows, in its current state the instrument is meeting or beating the design goals for all categories.

##### 3.1.3 Flight software and data storage

Flight computer is an important part of our ICOS instrument, because it is responsible for the data acquisition, data storage, data analysis, and even issuing out commands to maintain the system's functionality. Here is an outline how the flight computer works (using the information from the Anderson Group Data Acquisition Software):

1. Data is being received by the collector. It can come directly from the hardware, or through a driver. The collector generates data and assembles it in a way so that it could be sent to the telemetry buffer. The collector needs to know what the data is about (its precision, accuracy, units, resolution, etc.), so it interacts with many different interfaces.
2. The telemetry buffer is a data distributor. It sends data out to many different data clients, e.g. the extraction programs, displays, logger programs, and the data analyser.
3. The data analyser, or TMCalgo, is the brain of the instrument. This is the program that is responsible of making decisions based on the data stream.
4. The commands and decisions made by the TMCalgo go to the Command Server. This server interprets commands received from the algorithm (or from the keyboard for that matter), and provides a variety of interfaces in order to deliver these commands to the destination.
5. From the destination, new data can be received, which will then be sent to the Collector, thus completing the loop.

A visual image of the system can be seen in the picture below. Thanks to Norton, most of the code was already generated, we only had to make changes based on the new signals that we were expecting to monitor.

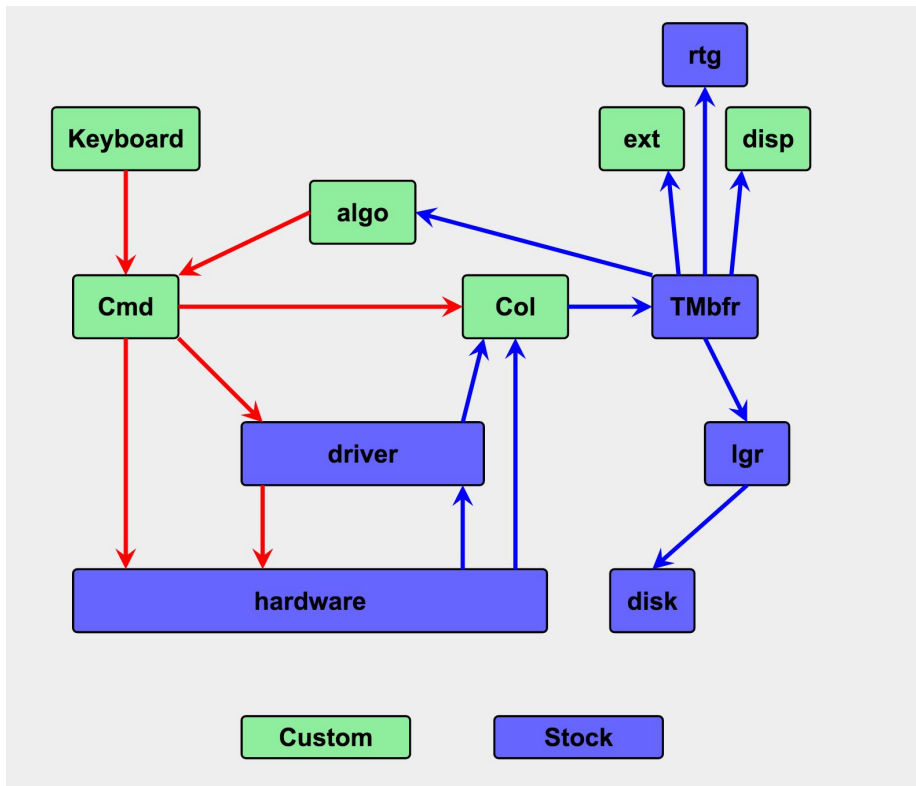
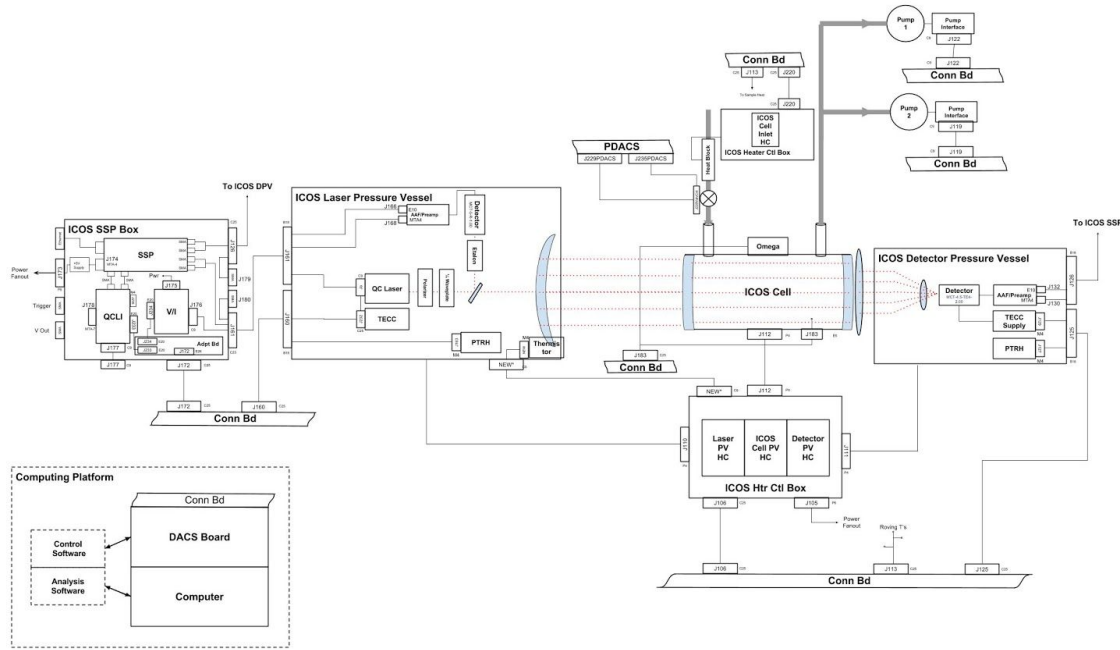


Diagram of the Flight Software setup, from [http://www.arp.harvard.edu/eng/das/guides/das\\_arch.html](http://www.arp.harvard.edu/eng/das/guides/das_arch.html)

### 3.1.3.1 System inputs and outputs

In order to have a well working ICOS instrument, we needed a neat flight computer. The purpose of the flight computer is to communicate with different parts and sensors of the instrument, so that everything could work well together and changes could be made to the system based on some of the readings. In order to do that, we needed to define all the signals and channels that would potentially need to communicate with either each other or with the software. We ended up defining around 50 channels that needed to be monitored, and we also defined the connections between different parts. The results can be seen in the following system wide interconnection diagram:



System Wide Interconnection Diagram

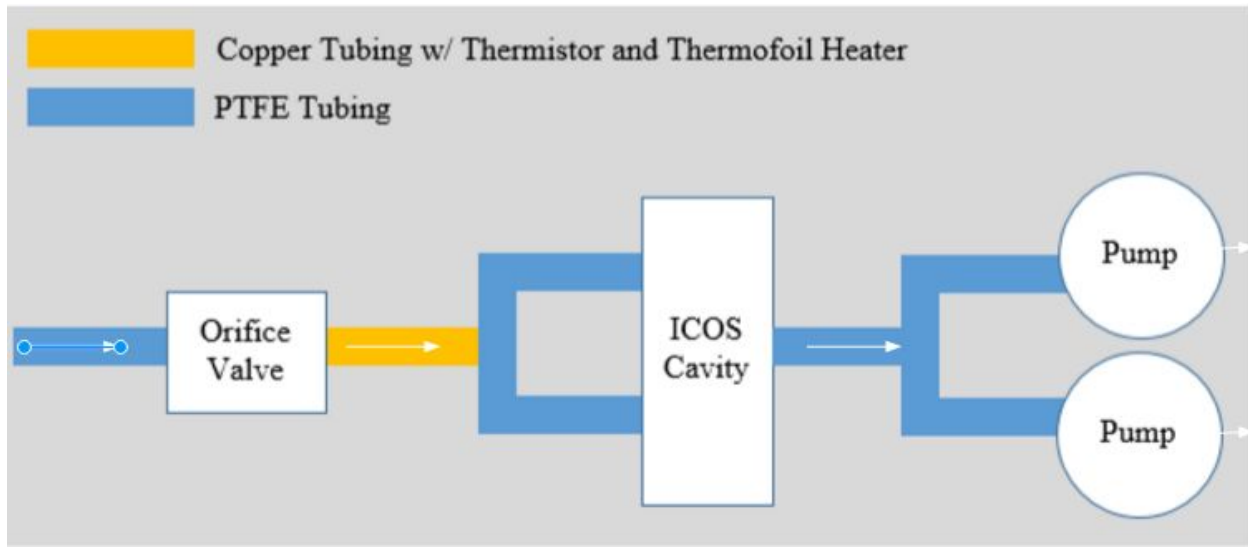
We were allowed to use the system diagram from last year's project, since we had very similar systems (both using HCl ICOS instrument). However, couple of changes were made to the diagram, including the additional pump interface, and the valve and servomotor interface. In addition, we deleted the pressure controller box since no pressure controller was needed anymore.

Coming up with a system diagram was half the battle. The second half was to make sure that all the connections make sense, and that they are all defined. For that, we used last year's documentation, and edited it so that it would fit our design requirements. Moreover, we had to make sure that the signals were routed from the sensors to the corresponding connector boards or drivers. We were lucky because some of the connections were already made by the last year's HCl team, but for some of the interfaces (pump, servomotor), we had to do some additional

wiring. Eventually, everything seemed to be working on the paper, but not much was tested out due to the constraints in time. Ideally, everything would work through the flight computer, so for example based on the pressure transducer reading, the valve would be adjusted. Such things were not tested out, and this is something that could be done in the future.

### 3.2 Flow Control System Design

The flow control system as a whole is the collection of components controlling the conditions of the air going into the cavity for sampling, and then bringing this air out again. The basic setup of this system involves air first being pulled through an orifice valve that controls the pressure going into the cavity. This valve is connected to a servo motor with a motion controller and pressure control board that can autonomously control the valve position to maintain constant pressure at all altitudes. Then the air goes through a segment of copper tubing connected with a thermistor and a thermofoil heater. The thermistor and heater are connected to a thermal control board to maintain constant temperature. Then this air goes through two tubes into the cavity where the laser and detectors do the sampling for HCl. Finally, the air is pulled out back into the atmosphere through two scroll pumps.



#### 3.2.1 Pump

The pumps are one of the major components of the flow control system. Ultimately, two SVF-E0-50 scroll pumps from ScrollLabs were chosen for use in this instrument. This decision was based on multiple design requirements that were met by this pump, and certain characteristics of the pump that made it very attractive for this project, including size and weight.

The design requirements that were set for the pump will be listed below, as well as the reasoning behind each. Then, the decision to specifically purchase the SVF-E0-50 will be

explained. Finally, testing on the pump to ensure that it can perform up to expectations at high altitudes was performed and documented.

### 3.2.1.1 Pump Design Requirements

The pumps need to meet certain specifications in order to be suitable for the HCl detection instrument. The entire system needs to take measurements at a frequency of at least 1Hz in order to have scientific merit, needs to operate at altitudes ranging from 10 to 20 km, and has a set weight and power limit to distribute among multiple systems. These considerations guide the design requirements that were considered for the HCl instrument. Ultimately, the design requirements that were set by the team were: flow rate, vacuum pressure, maximum pressure differential, power usage, weight, motor type, and flow type. The actual requirements that were decided upon are provided below and will be explained in the next sections:

Flow Rate	90 L/min
Vacuum Pressure	40 torr or 53 mbar
Maximum Pressure Differential	165 torr or 220 mbar
Maximum Power Usage	500 W
Maximum Weight	10 kg
Motor Type	Brushless DC
Flow Type	Continuous

#### 3.2.1.1.1 Flow Rate

It is necessary for the entire system to take measurements at a frequency of at least 1Hz in order to take enough measurements to be accepted as valid data by the scientific community. The cavity itself is 1L, and each measurement ideally needs a completely new volume of air to make sure it is a different measurement. Therefore, 1L of air must be replaced at least every second, if not more quickly. In order to account for any losses of performance by the pump at high altitude, it was necessary to increase our minimum requirement by 50%. Therefore, the requirement for flow rate was set at 1.5 L/s, or 90 L/min.

### **3.2.1.1.2 Vacuum Pressure**

The highest altitude that the balloon and the system will operate at is 20 km. The pressure at that altitude is 40 torr, or 53 mbar. For any pump that works as a vacuum, it is necessary for the pressure inside of the pump be lower than the outside pressure, or at worst, around equal to the ambient pressure. Therefore the minimum vacuum pressure should be 40 torr (53 mbar).

### **3.2.1.1.3 Maximum Pressure Differential**

The entire expected range of operation for the instrument module is between 10km and 20 km. The corresponding range of pressures is 205 torr (273 mbar) to 40 torr (53 mbar). Therefore, the maximum difference in ambient pressure that the instrument will operate under during its mission is 165 torr (220 mbar).

### **3.2.1.1.4 Power Usage**

In total, the instrument uses up 5 kWh over around 10 hours of the day, which roughly equates to 500W of power usage. As the pump system takes up almost all of this power, and this pump would hopefully be able to service all of the instruments eventually, the entirety of the 500W was budgeted to the pump. However, the less power usage there is the better.

### **3.2.1.1.5 Weight Limit**

The payload of the system has a total mass of 200 kg. There are multiple instruments, and the hull itself, so it is estimated that each instrument should at most weight 20kg. The pumps have typically been the heaviest component of the instrument, so a budget of half of the total weight was given to them. Therefore, the pump is allowed to be up to 10kg at its maximum.

### **3.2.1.1.6 Motor Type**

At high altitudes, brushed actuators are much more likely to arc because there is less air to effectively insulate the electrical components. This makes it easier for electrons to hop over to different electrical components that are situated nearby, but aren't connected, causing a short. This could potentially destroy the circuitry of the instrument and render it useless. Therefore, it is important that the motor is brushless.

### **3.2.1.1.7 Flow Type**

The goal of the air flow system is to fill the cavity with a completely new batch of air at each sampling point. Unless the pumps and the detector are perfectly synced, non-continuous flows of air would mean that some old air might be remaining in the cavity at the time the detector takes measurements. A continuous air flow from the pumps takes away the need to sync the pump with the detector while ensuring a new sample of air at every sampling point. This requirement was designated as optional, because it was very good to have, but it wasn't impossible to work without this feature.

### 3.2.1.2 Pump Selection

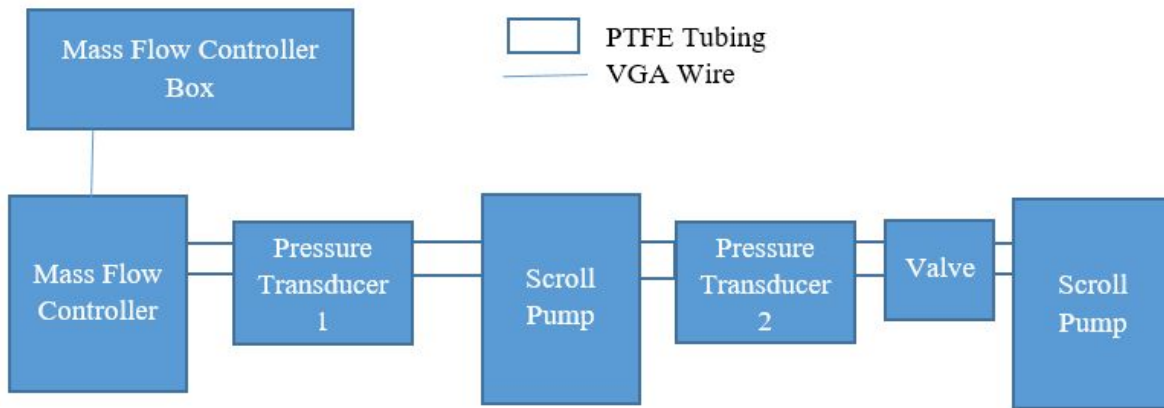
During the exploration of pump options from multiple manufacturers, the team decided that it would be easier and more efficient to buy multiple pumps of smaller sizes than a single, larger pump. This is because the single pumps that met the requirements were very large and heavy, and anything smaller wasn't possible to find. These pumps will be run in parallel to achieve the desired flow rate. The choice came down to two types of pumps, both of which satisfied the design requirements. These two pumps were the SVF-E0-50 from ScrollLabs or the T2-01 from Parker. The specifications are included below, in addition to the single pump used in a previous instrument for comparison.

Pump	SVF-E0-50 (ScrollLabs)	T2-01 (Parker)	KNF N838 (Old Pump)
<b>Pump Type</b>	Scroll	Diaphragm	Scroll
<b># pumps needed</b>	2	2	1
<b>Weight (kg)</b>	1.0 (2.0 total)	1.38 (2.76 total)	3
<b>Volume (L)</b>	0.968 (1.936 total)	1.78 (3.56 total)	1.5
<b>Power Usage (W)</b>	95±3 (190±6 total)	69 (138 total)	101
<b>Vacuum Pressure (mbar)</b>	≤1.0 (ultimate)	406 (differential)	90
<b>Flow Rate (Standard L/min)</b>	45	66	60
<b>Price/Unit (\$)</b>	2590.00 (5180 total)	809.00 (1618.00 total)	--

Of the two options, the T2-01 is preferable in the areas of power, flow rate, and price; however, the SVF-E0-50 is better in terms of weight and pure size. We ultimately decided benefits of smaller and lighter pumps outweighed the power considerations, because in terms of power, both pumps spec at a much lower power than the original design requirement. To get the instrument flight ready in the long run, it needs to be as small and compact as possible, so the savings in space and weight might be vital in the long run. In terms of flow rate, the 90 L/min already meets the requirement, which is higher than needed. Extra flow would not necessarily help if the detector only takes readings at around 1Hz, so that was viewed as a good feature, but ultimately it was extraneous. The SVF-E0-50 also has continuous flow, which is a beneficial part of the requirements. Therefore, the SVF-E0-50 is the best choice.

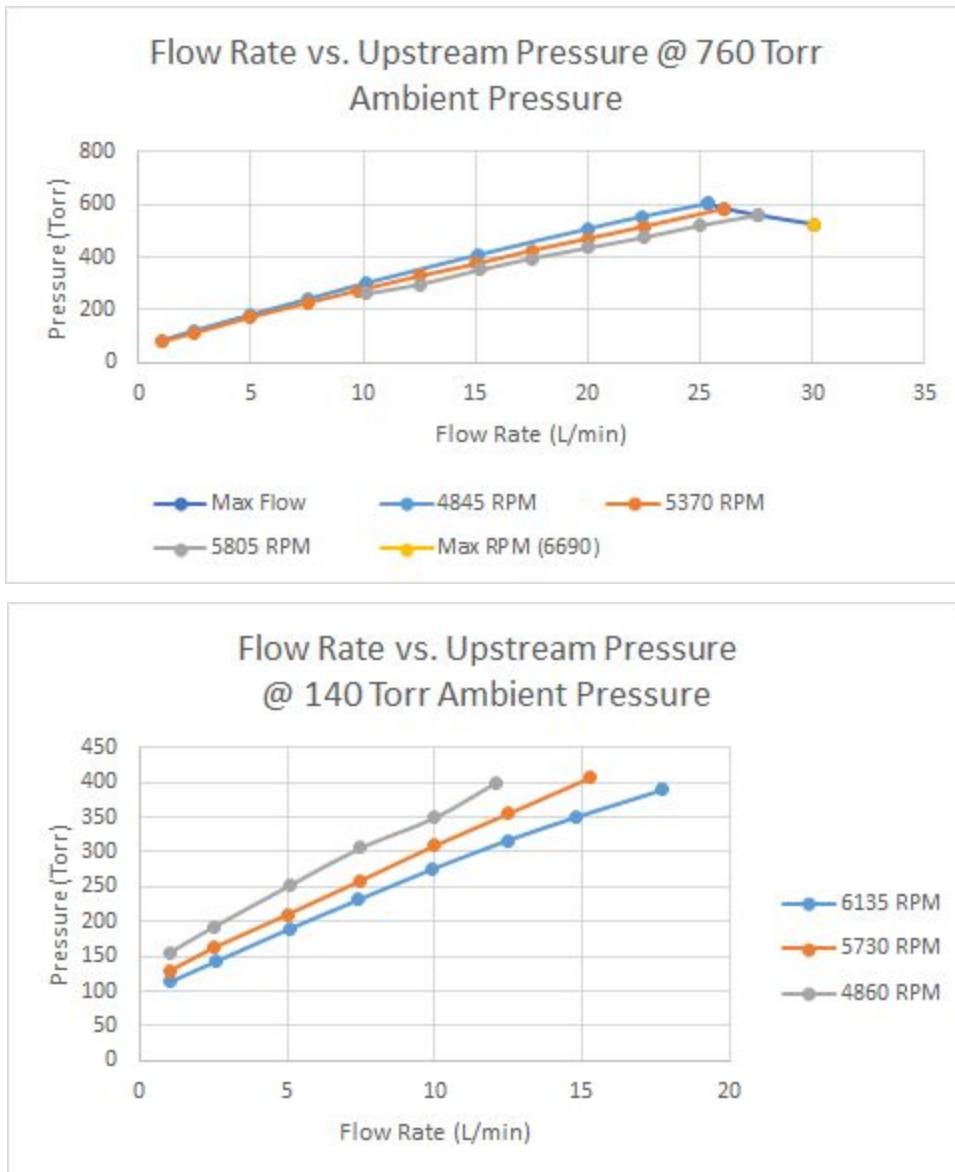
### 3.2.1.3 Pump Testing

Once the pumps were received, it was necessary to test the pump to see if it performed up to specifications. The goal is first to test it at 1 atm, to make sure everything runs up to spec, and then to test it when the pressure at the outlet is much lower, in an attempt to simulate high altitude conditions. The basic setup of the experiment is as follows:



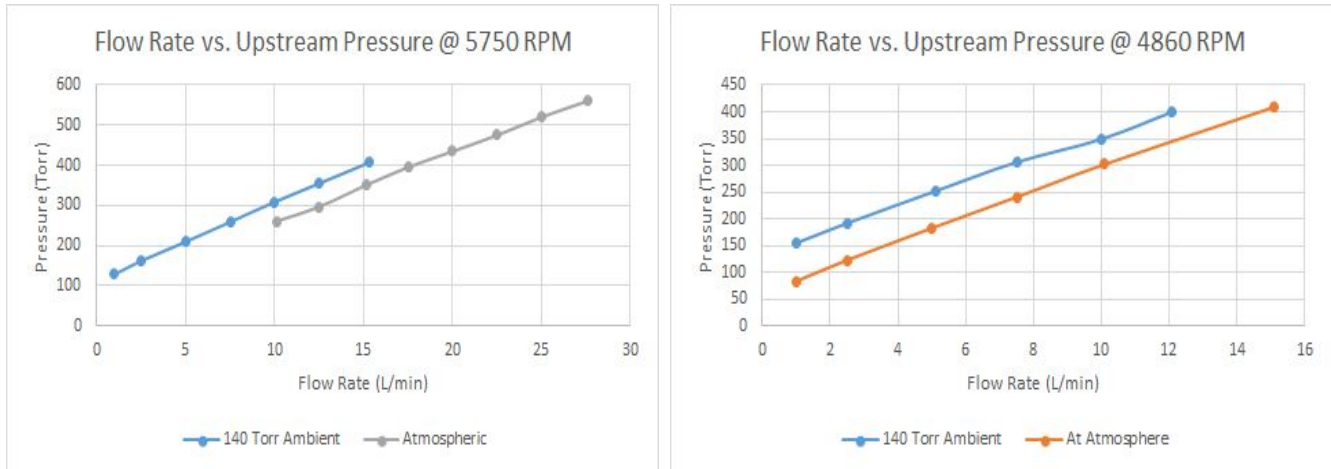
The mass flow controller will act as a valve to limit the flow rate. The pressure transducers will measure pressure, at both the upstream (transducer 1) and downstream (transducer 2) positions of the scroll pump. The valve will be used to maintain a constant pressure (140 torr) at the downstream position of the scroll pump when modelling high altitude conditions, and the second scroll pump will be used to create the low pressure conditions at the outlet of the first pump. The first pump will be the only pump being characterized in this experiment.

The first part of the experiment involves keeping the second scroll pump off and the valve all the way open. The SVF-E0-50 has multiple RPM settings, so for each RPM, the mass flow controller started at all the way open, and was gradually stepped down. For each step down, the upstream pressure was measured (downstream pressure is 760 torr). The second part of the experiment involved turning on the second scroll pump, and using the valve to maintain a 140 torr pressure at the downstream position. For this second part of the experiment, the characterization of the pump started at 400 torr upstream pressure, and the flow rate was stepped down from there. The characterization started at 400 torr because of limitations of the second pump made it impossible to achieve 140 torr downstream pressure at higher upstream pressures. The end results were characterizations of the pump mapping flow rate vs. upstream pressure for different RPMs of the scroll pump at both ambient pressure conditions.



Looking at the first graph of the characterization at 760 torr ambient pressure, the highest RPM gives a flow rate of around 30 L/min at 500 torr. The pump is rated at 45 standard L/min, where a standard L/min is defined as a flow rate regularized to standard pressure and temperature. This means that an actual flow rate at 76 torr would result in a standard flow rate of 10 times that amount, because standard pressure is 760 torr. In this case, to convert 500 torr to 760 torr, there is a factor of  $\sim 1.5$ . Therefore, at max RPM, the pump does in fact achieve a standard flow rate of  $\sim 45$  standard L/min, since 30 times 1.5 is 45.

Next, graphs were created to compare the performance of the pump at the two different ambient pressures at various RPMs.



In these graphs, atmospheric is used to describe conditions at standard pressure. From these graphs, it is clear that there are not major losses in performance at higher altitudes. At most, the pump loses about 2 L/min, and still follows the same characterization curves. Based on these results, it can be extrapolated that if 140 torr downstream pressure can be maintained, the characterization curve should still mimic the characterization curve at 760 torr ambient pressure. With only minor losses, and based on the fact that our pump specs have already accounted for performance losses by increasing the minimum required flow rate by 50%, the team is confident that these SVF-E0-50 scroll pumps will perform up to par at the higher altitudes that it will be operating under.

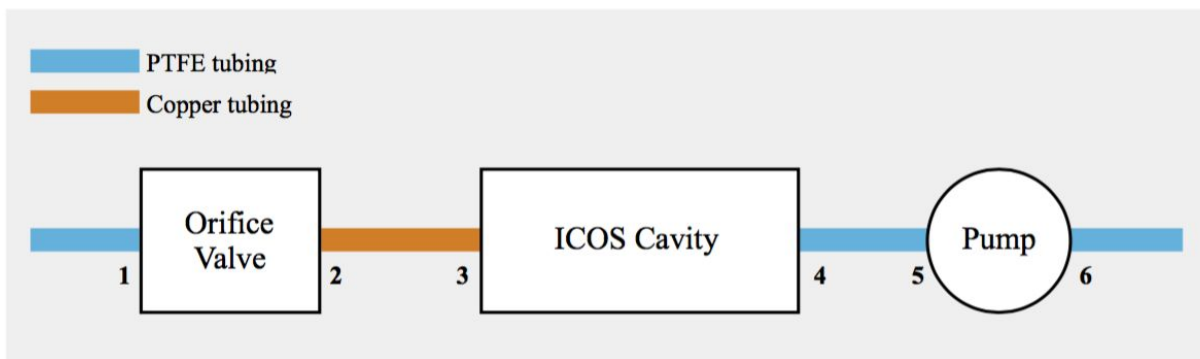
### 3.2.2 Tubing

All connections made between components within the flow control system will use extreme-temperature PTFE or copper tubing, both  $\frac{1}{2}$ " outer diameter. The PTFE tubing has an inner diameter of  $\frac{7}{16}$ " and the copper tubing has an inner diameter of  $\frac{3}{8}$ ".

The PTFE tubing is rated for  $-450^{\circ}$  to  $500^{\circ}$  F and is Durometer 60D rated. The tubing is inert to reactions with HCl and has a smooth interior for unrestricted airflow.

#### 3.2.2.1 Port connections

Compression tube fittings will be used for port-to-port and port-to-tubing connections.



### NPT Connections

- 1 Chemical Resistant PFA Compression Fitting, 1/2" Tube OD to 1/2" NPT Male
- 2 Brass Yor-Lok Straight Compression Fitting, 1/2" Tube OD to 1/2" NPT Male
- 3 Brass Yor-Lok Straight Compression Fitting, 1/2" Tube OD to 1/2" NPT Male
- 4 Chemical Resistant PFA Compression Fitting, 1/2" Tube OD to 1/2" NPT Male
- 5 Chemical Resistant PFA Compression Fitting, 1/2" Tube OD to 1/2" NPT Male
- 6 Chemical Resistant PFA Compression Fitting, 1/2" Tube OD to 1/2" NPT Male

### 3.2.3 Orifice Control

Maintaining constant pressure and temperature within the ICOS cavity are critical to collecting consistent measurements, especially as the instrument climbs thousands of feet into the stratosphere on board the StratoCruiser. For pressure control, the orifice valve is essential - it is the port exposed to the atmosphere and regulates the cavity pressure by restricting airflow. The orifice valve should be able to restrict the airflow in order to isolate the cavity from the surrounding atmosphere if necessary. Likewise, the orifice should also be able to adjust to a fully open position that does not restrict airflow. This position would be enabled when the instrument reaches a threshold altitude in which the cavity pressure is equal to the pressure of the surrounding atmosphere. Lastly, the valve should be built to withstand the forces of normal operation. This includes a valve torque that is able to withstand deviation of position while in flight. The valve should also be constructed to maintain normal operation in the low temperature, low pressure conditions described earlier in this report.

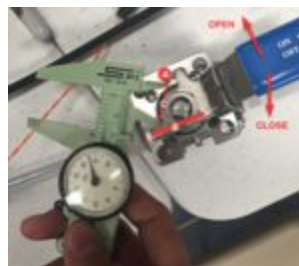
#### 3.2.3.1 Ball valve

We selected a 90-degree v-ball valve for our orifice. The ball valve was ordered from CR-TEC engineering and modified for flight qualification testing. Both ends of the ball valve have  $\frac{1}{2}$ " NPT female threads for easy connections with our copper and PTFE tubing. Since the valve position is controlled by the flight computer in flight configuration, it was important to test and characterize the flow response of the valve. Data from such a test would inform the software controlling the orifice valve position in order to adjust the pressure within the cavity.

The response of the orifice in flight conditions was assessed with an experimental setup utilizing a flow regulating controller, pressure transducers, and a ball valve for regulating inlet pressure. The upstream pressure transducer was a MKS 500 torr model while the downstream transducer was an Edwards Datametrics 1000 torr model. In the test setup, the upstream pressure transducer represents the pressure of the surrounding atmosphere while the downstream pressure simulates the cavity pressure. Both pressure transducers were powered by a +/- 15V and ground power supply. A scroll pump (Varian, Inc.) was used to draw ambient air through the experimental system while the flow controller maintained a constant volumetric flow rate of 9.0 SLM. One pressure transducer was placed downstream while the other was placed upstream of the orifice valve. The inlet pressure regulating valve was used to adjust the upstream pressure, essentially modeling changes in atmospheric pressure experienced in flight conditions.

The experiment was performed based on the position of the orifice valve. The opening size was measured using a caliper as the linear distance from the fully closed position, as shown in the image below. Starting from fully open, the orifice opening was adjusted incrementally and the range of pressure differentials that could be achieved for each increment was measured by regulating the inlet pressure valve. Thus, at each increment of the orifice valve, the range of pressure differentials between the upstream and downstream pressure transducers could be determined. A total of 4 to 6 adjustments of the inlet pressure valve were made for each increment of the orifice valve. The general methodology for the experiment is summarized below:

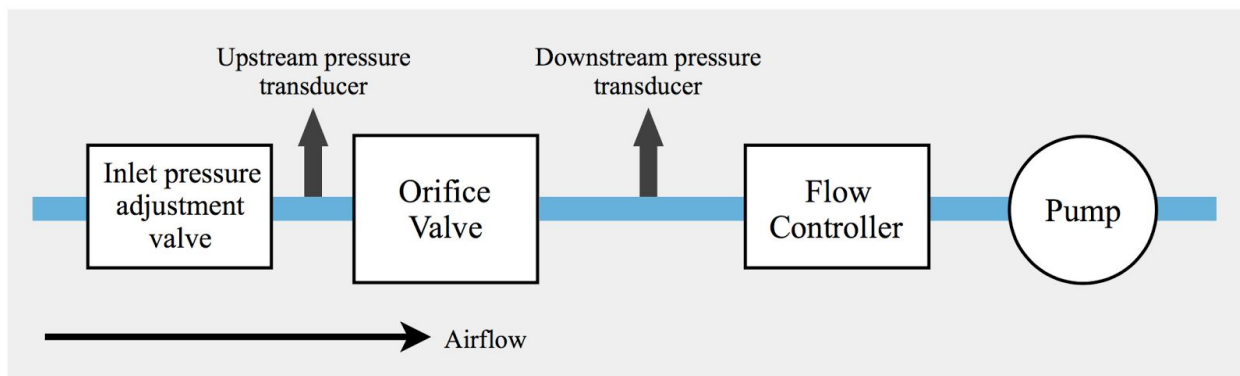
1. Starting with orifice valve fully open, adjust and record orifice valve opening size
2. Adjust inlet pressure regulating valve to achieve desired inlet pressure (indicated by upstream pressure transducer)
3. Record upstream and downstream pressure
4. Repeat steps 2-3 for several inlet pressures
5. Repeat steps 1-4 for several increments of the orifice valve



*Measurement of orifice opening size. The opening size was a linear measurement (C) between points A and B. A distance of 0 between A and B represents a fully closed valve.*

For this test procedure, the experiment was carried out until the inlet pressure regulating valve could no longer set the inlet pressure. Measurements started at a fully open orifice valve and a fully open inlet pressure regulating valve. Pressure differentials were recorded for every ~100 torr drop in the inlet pressure per increment in orifice size opening, allowing for sufficient resolution. Smaller increments were used in changing the orifice opening size when valve was close to fully closed, as greater resolution was required to capture the effect on pressure differential.

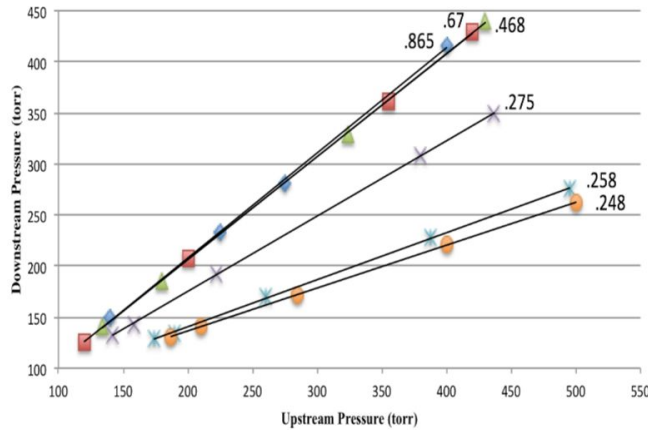
Along with the flow rate through the system, the pressure differential data collected with this methodology can be used to characterize the conductance of the orifice valve within a range of pressures. See the figure below for the full experimental system setup.



Data was collected from the upstream pressure transducer and downstream pressure transducer for each incremental change in orifice valve opening size. The data for the MKS pressure transducer was output to a laboratory computer and converted to be displayed in torrs. The downstream Edwards Datametrics pressure transducer reading was output to a voltmeter ranging from 0-10V. The voltage output was multiplied by 100 to obtain the pressure reading in torrs.

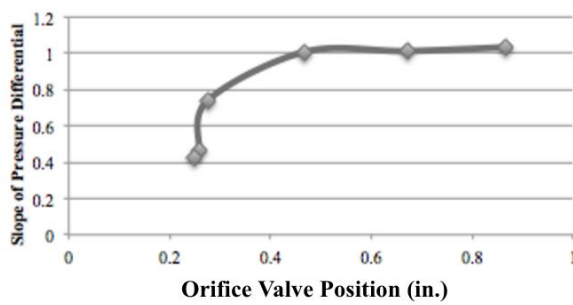
Downstream pressure was plotted as a function of upstream pressure for each orifice valve opening size, as shown below. While the relationship is linear for each orifice size, the slope of the relationship changes as the orifice size is incremented. This is important to note for flight conditions, as the pressure in flight will drop considerably as the StratoCruiser reaches mission altitudes in the lower stratosphere.

**Upstream vs. Downstream Pressure  
(Per Orifice Valve Position)**



The slope of the upstream vs. downstream pressure relation is also shown below for each orifice size. The relationship is 1:1 for orifice opening sizes as small as 0.43in, which is 50% of the fully opening state. After this critical point, the slope decreases rapidly.

**Slope of Pressure Differential vs.  
Orifice Valve Position**



The nonlinearity of the ball valve flow response is important in that it guides the software design controlling the orifice valve position in flight. In particular, the pressure differential data vs. orifice valve position can be used as an input to the algorithm controlling the valve position in order to dynamically change adjustment distance based on the current and desired pressure differential.

### 3.2.3.2 Servo Motor

To drive our orifice valve automatically, we created a servo motor configuration with 1:246 gearhead, delivering a maximum torque of 3.5 lb-ft, more than enough to drive our 0.7 lb-ft valve. The servo motor and motion controller were supplied by MicroMo and are manufactured by Faulhaber. The servo motor was selected for its small size and weight, and ability to operate nominally in flight temperature and pressure conditions.

We also designed and CNC manufactured an adapter sleeve and mount to connect the motor gearhead to the valve. The adapter sleeve, shown below in grey within the gold mount, was manufactured out of stainless steel while the mount, shown in gold, was made of aluminum. The entire assembly fit together securely and had minimal mechanical slippage while in use.



### 3.2.3.3 Feedback and Control

The servo motor is driven by a motion controller board supplied by Faulhaber. The motion controller board, powered by 12-24V, communicated either via RS232 or CAN with the flight computer. We selected to use RS232 serial communication and were successful in driving the motor by sending commands from the flight computer. Command options include setting drive speed, drive to position, drive limits, and more.

The motion controller is ready to be connected to the flight computer in a flight simulation setup. Software will be written to control the orifice size in response to a pressure transducer placed downstream of the orifice valve.

### 3.2.4 Temperature Control

#### 3.2.4.1 Heating element

In order to use Beer's law to calculate the concentration of HCl in the sample within the cavity via a change in light intensity, it is vital that there is no significant temperature gradient within the cavity, either axially or radially. Likewise, it is important that the temperature of the air sample is the same throughout the time we are taking measurements so that calculations are consistent and made under the same conditions, similarly to the need to control pressure in the instrument cavity. One step that we can take in order to satisfy this design requirement of our instrument is to install a heater near the inlet to heat the air to above freezing, in this case 5°C, in order to stay consistent with the temperature of the internal electronic components in the body of the instrument and ensure that there is no temperature gradient. This heater is connected to a thermocontroller with an updated voltage regulator chip that allows it to output a smaller voltage difference than before. The thermocontroller is a tuned PID loop that takes the temperature at the thermistor location near the heater, and changes the voltage output to the heater to maintain the temperature at the setpoint. It has been used successfully in previous instruments in order to regulate temperature, so we felt comfortable applying it to our instrument design, especially with the improvements mentioned above.

At the beginning of the design stage, we had to decide among many different options to heat the air, some of which the lab group had used before, and some that they had not. After talking with the course staff and conducting further outside research, we chose a thermofoil heater instead of a cartridge heater in the end. Using a thermofoil heater to control the temperature gave us flexibility to choose the heater that matched our power requirements and promised ease of installation (the heaters often have an adhesive backing), relatively low cost at \$68 per heater, and an extremely light weight of 0.15 oz. There are a number of reputable companies that sell thermofoil heaters, with most of the lab heaters being ordered from Omega, but Minco had the largest selection that we saw in stock in terms of both power density and the physical size and shape of the heater.

Since we are designing an instrument meant to fly in the lower stratosphere, it is important to keep considerations such as the ambient temperature, pressure, and moisture conditions in mind during the entire design and fabrication process. However, we must also be conscious of the limits of in-lab testing when considering the how we will test the prototype instrument. For instance, we expect to encounter temperatures around -60°C in the region of the lower stratosphere where we will be collecting concentration data with the final instrument. In the lab, although it is possible, it will be difficult to reach these low temperatures and introduce a great deal of extra work into the process of evaluating our heater performance. Therefore, in order to test the performance of the heater control system, we decided to raise the temperature of

the air in the lab by 20°C above room temperature. This relatively arbitrary set point gives us a basis to test the general characteristics of our heater in a controlled setting with a reasonably low temperature and hopefully determine whether the thermocontroller can maintain a consistent downstream flow temperature.

In order to determine the heater that we would need to heat the air at room temperature, we had to take into account the flow rate necessary to maintain a 1 Hz. measurement rate in our instrument, which at the time we made this decision was 2.28 L/s because that was the volume of the cavity for the previous year's ES96 class. Once the cavity team used Norton's software to generate a final optical configuration, they came up a cavity dimensions that were even smaller than those we used for our initial calculations. Using the estimated operating pressure, flow rate, air density, and specific heat of air during in lab testing, we calculated the heater power density necessary to raise the temperature of the air flowing through a 12.7 cm. section of copper pipe by 20°C. In addition, we used heat transfer equations to find an estimate of the surface temperature of the copper pipe necessary to achieve our desired downstream air temperature change.

$$\dot{m} = Q\rho$$

$$Q = \left(2.28 \frac{L}{s}\right) \times \left(\frac{1}{1000} \frac{m^3}{L}\right) = 0.00228 \frac{m^3}{s}$$

$$\rho = \frac{PM}{RT} = \frac{(6000 \text{ Pa}) \times (0.02897 \frac{\text{kg}}{\text{mol}})}{\left(8.314 \frac{\text{m}^3\text{Pa}}{\text{K} \cdot \text{mol}}\right) \times (298.15 \text{ K})} = 0.070122 \frac{\text{kg}}{\text{m}^3}$$

$$\dot{m} = 0.00228 \times 0.070122 = 1.5988 \times 10^{-4} \frac{\text{kg}}{\text{s}}$$

After some simplification, we can then calculate the constant surface heat flux, assuming a change in temperature of 20°C, and a tube of length L=5in=0.127m and diameter D=0.5in=0.0127m:

$$q_s'' = \frac{\dot{m}c_p\Delta T}{\pi DL} = \frac{(1.5988 \times 10^{-4})(1005)(20)}{\pi(0.0127)(0.127)} = 634.2 \frac{W}{m^2} = 0.409 \frac{W}{in^2}$$

Following the example 8.4 in the thermodynamics textbook from Mike, can solve for the heat transfer coefficient,  $h$ , then plug this into Newton's law of Cooling:

$$k_{air} = 0.0263 \frac{W}{mK} @ 300K$$

$$Nu_d = \frac{hD}{k} = 4.36$$

$$h = 4.36 \left(\frac{k}{D}\right) = 4.36 \left(\frac{0.0263}{0.0127}\right) = 9.03 \frac{W}{m^2 K}$$

With an outlet air temperature of 45°C for  $\Delta T = 20^\circ\text{C}$ , we find the surface temperature of the 5 in. long copper pipe section to be:

$$T_{s,o} = \frac{q_s''}{h} + T_{m,o} = \frac{634.2}{9.03} + 45.0 = 115.2^\circ\text{C}$$

Based on the calculations above and the further analysis of the flow conditions both during in-lab testing and in the lower stratosphere we decided to order a 0.5x2 in. 19.6 W thermofoil heater from Minco. This maximum power from the heater will overshoot our needs slightly, but ensures that we have flexibility in regulating the temperature with the control board, as we can vary the power output by the heater by changing the voltage across its leads.

We attached the thermofoil heater to a 0.5 in. outer diameter, 0.375 in. inner diameter copper pipe, choosing copper due its high thermal conductivity so that the heat from the

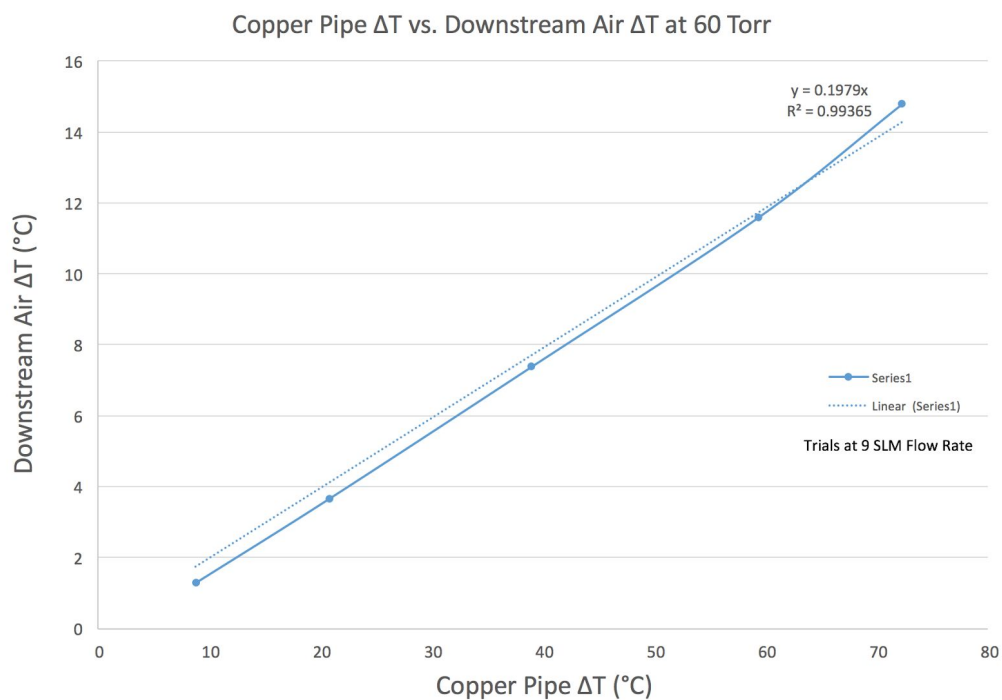
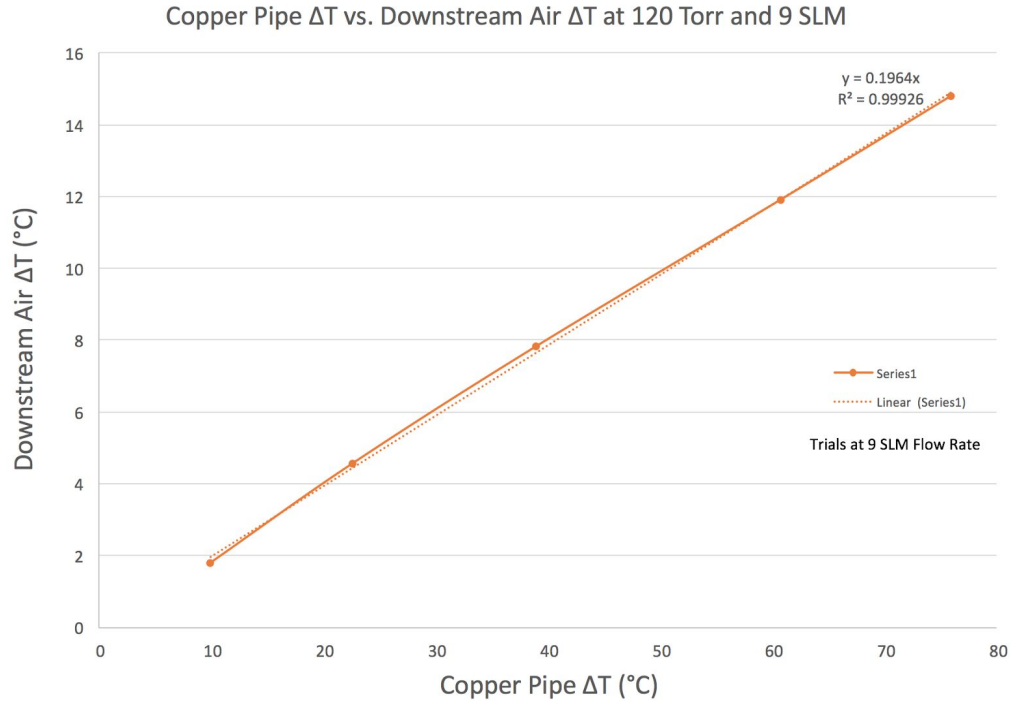
thermofoil heater would be transferred quickly to the air flowing through the copper tube. We also chose the thinner-walled of the two options for the 0.5 in. copper pipes because less copper to heat means we can change the temperature of the pipe more rapidly, ensuring responsive temperature regulation of the downstream flow.

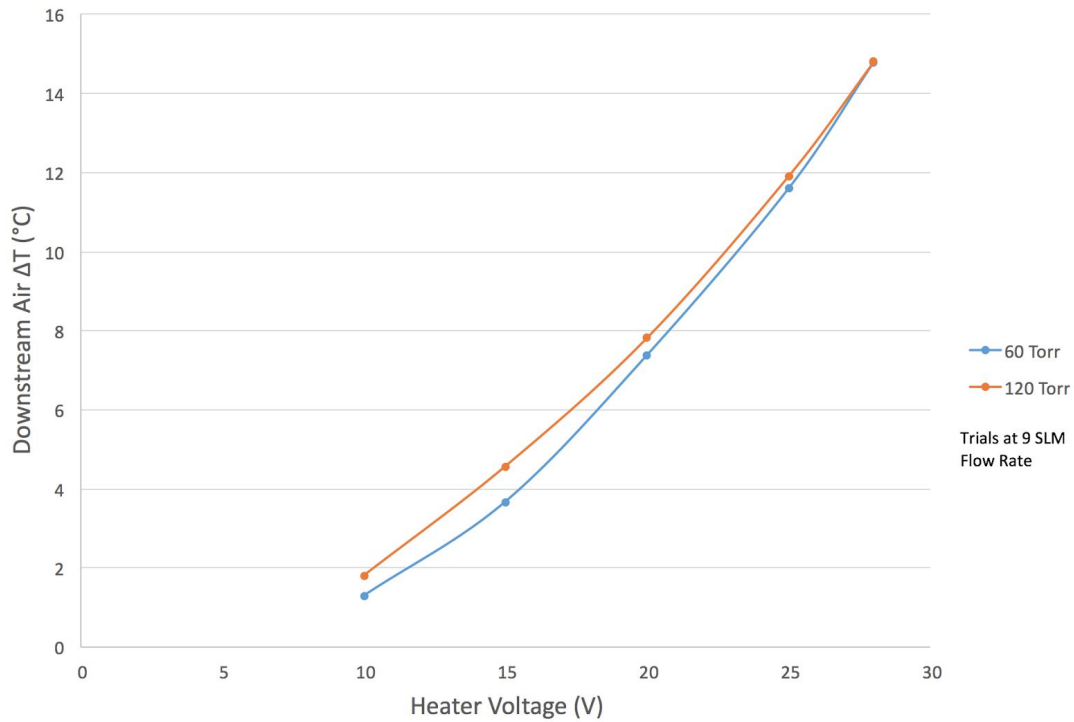
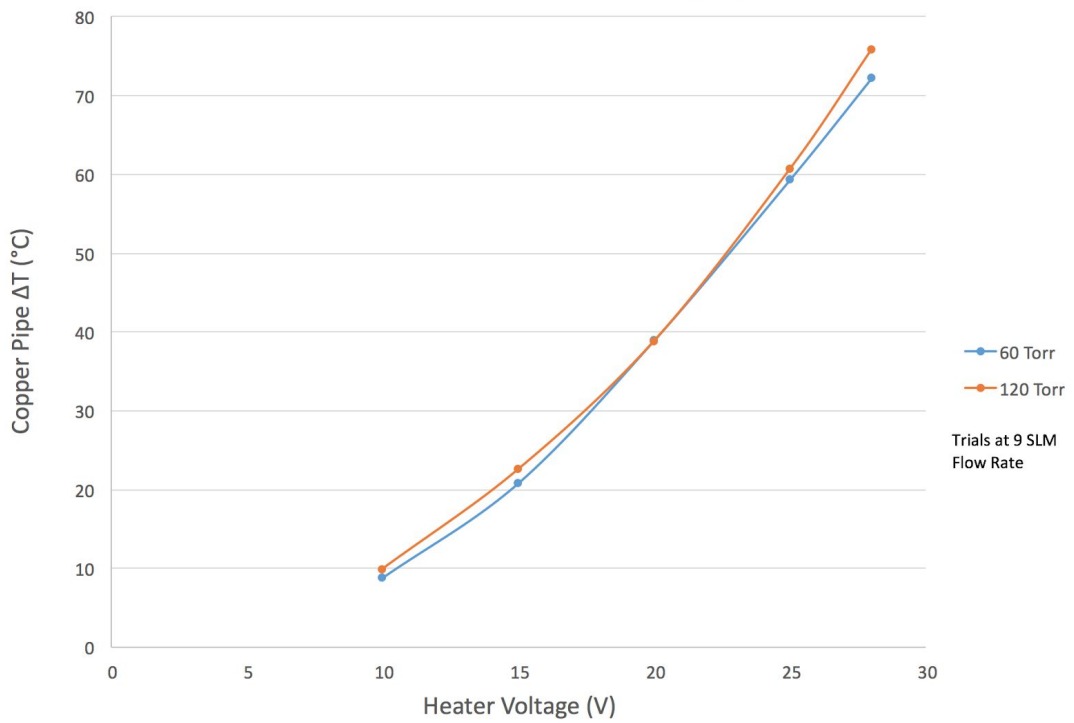
To characterize the performance of the thermofoil heater and ensure that it meets our stated requirements for the prototype instrument, we set up a test rig in the lab that resembled the connections between the valve, the pressure transducer, the teflon and copper tubing, and the pump that we used in our final instrument.

In order to get meaningful results from this experiment we wanted to test our thermofoil heater under a set up that closely resembles that which will be implemented in our payload. This meant that we wanted to have our pump regulating a set flow through a roughly straight set of tubing so that losses were minimal. We were able to achieve a setup which resembled our envisioned atmospheric setup except for temperature conditions. This was acceptable though, because we were recording the change in temperature rather than a set start and end temperature. To test the suitability of our thermofoil heater we wanted to test the change in temperature that could be achieved downstream of the heating under varying conditions. This would simulate the temperature the inlet tube could get our atmospheric air to before entering the cavity. To test this, we heated our thermofoil heater for 5 minutes with a set flow rate of 9 standard liters per minute, under varying pressures to see the change in temperature we could achieve. We chose to use the 9 liters per minute because we thought that by using the higher flow rate, it would make the air harder to heat, so if the heater could achieve this then we would know it is suitable for our application.

Our original plan for the experiment was to run a set voltage through our thermofoil heater and observe the change in downstream temperature that resulted from this. The problem with this plan was that because the copper has such a high heat capacity, it would continue to heat, albeit slowly for low voltages, for such a long time that the final temperature wouldn't settle for a very long time. Due to time constraints in the lab we couldn't wait for this experiment to run out and observe the results, so we modified our experiment so that we observed the change in temperature over a 5 minute time span.

Our experimental data for this experiment yielded the following plots:



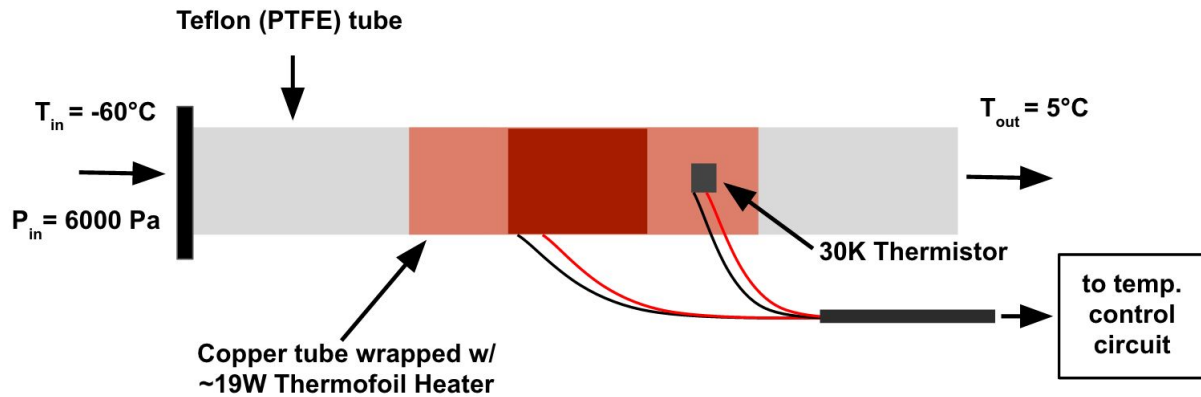
Downstream Air  $\Delta T$  vs. Heater Voltage at Varying PressureCopper Pipe  $\Delta T$  vs. Heater Voltage at Varying Pressure

Contrary to our calculations prior to the lab, the pressure of the air flowing through the tube does not seem to have any significant effect on the downstream temperature change. This is evident in the overlapping lines in both of the temperature versus voltage plots as well as in the similarity of the trendline slopes in the second two plots. We set the y-intercept for the trendline to be zero in both of these plots to establish zero downstream air temperature change for zero tube temperature change, but this only slightly affected the trendline equations.

From the trendline equations we calculated, due to the apparent linearity, we can likely extrapolate to see what copper pipe temperature we will have to set on the thermocontroller to reach our goal delta T for in-lab testing of 20°C. At 60 Torr,  $y=0.1979x$ , where y is the change in downstream air temperature and x is the change in copper pipe temperature, so  $\Delta T = 20.0 \div 0.1979 = 101.06^\circ\text{C}$ . This change in temperature certainly seems to be within the reach of our thermofoil heater, since the temperature of the pipe was still rising steadily at 28V when we stopped the trial at 5 minutes, yielding a change in temperature for those trials at both pressures of over 70°C. Since we insulated the copper pipe and PTFE tubing sections, we expect that our heater will not only be able to heat the copper pipe to over 100°C, but that it will be able to maintain this temperature with the aid of the thermocontroller.

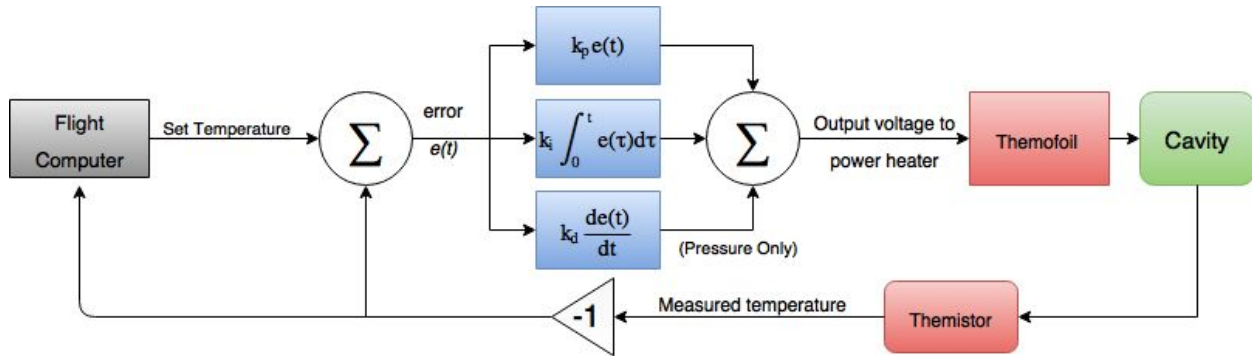
Once we extrapolated to calculate the copper pipe temperature set point for the thermocontroller, we next set out to investigate the length of copper pipe necessary to keep the temperature below 60°C on the surface of the copper pipe. After a discussion with the teaching staff, we believed this was necessary because we were told that all instrument components should be kept at a temperature below 60°C so that they are safe to touch during operation. We reasoned that we could achieve the same heating of the downstream air with a lower pipe temperature by attaching the thermofoil to a longer pipe so that the air was in contact with the warmed pipe surface for a longer period of time. For each trial in the second experiment, we measured the temperature of the pipe at the center near the thermofoil heater and at the upstream end of the pipe next to the compression fitting to gain some insight into the temperature gradient across the pipe for lengths of 30 cm. or less (by 5 cm increments). We measured the temperature change of the pipe at both locations and recorded the time that it took to raise the temperature of the downstream flow by 20°C. The results of this experiment were less conclusive than the previous one, and after talking further with the teaching staff, we realized that the higher temperature of the pipe was acceptable because it was insulated with Nomex, so we chose to heat the exterior of a 15 cm pipe in our final design. After testing and installing the heater and thermistor, we wrapped the copper pipe segment as well as all the other PTFE tubing from the inlet to the cavity in Nomex insulation to minimize heat losses through the system. The cavity itself will incorporate a similar temperature control board with a heater and thermistor, but our

heater located near the inlet does the majority of the temperature regulation so that our HCl detection instrument can function properly. A rough schematic of the design is pictured below:



### 3.2.4.2 Feedback and Control

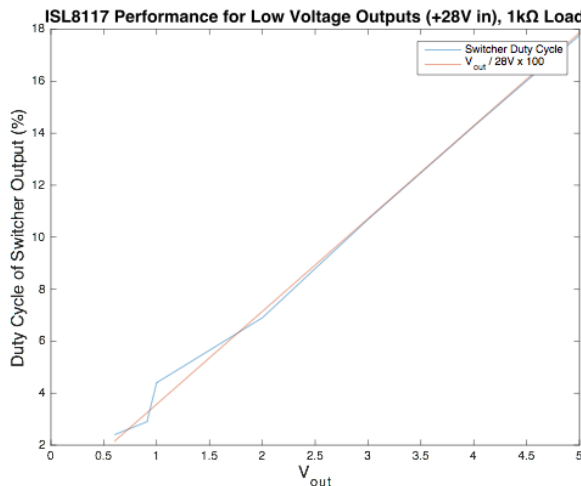
The thermofoils and copper piping provide a mechanism to heat the incoming air, but it is also necessary to automate the instrument to take in a desired temperature and regulate the system to remain at that temperature without further user input. We achieve this goal through the use of a PID (proportional, integral, derivative) controller board, which is an electronic circuit board that takes in power, desired set point, and a voltage reading from a thermistor, and it outputs power to the thermofoils to heat incoming air. A basic overview of PIDs is given in the block diagram below:



The current temperature reading is compared with the desired temperature to produce an error signal, which is fed into blocks to calculate the accumulated error over time (integral), the rate of change of the error (derivative), and the current error (proportional). Each of these three signals are scaled according to constants assigned to each block (carefully choosing these constants is called “tuning” the PID), and then they are summed to produce an output signal which is ultimately fed to a voltage regulator to provide power to the thermofoils. On a circuit board, these blocks are realized using op-amps, capacitors, and resistors.

For our thermal control board, we started with a board the Anderson Lab has used on previous missions. By Marco's suggestion, however, we chose to make a few modifications to it. The Anderson lab's board cleverly uses a switching voltage regulator (traditionally used for efficient conversion of an input voltage to a desired output voltage for power supplies) to take in the output signal of the PID feedback loop and use it to drive power across the thermofoils. The switching regulator on the old boards, the LTC1624, has previously had difficulty regulating precise temperatures. These chips regulate voltage by quickly switching the input voltage on and off at a specific duty cycle (amount of the time the pulse is ON over the entire period of the pulse); for low voltage outputs, however, the pulses need to be very short, and this chip has been observed "skipping" pulses when it needs to drive small amounts of power to the thermofoils. Specifically, Marco said that in the past they had seen the chips behave unreliably for duty cycles under 10%. As an alternative, Marco found a new chip, the ISL8117, which research suggested might not exhibit the "skipping" behavior.

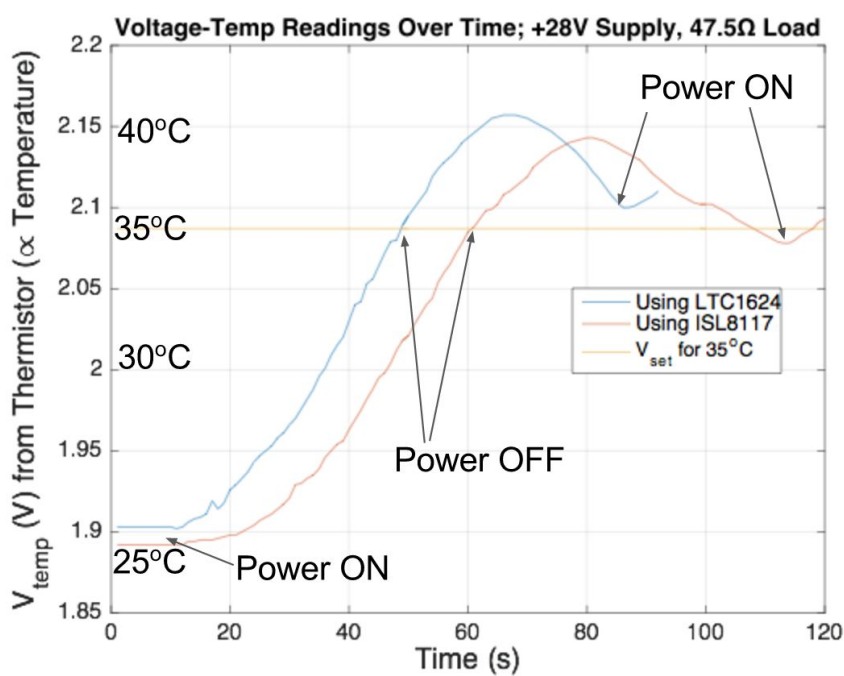
The process of integrating and evaluating the new chip had two steps. First, we used the evaluation board for the chip to simply test its reliability providing low voltage outputs across a simple  $1\text{k}\Omega$  load. Using +28V power supply, we soldered in a potentiometer to the resistor-divider part of the test board which sets the output, and then changed the resistance to drive a range of outputs across a  $1\text{k}\Omega$  resistor. Results from this test were promising, and we found that this chip provides stable, reliable outputs for duty cycles down to 5%, an improvement on the LTC1624. A graph of the switcher duty cycle vs. output voltage is seen below:



The red line shows the exact percentage of  $V_{\text{out}}/V_{\text{in}}$  (the expected switcher duty cycle), while the blue line shows the actual duty cycle measured on the switching pin of the chip. The measured deviates from the ideal line very slightly starting around 7%, and at 5% starts to deviate further. Overall, however, these initial results were promising.

Next we had to integrate the chip with the old board. For initial tests, this simply involved connecting the output of the PID with the feedback pin of the chip on the evaluation board, as

well as connecting the voltage inputs, outputs, and ground. To evaluate the performance of the new chip, we subjected the board with the new chip and a copy of the old board to the same experiment and compared the results. We created a test load with a  $47.5\Omega$  power dissipating resistor with a  $30k\Omega$  thermistor taped to it, which would act as the system the boards were regulating the temperature. Both loads were subjected to a step signal, and we observed the response. The voltage signal indicating temperature was measured during the both responses and can be seen plotted below:



In this graph we see the temperature (given by a voltage signal from the thermistor) over time of the load when driven by the new (ISL8117) and old (LTC1624) regulator chips. Also on the Y axis are labels indicating the temperature associated with certain voltages. Both tests, the loads started at about  $25^\circ\text{C}$  and were driven to a set temperature of  $35^\circ\text{C}$ . For both chips, we see that when the load is connected, the temperature rises steadily as power is driven across the load. Both chips shut off when the temperature reading matched the set temp, but there was overshoot in both cases (as there is a slight delay between the temperature of the power resistor and the temperature of the thermistor). As the loads cooled, however, we observed that the old chip actually began driving power across the load before the temperature had dropped back below the set-point, causing the temp to continue to rise more, suggesting that, with this chip, the temperature of the load will oscillate around a point offset from the desired temperature. In the new chip, we found that when the temperature of the load fell below the set point, the chip output went into a low power mode, in which it was driving low power ( $2-3\text{V}$ ) across the thermofoils. Due to latency, however, the temperature continued to fall slowly, and when the voltage reading was  $.007\text{V}$  below the set point, the regulator went to full output power again, which quickly

brought the load temperature back up, at which point the power turned off. Due to constraints with data measurement in the lab, it was difficult to perform this test for long enough to watch the load temperature converge to a single value; still, the low power mode and careful turn-on timing of the ISL8117 suggests it is an improvement over the old chip.

In the next steps, the board should be redesigned to implement the new chip along with the necessary specific resistors, capacitors, and inductors needed for its optimal operation. The PID should also be tuned to minimize overshoot and have the temperature converge to the set temperature in the step response as quickly as possible.

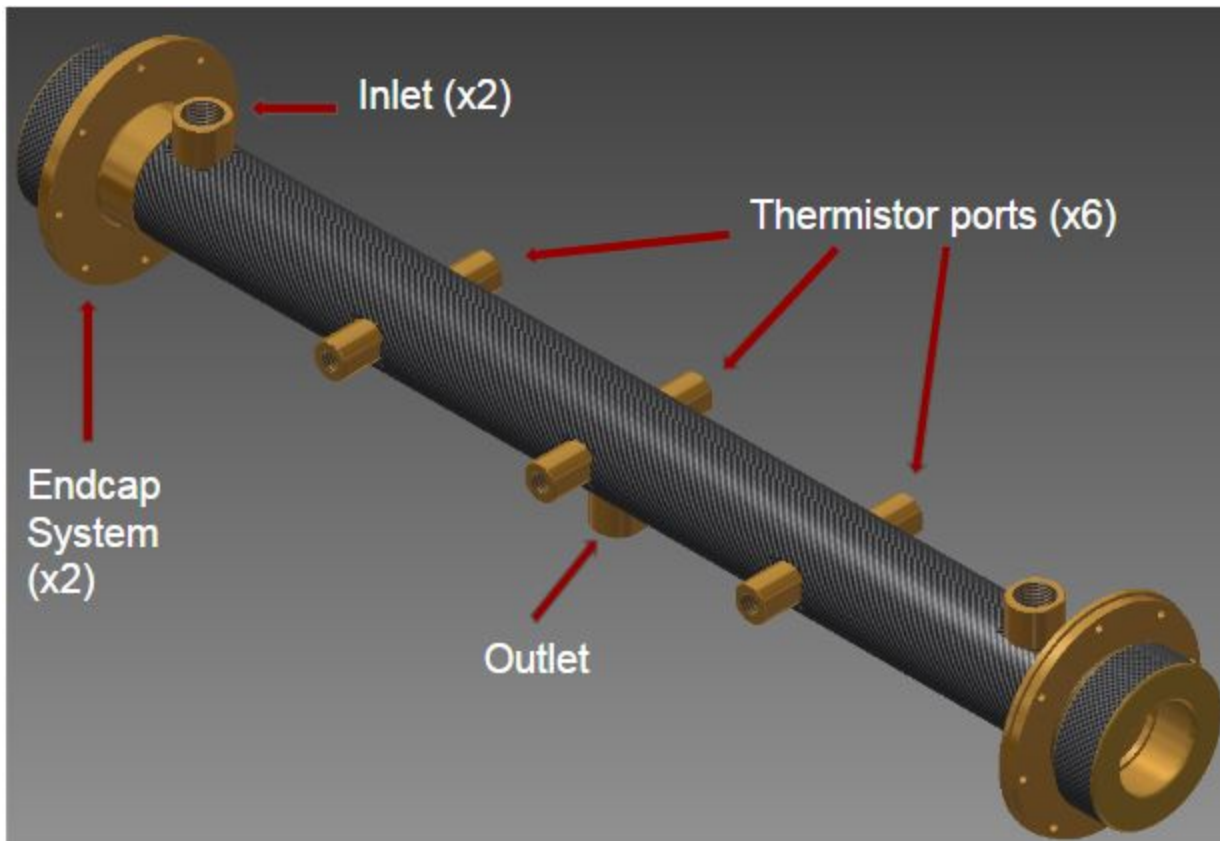
### 3.3 ICOS Cavity Design and Optics

The cavity subsystem has two main goals:

1. Provide an inert, temperature- and pressure-controlled environment for the sample gas to be analyzed by the photons of the laser;
2. house the highly-reflective optics and keep them in alignment with the laser fore-optics and detector.

To accomplish these goals, work on the cavity was split into four main subsections:

1. Optical configuration design
2. End-cap system (optics mounting system)
3. Temperature and pressure sensing & sample inlet/outlets
4. Cavity material and coatings



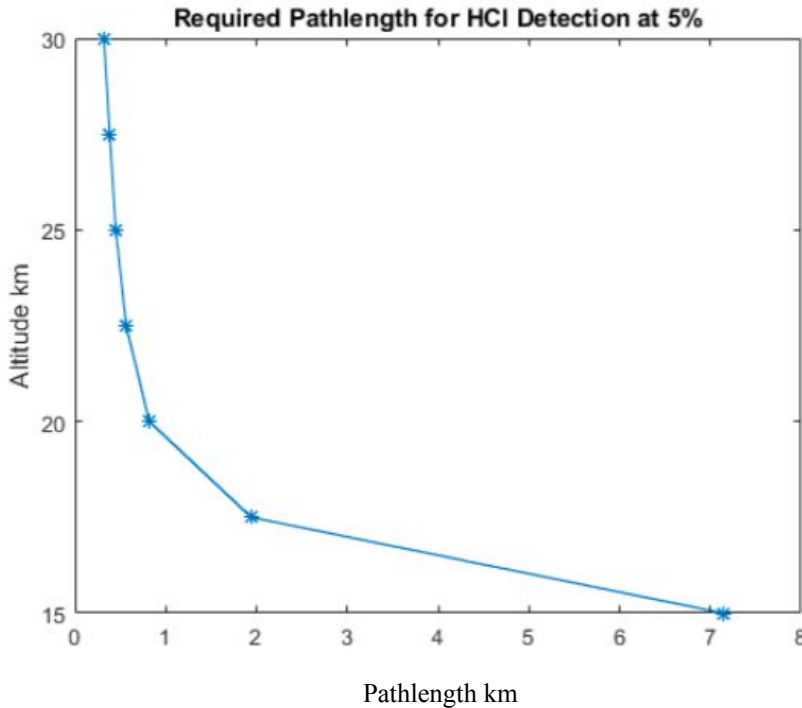
*The cavity subsystem includes a carbon fiber cell, 6 thermistor ports, 2 inlet ports and 1 outlet port, and 2 endcap systems which house 2 highly-reflective mirrors.*

#### 3.3.1 ICOS system

##### 3.3.1.1 Effective pathlength

The driving force behind the design of the ICOS system cavity is the effective pathlength that it produces. Referring to the graph below, it is illustrated that in order to detect HCl with an accuracy of five percent at various altitudes in the stratosphere, an effective pathlength of seven

kilometers will be necessary. The cavity is designed to achieve an acceptable pathlength while maintaining a relatively low cell volume. The larger the cell volume the more energy is required to move the air sample inside; therefore, having a low volume is crucial when considering the overall power requirement of the system.



### 3.3.1.2 Mirror reflectivity

The effective path length can be thought of as the length one pulse from the laser travels inside the cavity before it is dispersed. For the ICOS system, it can be calculated using the equation below.

$$\ell' \cong \frac{\ell}{L + \alpha}$$

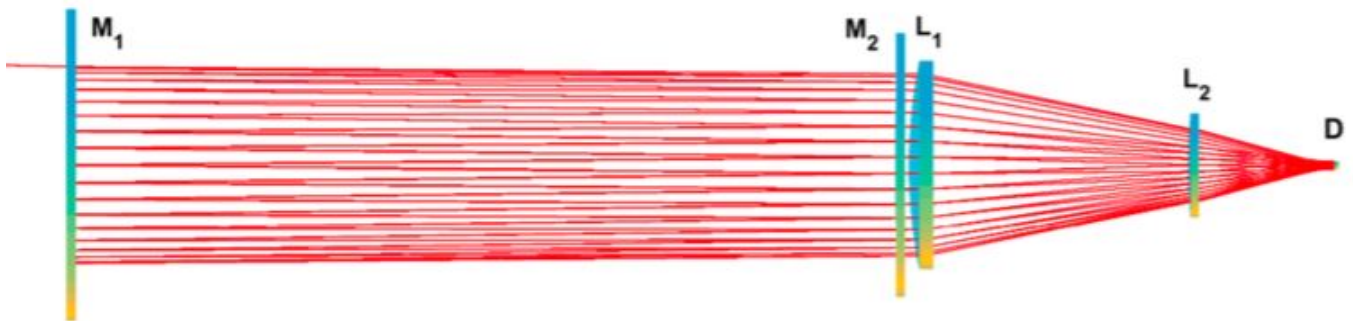
With lower case L representing the cavity length, L representing mirror loss, and alpha representing the absorption of the cell (which can be approximated to be zero), we see that the effective path length is determined by the length of the cell and the reflectivity of the mirrors. The effective pathlength is not the only property of the cavity that is determined by the cavity length and mirror reflectivity. The length of our cell will be roughly 50 centimeters, which correlates to a mirror loss of roughly 70 parts per million. These parameters also determine the

ringdown time of the cavity, which can be thought of as the amount of time the laser beam stays inside the cell. The ringdown time, which is a crucial value to account for when deriving detector specifications, can be calculated using the equation below.

$$L = 1 - e^{-\ell/c\tau} \cong \ell/c\tau$$

### 3.3.1.3 Optical configuration

How exactly does the laser travel approximately seven kilometers in a cell that is only half a meter long? When the beam first enters the cavity, it is incident on the back of the first mirror. Due to the mirror's reflective nature, a small portion of the laser (roughly .0001 percent), will enter the cavity while the remainder will be reflected away. Once the laser is inside the cavity, it travels to the second mirror where the same process occurs; however, in this case the small percentage of the laser that gets transmitted through the second mirror is the signal which will be focused onto the detector. This process occurs thousands of times per laser wave as the beam is reflected back and forth between the two mirrors on opposite sides of the cell. A crucial key to the system is avoiding overlapping of the beam inside the cell which generates noise in the measurement. To avoid this problem, the beam enters the mirror off-axis and a circular spot pattern is generated as the beam traverses the cell. This process is illustrated below.



### 3.3.1.4 Optics specifications and re-injection

Using a mathematical model of the ICOS system generated in Matlab, our group was able to derive multiple appealing configurations using two different sets of mirrors. The specifications for those optics are as follows:

Mirror 1 radius of curvature: 200cm; 100cm

Mirror 2 radius of curvature: 300cm; 400cm

Mirror diameters: 1.5in; 2in

The material of choice for these mirror is Zinc Selenide, specifically because the material has nice transmissive properties and is insoluble in water -- meaning that water vapor in the atmosphere will not destroy the mirrors. Note that a coating will be applied to make the mirrors highly reflective. The configurations generated with these mirrors will be capable of achieving the target pathlength of seven kilometers have volumes of roughly a liter -- a remarkable improvement from previous ICOS systems.

Referring back to the nature of the system, it seems unfit that the majority of our laser beam be lost before it even reaches the inside of the cavity. To solve this problem, our group plans to use a re-injection mirror which will be placed before the first mirror. This re-injection mirror, likely made of aluminum with a reflective coating, will re-reflect the beam back toward the cell every time the front mirror tries to reflect it away. This would vastly increase the power measurement on the detector by multiplying the amount of times the detection process occurs in the cell by the amount of times the laser is reflected off of the re-injection mirror.

### 3.3.2 Cavity

#### 3.3.2.1 Material & Structure

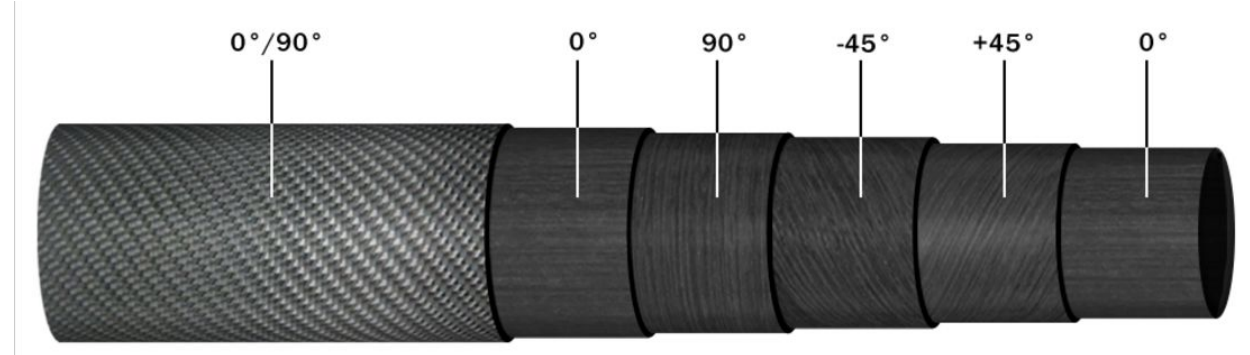
In keeping with the overall instrument design goals of minimizing mass, volume, and power requirements, an optimal cavity would be made of low density material to minimize mass and have a low volume to minimize the space occupied by the cavity and to minimize the power required by the pumps to draw air in at a sufficient sampling rate. Cavity volume was determined primarily by the mirrors' diameter and reflectivity, but density is a function of the cavity material. (Note: the optical configuration considered for the HCl prototype cell featured circular mirrors, so all cavity material considered was cylindrical with a circular cross section).

After developing a short list of Aluminum 6061, Aluminum-Lithium, and Carbon Fiber Reinforced Plastic, the cavity team chose CFRP tubing provided by Rock West Composites due to its low density of 1.57 g/cm<sup>3</sup> (only 58% the density of Al-6061).

Mechanical properties of the carbon tubing were also considered: the largest external mechanical loads experienced by the carbon tube would result only from the weight of the endcap/mirror system secured to the ends of the tube (approximately 6 N); the mechanical properties of the carbon tube resulted in a flexural stiffness factor of safety on the order of 10<sup>6</sup>

The largest internal force the tubing would experience would occur during vacuum testing of the cavity in the lab: the largest internal pressure change would be approximately 14.7 psi if the pump were able to pull a complete vacuum; however the Internal Pressure strength of the tube is specified at 1260 psi, which results in a factor of safety of approximately 17.7.

The layup schedules of the carbon fiber tubes were also examined. Tubes are laid up with some fibers (also called plies) oriented along the z-axis of the cylinder ('axial' or '0°' fibers), others oriented at 90° to the z-axis of the cylinder, and others oriented at ±45° (see diagram below for ply orientations).



*Source: <https://www.rockwestcomposites.com/45111>*

The layup orientations are primarily for structural and strength requirements; however, as noted above, strength was not an issue in selecting the ply orientation due to small magnitude of loading.

However, ply orientation was important for machinability of the tube. Although the carbon fibers are very strong in tension, they are prone to fraying and delamination under shear stress, and most drilling/milling processes would subject the fibers to shear. We knew we would need to mill regions of the tube for hardware connections, so we chose a tube with an outer 'fabric' outer layer -- one which includes both a 0° and a 90° which is designed to reduce the risk of delamination during machining.

A final physical property dependent upon ply orientation which we did not examine in detail until after ordering the tube was the thermal conductivity. We hypothesized and tests confirmed that carbon fibers conduct heat better along the fiber axis than perpendicular to it. Tests carried out on a smaller-diameter tube (with a different layup schedule) indicated a thermal conductivity on the order of 200 W/(m\*K) along fiber axes and around 50 W/(m\*K) for an individual layer of 90° fiber surrounding 4 layers of axially-oriented fibers. Although these conductivities are in the same ballpark as thermal conductivity for aluminum 6061 (167 W/(m\*K)), the conductivity in the radial direction from outer wall to inner wall was measured as approximately 6 W/(m\*K), which is much lower than that of aluminum (which is an isotropic material). The low radial thermal conductivity of the carbon tubing may make it difficult to regulate the temperature of the interior cavity wall from a thermofoil glued to the exterior surface of the tube. Multiple heaters on the exterior of the cavity (or a different heating method altogether) may be required based on the thermal conductivity data.

Note 1: the thermal conductivity data presented above is for Rock West 1.25in ID x 1.506in OD tubing with only 0° and 90° plies (SKU 45569). Additional tests would need to be

carried out for the tubing chosen for the HCl prototype cell which includes  $\pm 45^\circ$  plies (Rock West 1.75in ID x 2.00in OD tubing, SKU 45111) to measure its thermal conductivity.

Note 2: see “Thermal conductivity of carbon fiber tubing” experiment report for details on the test conducted on SKU 45569.

Once SKU 45111 was chosen as the tubing, we began designing the hardware interface surfaces for the inlet/outlet bosses, thermistor ports, and endcap system. Each of these surfaces was designed for ease of assembly with the aluminum parts and was machined out of the carbon fiber tube. The overall length of the tube was determined by the ray-tracing software which optimized path length, mirror reflectivity, and radius of curvature. The placement of the inlets, outlet, and thermistors will be discussed in a following section devoted to Ports and Sensors.

### **3.3.2.2 Coating & Bonding**

The interior of the cavity must also be non-reactive with HCl. The instrument will detect HCl concentrations at approximately 50 parts per trillion, so the interior surfaces of the cavity and ports must not remove any HCl from the sample air because this would change the concentration of HCl (or perhaps eliminate it entirely) and make the measurement useless. The coating also needs to withstand a wide temperature range of 190 K to 310 K (190 K: coldest temperature occurring in the lower stratosphere, where the suspended payload would dock with the drive module for recharging; 310 K: hottest temperature during a summer day in the U.S. Southwest on a tarmac waiting for launch). Whereas the interior surfaces of metal cavities for previous instruments could be electroplated with a non-reactive coating, electroplating was not an option for a composite cell. Therefore other coating options were explored.

The aluminum ports and endcaps must also be bonded to the composite tube. The bonding surfaces exposed to the sample air must also be coated in the inert coating, so we searched for a material that could serve as both an inert coating and a bonding agent.

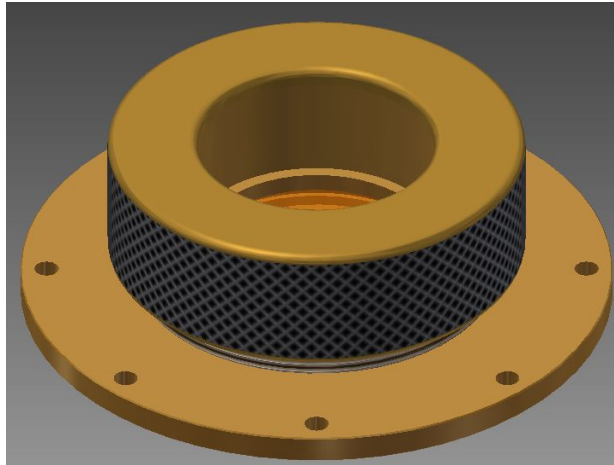
An epoxy provided by Masterbond and designed for inertness with strong acids and for cryogenic operations was chosen as the optimum coating and bonding agent for this cell. Masterbond EP29LPSP has an operating temperature range from 4 K to 408 K, and it is inert to acids and bases. It is also specifically designed for bonding metal parts to composite parts, which makes it a good choice for bonding the inlet/outlet ports, endcaps, and thermistor ports to the carbon tube.

### **3.3.2.3 Size**

As discussed above, one of the goals of cavity design was minimization of volume in order to minimize the pump power required to achieve the minimum acceptable sample refresh rate (the rate at which the entire cavity volume has been replaced by a new sample) and minimize the volume of the entire instrument. The cell volume is dictated by the cell length and the mirror geometry. This cell featured circular mirrors, which led to a cylindrical cavity. The cell length

was determined by the effective path length provided by the mirrors; the effective path length is a function of the level of reflectivity of the mirrors. After accounting for radii of curvature, bonding gap for the epoxy, and other hardware geometry, the carbon tube length was chosen to be .5525 m. The mirrors for this cell were selected to have a 2.00 inch diameter, so the cell outer diameter was chosen to be 2.00 inches with a .125 inch wall thickness for machinability.

### 3.3.3 Endcaps

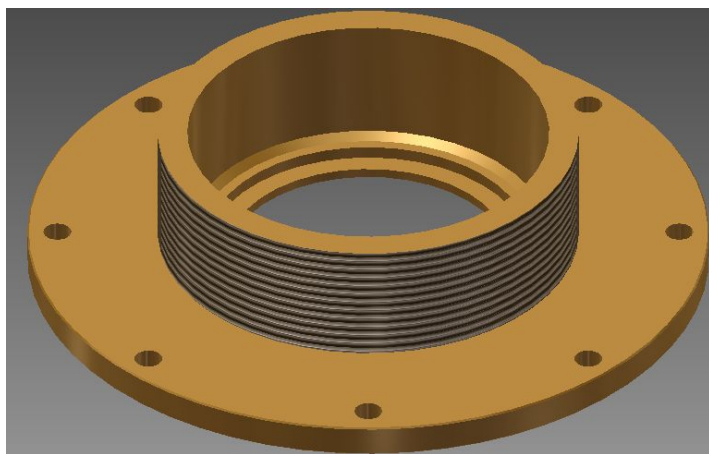


*This is an assembly image of the endcaps, including the mirror.*

#### 3.3.3.1 Structure

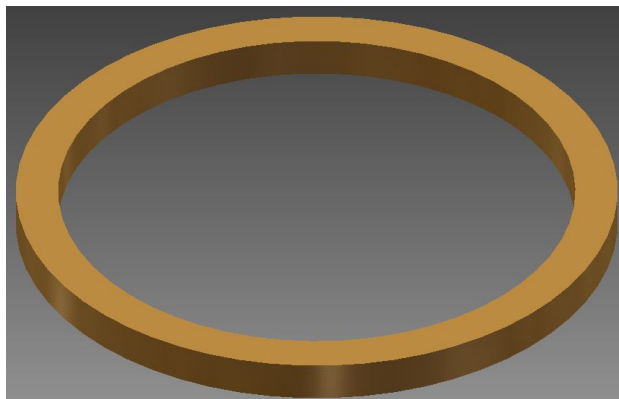
For the endcap the objectives of the design was to create a structure that was easy to assemble so that the assembly could be taken for maintenance or testing purposes, yet held the mirrors in place and sealed the cavity correctly to avoid any leakage of our air sample. The sealing ability is very important in order for the data we record to be valid in the scientific community. Keeping these objectives in mind, we went with a structure that is made up of four individual components:

Base



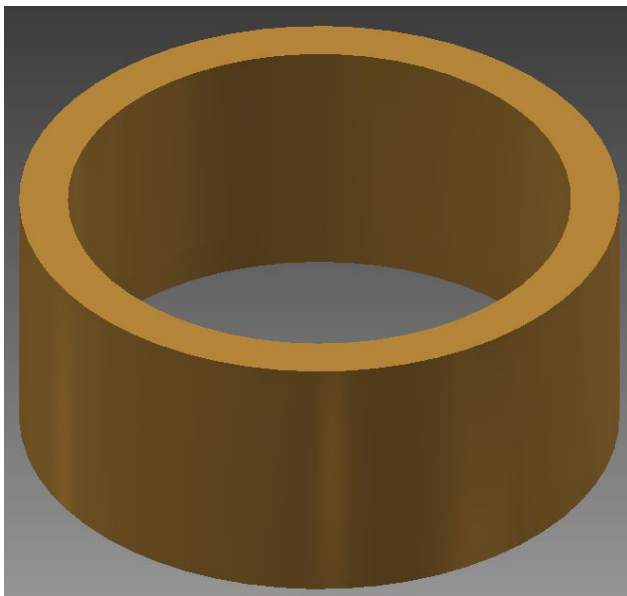
The base of the structure is where the mirror is placed. It contains a small lip to place the mirror of .004 inches deep to avoid the mirror from being displaced horizontally and can be made to great precision due to the fact that the tolerance for the diameter of the mirror is held to a small tolerance. Additionally the base has the holes through which screws are placed to connect the end cap assembly to the end plate (see interface with cavity). The base also has a vertical structure that allows it to interface with the endcap cap through threaded screws. Inside the base all other parts are located.

Shim



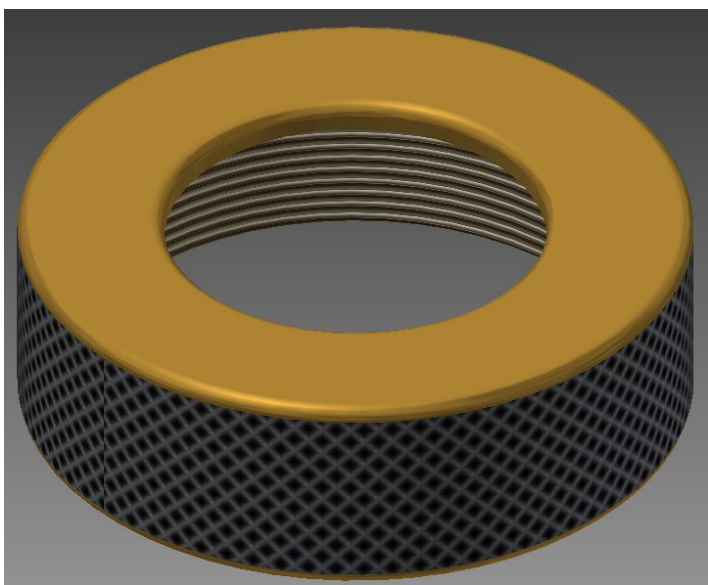
The shim is a circular ring placed over the mirror and under the sleeve. This part was not included in the initial design but added on when we found out the thickness tolerances for the mirror vary much more than initially expected, so we needed to have a way of counteracting this possible thickness difference and that was done through the shim since it can be easily lathed to the appropriate thickness.

Sleeve



The sleeve of the endcap is a circular piece that interfaces with the shim, but also has a lip that is in charge of compressing the O-ring. It fits directly inside the base of the endcap.

Cap



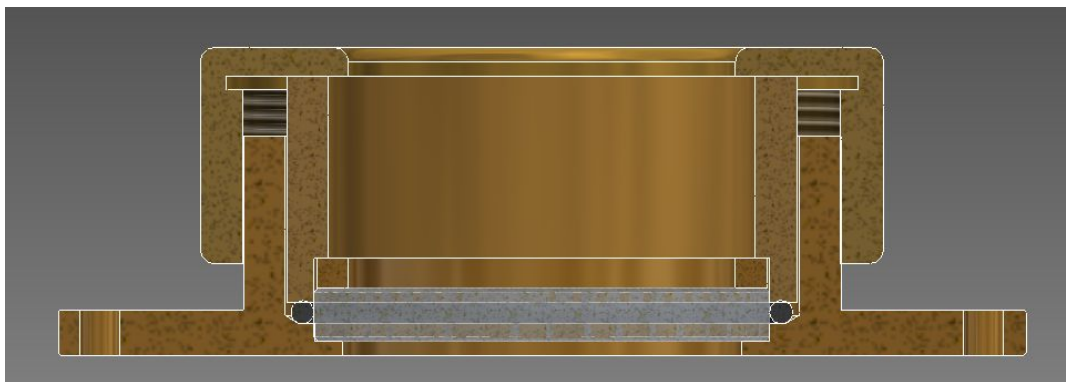
The cap, like stated above, screws onto the base. It makes sure all the other components stay within the endcap and interfaces with the top of the sleeve by pushing it down. It is not solid all the way through horizontally since it needs to allow the space through which the laser will come in and hit the back of the mirror. It has a knurl finish on the outside to make it assembly easier. This occurs because a rough surface allows less possibility of slip between the material and the hand of the person making the assembly.

Note: A drawing of each part with all critical dimensions will be found in the appendix.

### 3.3.3.2 Materials

The material of the endcap needed to be light yet easy to manufacture as well as have no corrosion problems so we decided to go with aluminum T6061. The only part that is not made out of aluminum is the cap due to the fact that the cap and the base both have threads that connect them together. Aluminum on aluminum interfacing can corrode on small surfaces compromising how well the threads stay together and if kept screwed for long enough maybe even making it incredibly difficult to disassemble. A metal that has no corrosion issues with aluminum is brass, so the endcap cap was made of this material. Going forward we want to reduce mass by selecting a plastic to make the cap, but we need to make sure it is strong enough to push the sleeve and not deform.

### 3.3.3.3 Sealing



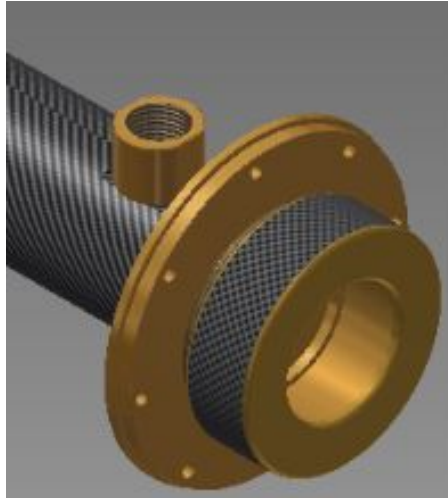
*A cross sectional view of the endcaps assembly, including the mirror and the O-ring for sealing purposes*

The sealing mechanism chosen was an O-ring on the sides of the mirror. This was chosen since this mechanism is not permanent. In order for the O-ring sealing to be effective, the o-ring must be completely compressed and take up the entire volume of space left between the mirror, the base and the sleeve. As is visible in the assembly, the nominal dimensions for each part is made such that there already is some interference between the sleeve and the O-ring to assure compression. This sealing is achieved when the lip of the sleeve compresses the O-ring after it is pushed down by the cap, which in turn has been moved downwards due to its rotational motion as it screws on to the base. The base was designed so that it had that volume where the O-ring was to be placed and that volume was small enough to allow the O-ring to be compressed completely. Since the tolerance for the diameter of the mirror is well known, it was possible to create this space precisely, in terms of its horizontal configuration. The O-ring selected for this was a Silicone 2-136 in Class III.

### 3.3.3.4 Sealing test

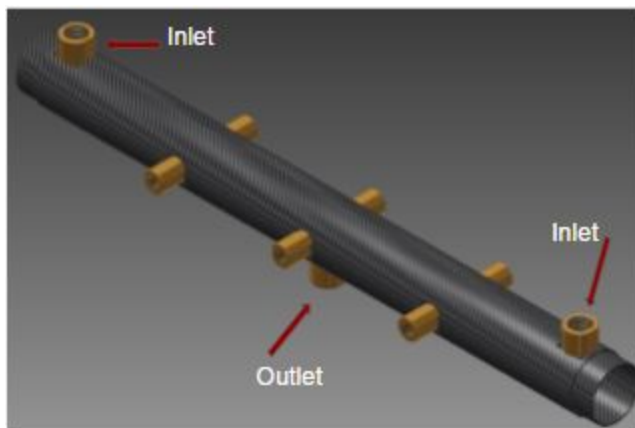
The endcap sealing capability was tested through a pressure test. We used blank mirrors created out of aluminum for testing purposes. Since two end cap assemblies were created each one was tested. In order to test the endcap fully assembled was screwed on to a testing module that was already present in lab, which through a valve connected to a tube and eventually a pump. In order to gage what the pressure lost was from the tube and valve connections, the test module was connected to a circular plate which would not allow any leakage. The pump was turned on to evacuate the testing module of any air. After it reached 8.1 Torr, the valve was closed off so the pump was no longer connected to the testing module, after 10 minutes the pressure had increased to 8.4 Torr. This change of 0.3Torr is our baseline loss. With endcap assembly number one, the initial evacuated pressure was 8.8 Torr and within two minutes the pressure had increased to 131.5 Torr. These results show the endcap was not sealing properly, in other words, the O-ring is not compressed completely and there is space for the air to move between the outside and the test module. With endcap assembly number two, the initial evacuated pressure was 8.2 Torr and after 10 minutes, the testing module reached 9.0 Torr. Giving a net pressure change, that takes into account the baseline change of 0.5 Torr. These results were consistent with experiments in the past and fall within the necessary sealing for our purposes. After a tolerance analysis given the measured values of each shim, the slip of each sleeve, and the mirror, it was determined that in endcap assembly number one the lip of the sleeve, just touched the top of the O-ring and so did not compressed the O-ring at all. Through the same calculations it was determined that the second assembly was able to compress the O-ring's diameter by 5%. The ideal diameter compressions for the O-ring are 10% so new shim thicknesses were calculated. For assembly number one, the shim must be 0.120 inches thick with a tolerance of +/- 0.002 inches. For assembly number two the shim must be 0.124 inches thick with a tolerance of +/- 0.002 inches.

### 3.3.3.5 Interface with cavity



The endcap uses screws and eight equally spaced holes to interface with the endplate of the cavity. This endplate is designed to be epoxied on to the ends of the cavity tube. It is therefore 0.005 inches to 0.008 inches larger than the tube in radius. This plate is also made an  $\frac{1}{8}$  of an inch wide between the end of the tube and the beginning of the endcap base.

### 3.3.4 Ports and sensors

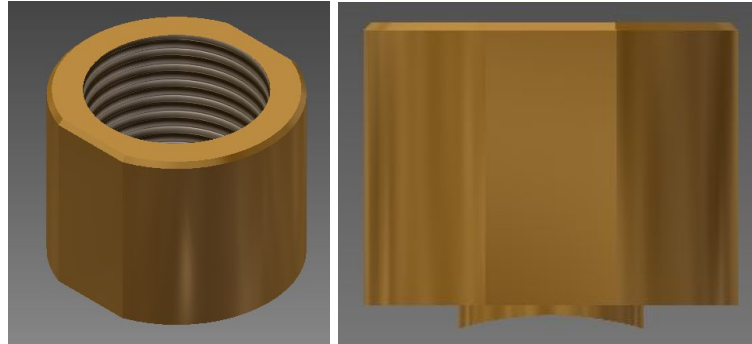


*Cell with temperature ports and inlets & outlets*

#### 3.3.4.1 Inlets & outlets

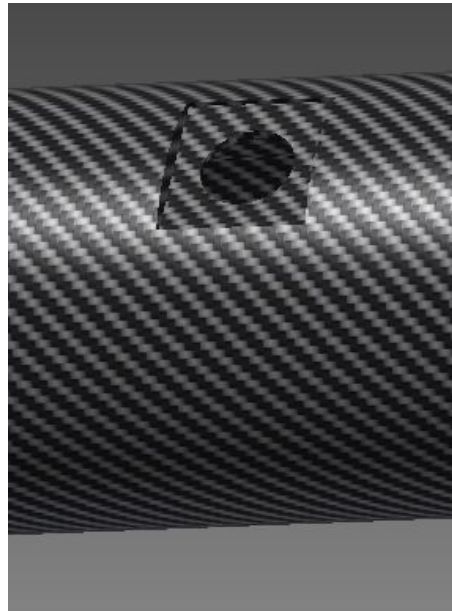
In the cavity we chose to design for two inlets placed at the end of the cell, as close to possible as the optics in the cell. The choice of two inlets encourages air mixing in the cell more than just one inlet, and the location near the optics is important to encourage air mixing

especially near the optics and to prevent dead zones at the ends of the cell. It is important that the air is well mixed within the cell because this ensures that the concentrations of various molecules (namely HCl) in our sample air are representative of the concentrations in all of the air in that region of the atmosphere. In addition to the two inlets in the cavity we also have one outlet located opposite the inlets to allow air to escape. We designed an inlet/outlet boss piece made of aluminum in order to interface our inlets and outlets with the pump tubing.



Inlet/outlet boss

The inlet/outlet boss will be attached to the cavity by machining the port locations on the cavity to be flat surfaces, resulting in a lip on 2 edges. That lip will keep the inlet/outlet boss from rotating during or after the attachment process. They will be attached using epoxy to the flat, machined surface of the cavity.



Cavity surface

These bosses have  $\frac{1}{2}$ " female NPT threads that will accept the male end of a Swagelok SS-810-3-8TMT Tee Connector, whose opposite end will connect to the pump tubing. The third connection on the Tee will be used for a thermistor, discussed in more detail below.

### **3.3.4.2 Temperature sensor (exterior)**

In order to control cavity temperature we will have one thermistor on the surface of the cavity whose purpose is to control the two thermofoil heaters on the surface of the cavity, discussed in more detail below. For this thermistor we chose a NTC (negative temperature coefficient) with a 100K Ohm resistor from Digi-Key (part number 495-2125-ND). We chose this in order to maximize our dissipation constant, which will, in turn, minimize the noise that will end up in our data. It is imperative that we minimize self-heating and therefore noise in order to ensure that our data collection is accurate.

### **3.3.4.3 Cavity heating**

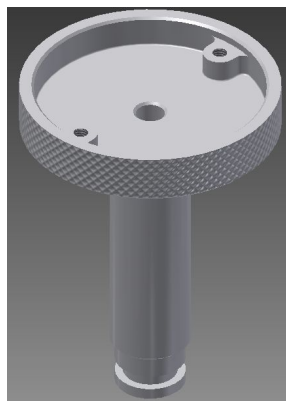
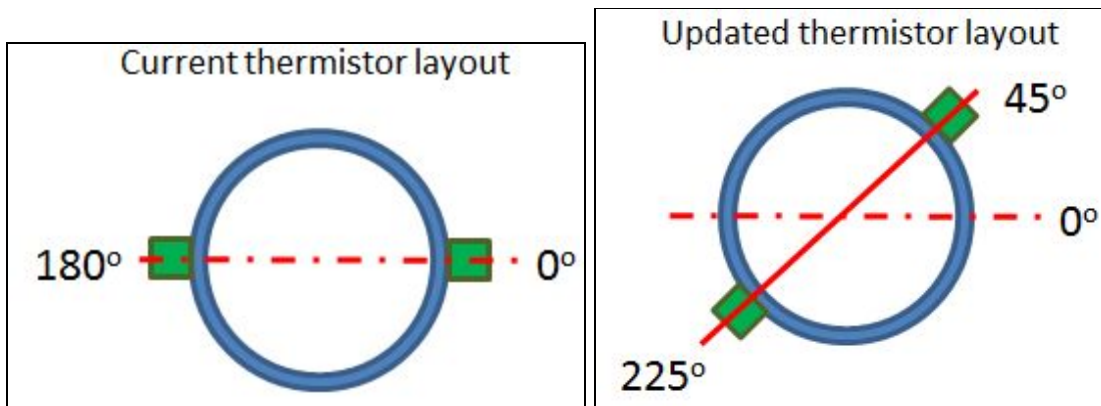
As mentioned above, our cavity will be heated with two thermofoil heaters. It is important that the cavity be heated to the correct temperature for our data collection. These thermofoil heaters will be temperature controlled by the exterior thermistor on the surface of the cavity. They will effectively heat up the cavity and the air in it, preventing or mitigating temperature gradients along the cavity.

### **3.3.4.4 Temperature sensors (interior)**

Besides the exterior thermistor, we will have nine additional thermistors measuring temperature inside the cavity. We have six thermistors placed along the length of the cavity, and one thermistor at each inlet and outlet. The purpose of these thermistors is to ensure that there is no temperature gradient along any part of the cavity, meaning that the temperature coming into the cell (at both locations), coming out of the cell, and at all points along the cell, should be within a  $0.1^{\circ}\text{C}$  range. For these thermistors we will use the same thermistor NTC, 100K Ohm thermistor from Digi-Key that we chose for the exterior thermistor. This thermistor detects the temperature with small glass bead that would not interfere with the path of the laser in the cavity. We have designed two variations of the housing for the thermistors—one for the three thermistors at the inlets and outlet, and another for the six in-cavity thermistors. A small hole will be drilled in the center of each of these housings from end to end and filled with epoxy to hold the actual thermistor. The thermistors located at the inlets and outlet will connect with the perpendicular branch of the Swagelok Tee Connector. This connector branch will be machined to increase its diameter in order to allow for a standard size O-ring to fit on the thermistor housing and seal the connection.

The six in-cell thermistors are currently positioned at  $0^{\circ}$  and  $180^{\circ}$  with respect to the horizontal (see schematic below). This does not provide any information about a vertical

temperature gradient within the cell. Therefore later iterations of the cell will have the thermistors positioned at 45° and 225° to provide vertical gradient data.



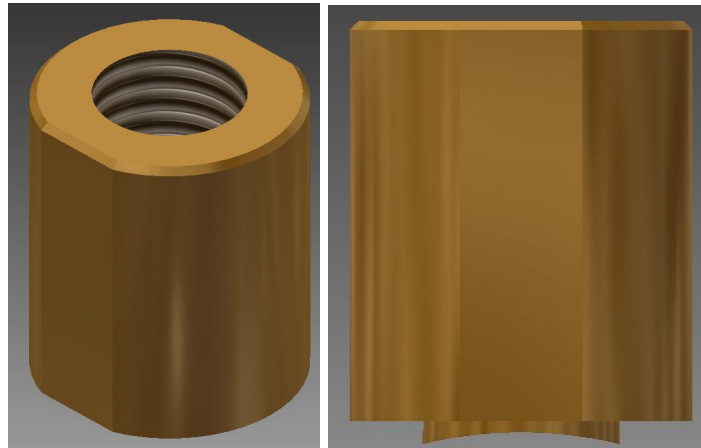
Thermistor housing for inlets/outlet

The six in-cavity thermistors will sit in a similar housing to the ones at the inlets and outlet except that their housing is threaded and will screw into its own thermistor boss.



Thermistor housing for in-cavity thermistor ports

The housing for each of these thermistors has a top that holds a circular circuit board to control the electronics for the thermistor, and will ultimately interface to the flight computer to read out the temperatures in the cavity.

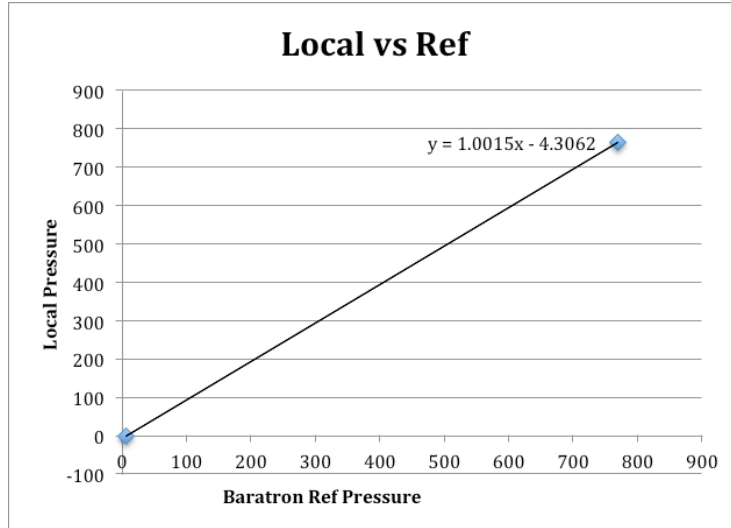


Thermistor boss

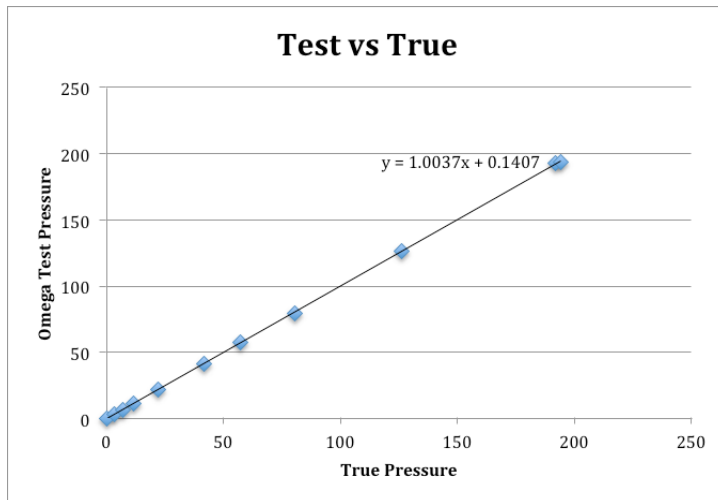
These six thermistor bosses are very similar to the inlet and outlet bosses, in that they are made out of aluminum, contain a female thread, and will be attached to a machined-flat surface of the carbon fiber tube using epoxy.

### 3.3.4.5 Pressure sensor

There will be a pressure sensor located at the outlet of the cell in order to ensure that the cell is at the correct pressure. For this pressure sensor we chose a high-accuracy absolute pressure transducer with a 0-5Vdc output and a cable connection from Omegadyne (part number PX409-005A5V). The transducer measures from 0-5 psi. The pressure transducer is connected just below the outlet via a  $\frac{1}{4}$ " NPT thread from a plastic Swagelok Tee Connector whose other two ends will attach to the pump tubing since the end of the pressure transducer is a  $\frac{1}{4}$ " male NPT. In order to test the accuracy of this pressure sensor we set up a reference between this sensor and another one (Baratron MKS) we had in the lab. Because the Omegadyne pressure transducer does not read pressures as high as atmospheric, we used the Baratron pressure gauge as a reference, first finding the linear fit and offset between the Baratron pressure gauge and the true pressure, by using zero pressure and atmospheric pressure as reference points.



We then used this linear fit of “true pressure” to compare to our Omegadyne pressure sensor.

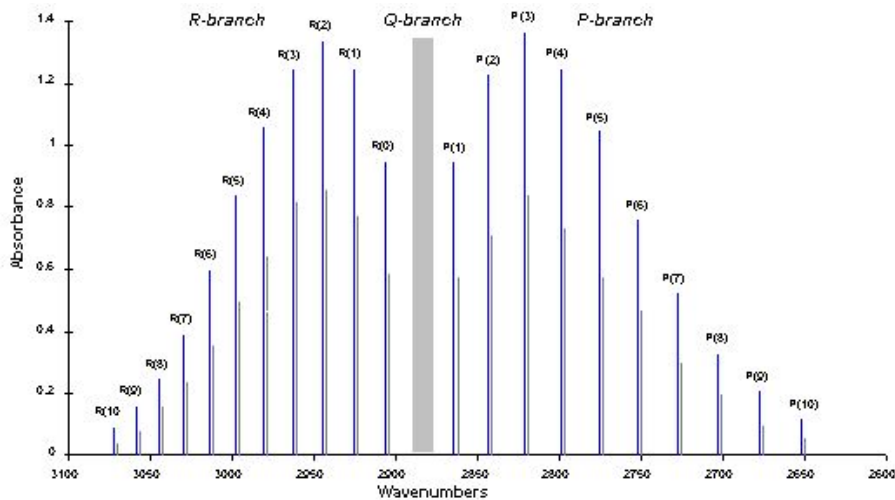


The result was a slope of 1.0037 and an offset of 0.1407. The slope shows good accuracy, while the offset is a little higher than we may have hoped, it is probably at least partly due to experimental error and not solely error of the instrument. In order to get data from our pressure transducer, both in the lab and in-flight, we connected its cables to the flight computer and its data can be read on-screen.

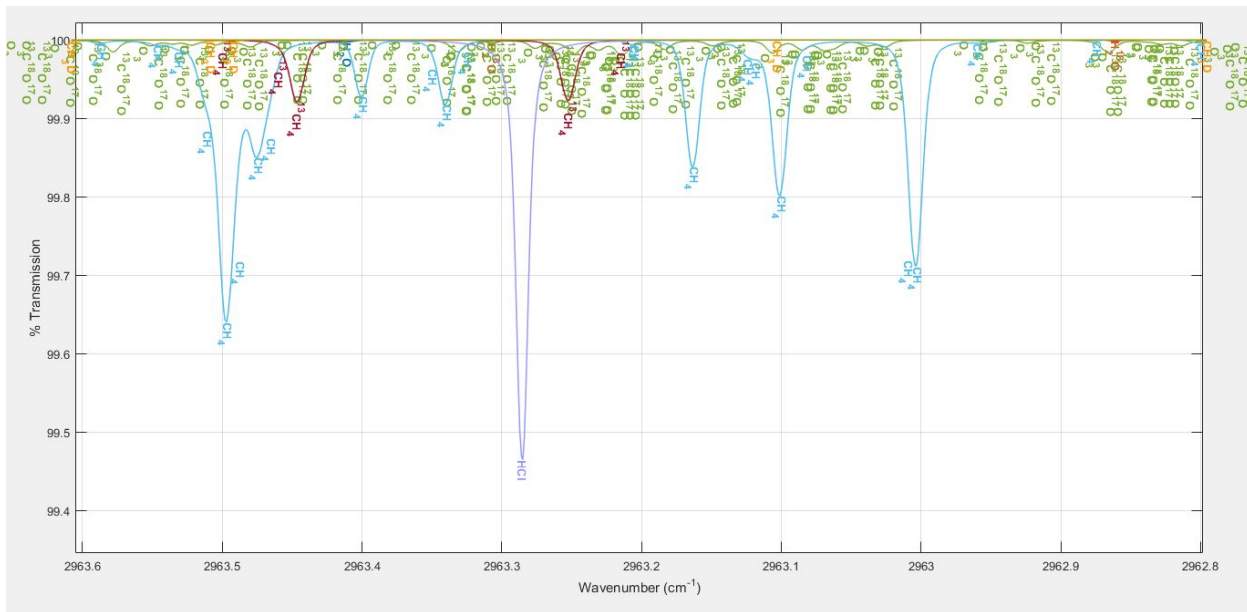
## 3.4 ICOS Laser and Forward Optics

### 3.4.1 Laser Wavelength Choice

In order to detect absorption of HCl, we first needed to find a wavelength at which it is readable. To do so, we analyzed the vibrational-rotational spectrum of HCl pictured below.



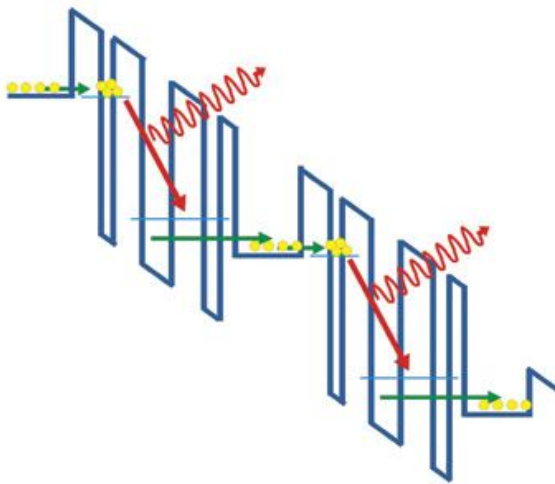
On the x-axis is wavenumber and on the y-axis is absorbance. The various peaks seen on the chart represent wavenumbers at which HCl has particularly high absorbance. As you can see, HCl has a very high absorption characteristic in the mid-infrared region at wavenumbers of about 2700 to 3000. Once we determined this particular range on the IR spectrum to analyze, we then had to search through the spectrum to find a wavenumber at which HCl would have a readable output. The two requirements that we used when searching for the wavenumber were high percent absorption and separation from other molecules' peaks. High absorption would guarantee that we have a very strong and detectable signal. Separation from other peaks would guarantee that interference with other molecules would be minimized. To search through the spectrum for particular candidates, we used a MATLAB program developed by David Sayres of the Anderson Group. This program gathers absorption data from all other molecules that appear in the atmosphere and assembles it onto one graph so that you can see the absorption of a target molecule along with the absorption of other molecules at the same wavenumber. After we discovered several wavenumber candidates, we decided to select a wavenumber of  $2963\text{ cm}^{-1}$  and a wavelength of  $3.375\text{ }\mu\text{m}$ . The absorption graph of HCl along with other surrounding molecules is pictured below. HCl is pictured as the central grey line while other molecules are pictured in various colors.



As you can see, at  $2963\text{ cm}^{-1}$  HCl has a detectable absorption peak and is separated enough from other molecules that interference will not be an issue. The surrounding light blue lines represent methane absorption, but the peaks are far enough away from HCl and its absorption is much lower.

### 3.4.2 Laser Choice

Once we determined an optimal wavelength to detect HCl absorption, we then needed to determine an optimal way to generate a laser at that specific wavenumber. We ultimately decided to use an Interband Cascade Laser. Interband cascade lasers are a fairly new technology and are very similar to quantum cascade lasers. They function by using thin semiconductor materials that are repeatedly stacked in series and function as quantum wells for different electron energy states. A simple model for how these lasers generate photons is pictured below.



As a current is supplied to the laser, electrons begin flowing through these semiconductor stacks. The electrons pass through these semiconductor layers and change energy states, emitting photons with each transition. The stacked structure is particularly useful because one electron can continually produce photons as it “cascades” through the semiconductor bands. Interband cascade lasers are particularly useful for spectroscopic applications as they have high power, output, significant tunability and can be operated at room temperature.

The particular laser we will be using is an interband cascade laser fabricated at the Jet Propulsion Laboratory at the California Institute of Technology. It is a miniature, tunable, solid state laser that allows us to hit our target wavelength in the mid infrared range. The laser package includes a beam collimator and a thermoelectric cooler for built in thermal control. We currently have two of these lasers in our lab. The ICL 57 has very precise output and will be used on the final instrument in flight. The ICL 58 has a more variable output and therefore is being used in our prototype and to conduct laboratory tests.

### 3.4.2.1 Collimator

The beam collimator is built into the JPL-ICL57 laser housing. The collimator narrows the infrared light waves/particles from the laser into an elliptical beam of approximate major axis diameter of 4 millimeters. The divergence of the beam on the major and minor axes is 0.304 degrees and 0.218 degrees, respectively.

We tested the divergence by taking a reading of the laser, using a Spiricon Laser Beam Diagnostics Pyrocam III camera, from two different distances. After looking at the images, it was determined that the laser beam was not spherical, but elliptical. This meant we had to calculate the divergence of both the major and minor axes. The divergences were calculated using the following equations:

$$Y = (h_1 - h_2)/2$$

$$\tan(\theta) = Y/L$$

$$\Theta = \tan^{-1}(Y/L)$$

### 3.4.3 Forward Optics

#### 3.4.3.1 Telescope

The purpose of the telescope is to focus the laser beam from approximately 4 millimeters to approximately 1 millimeter, in order to minimize interference of reflecting beams within the cavity. The telescope system contains two half-inch diameter, positive meniscus Zinc Selenide lenses. For these lenses to shrink the beam fourfold, the focal lengths of the lenses must have a 4:1 ratio. The first lens has a focal length of 50.8 mm, and the second has a focal length of 12.7 mm. These focal lengths create a perfect 4:1 ratio.

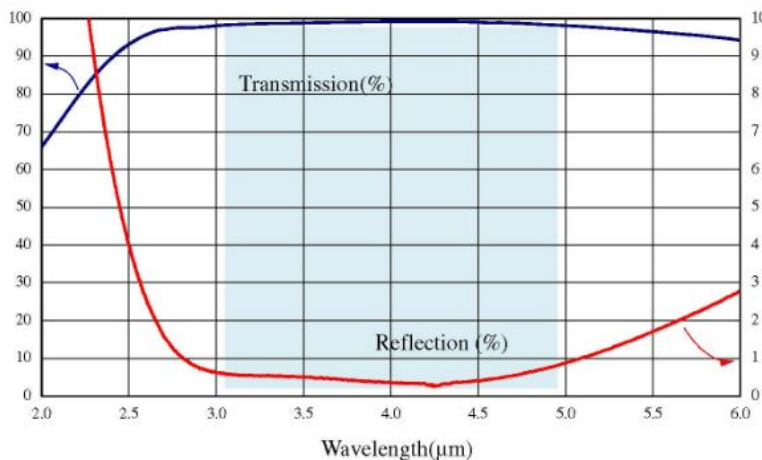
The coating on the lenses is important as well. These lenses are coated with a 3-5 micron anti-reflective coating. This coating allows high percentages of transmittance of light between 3-5 microns, which is useful for this ICOS instrument, as our wavelength is 3.375 microns. The rated transmittance of light at 3.375 microns through lenses with this coating is approximately 98%.



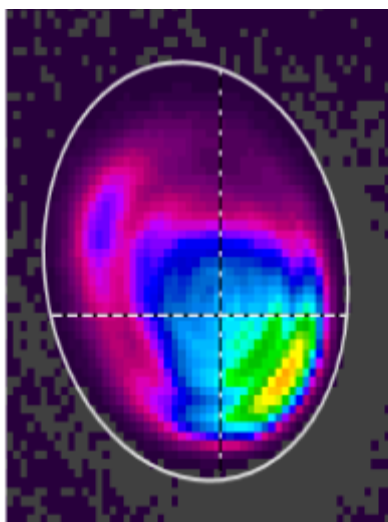
#### ZnSe BBAR 3-5 microns

Part Number: BBAR-ZnSe-3-5

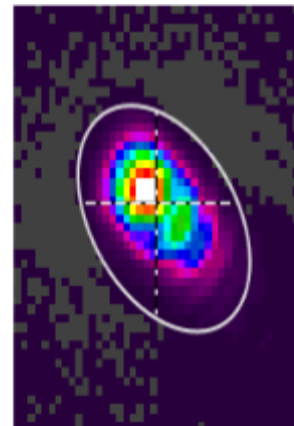
Wavelength (μm)	Reflection avg	Reflection max	Transmission avg	Transmission min
3.0-5.0	<0.75%	<1%	>98%	>95%
3.4-5.0	<0.5%	<1%	>98%	>96%



In order to test the effectiveness of our telescoping system, the two lenses were first mounted in the cage system described below and set up exactly 63.5 mm apart to achieve the desired 4:1 ratio between their focal lengths. The laser beam was then directed first straight into a Pyrocam III Beam Profiling Camera to get the shape of the collimated beam. After measuring the size and shape of the beam, the telescoping lenses were placed between the Pyrocam and the laser. This caused the beam to shrink and the beam size and shape were again measured using an aperture control on the Pyrocam software.



Beam without telescope at 4.5mm diameter



Telescopied beam at 2mm diameter

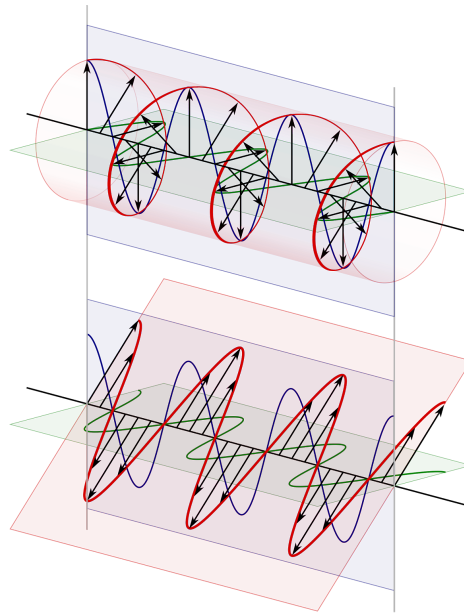
While the methods of the experiment were successful, it was found that the beam only decreased in size to about a 2.25:1 ratio, far less telescoping than was originally planned. Likely, the reason the telescope did work as well as expected is because the 4:1 measurements made were expected for a perfect circular, collimated beam. As seen on the images above, the ICL-57 beam is not perfectly round and thus would not exactly follow the expected telescoping ratio. Still the cavity mirrors were designed with a lower ratio in mind and the 2:1 aspect is still fine to reduce the spotting and will decrease the overall interference of the laser within the cavity. For future reference, better telescoping solutions should be investigated to achieve the ideal 4:1 ratio originally expected by the two positive meniscus lenses.

### 3.4.3.2 Polarizer and Quarter Wave Plate

We expected that one of the main causes of interference in our forward optics would be laser light that is reflected off the different optical components and directed back into the laser aperture. To fix this problem, we use a polarizer and quarter wave plate in series to reduce this

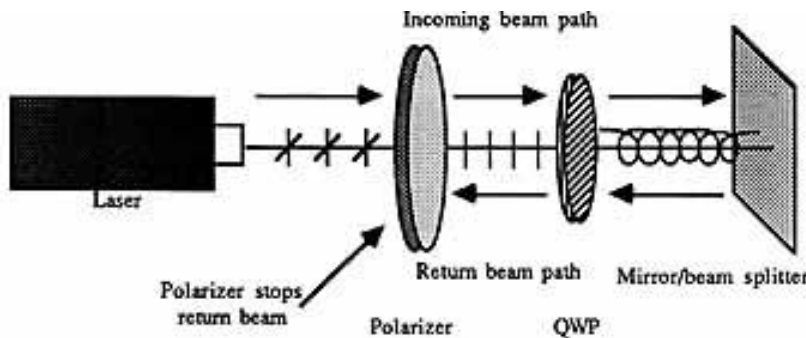
interference. These two components in conjunction are able to change the orientation of the light and filter it out as it travels back towards the laser.

In order to understand how these components work together we first needed to understand the polarization of light. Light acts like a wave and therefore has certain electromagnetic properties. Normally light is unpolarized which means that its waves are vibrating on more than one plane. However, light can be polarized in a number of different ways so that its waves only propagate on desired planes. The two types of polarization we were interested in were linear and circular. Linearly polarized light consists of a single wave propagating on a single plane. Circularly polarized light consists of two waves propagating on planes differing in phase by 90 degrees. Pictured below are figures that allow us to conceptualize these ideas more clearly. On the top is an image of circularly polarized light and on the bottom is linear.



These properties of light along with a polarizer and wave plate allow us to manipulate the orientation of light and only allow desired orientations to pass. The polarizer acts like an optical filter that only allows light on a certain plane to pass through. The quarter wave plate adjusts the orientation of polarized light by 45 degrees and converts linear light to circular light and vice versa. The beam emitted from our laser is already linearly polarized but at an unknown angle. This beam first passes through the polarizer. If the two components are aligned correctly, 100% of the laser power will pass through. The beam then enters into the quarter wave plate, which turns the linearly polarized light into circularly polarized light. This circularly polarized light passes through the entire forward optics and is then reflected back through the system. As it is reflected back, it passes once again through the quarter wave plate, which turns the light back

into linearly polarized light but at a 90 degree phase shift from the original beam. This light which is now perpendicular to the polarizer grating, will not be able to pass through and will be reflected off of the polarizer and into a beam dump. This method ensures that no reflected light will be allowed to re-enter the laser and cause interference and damage. The image below helps to visualize this process.



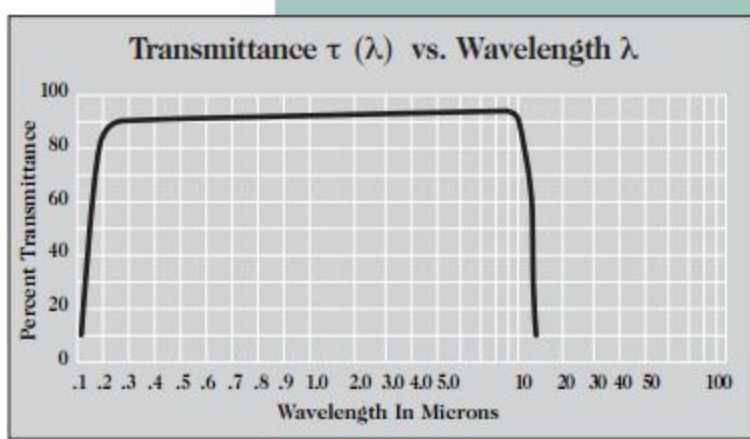
The two components we used were a silicon extreme contrast polarizer that functions with light from wavelengths of 3-5 microns as well as a quarter wave plate that functions with light at a wavelength at 3 microns. Because the wave plate was not fabricated to the specifications of our exact wavelength, we would need to adjust the alignment in testing to make the system work.

The testing for the proof of concept of this method was done using power meters as well as Thor Labs rotation mounts. The light from our laser is already linearly polarized but at an unknown angle. We wanted our beam to be polarized at 45 degrees to the vertical. The 45 degree orientation would compensate for the imperfect wave plate by allowing us to only adjust it with one degree of freedom rather than at a compound angle. To achieve this alignment, we first aligned the polarizer at 45 degrees and rotated the laser until we achieved 100% power, which would mean that the laser and polarizer were aligned at the same angle. Next, we added the wave plate between the power meter and polarizer and adjusted the pitch angle until we achieved 50% power. We chose 50% power because the circular light consists of two waves at 90 degree separation. The polarizer would only let one of these waves pass through once the correct alignment was achieved. The one wave would consist of 50% of the beam's total power. The testing of these two components was successful, as we were able to achieve a correct orientation of all components.

### 3.4.3.3 Beam Splitter

The fore optics need a beam splitter in order to separate the beam into two sub-beams - one to go to the cavity, and one to go to an etalon crystal. The reason we need to send part of the beam to an etalon crystal is so that we may test the wavelength that is coming out of the JPL-ICL 57, so we can verify we are using 3.375 microns.

The beam splitter we used is simply a barium fluoride wedge lens (with a 30-minute angle). With a wavelength of 3.375 microns, this wedge ideally would split the beam into one beam with around 8% power that is reflected off the lens, and one beam with 92% power that is transmitted through the lens. However, after testing this system using a power meter, it was found that the percent reflected was 9.95%, the percent transmitted was 88.99%, and the percent absorbed was 1.11%. It is important that there is a large enough power for the etalon detector to be able to give a clear reading, but we also do not want to compromise how much power passes through to the cavity.



### 3.4.3.4 Cage System

After determining the appropriate set of optical components needed to correctly manipulate the laser beam before entering the cavity, we needed to implement a mechanical system capable of housing the optics and allowing precision alignment of each individual component. We decided to implement a modular 30 mm cage system using both stock parts from Thorlabs and several custom-machined pieces. In order to ensure correct alignment of the laser, wave plate, and polarizer we utilized specific rotation mounts for each. (Note: we use the terms yaw, pitch, and roll to describe the rotational control of each mount.) Starting with the laser, we needed a rotation mount that allows for roll rotation adjustment to align the vertical polarization of the laser with that of the polarizer optic, thus we utilized a Thorlabs CRM1P - Precision Cage Rotation Mount with Micrometer Drive for 1 inch optics.



Next, we needed to mount the polarizer optics at a 45 degree angle from perpendicular with the laser in order to divert the unpolarized light away from the rest of the optics. Furthermore, the mount needed roll-rotation control in order to align with the laser as well. For this we designed a custom machined mount plate for a RSP-1 Rotation Mount for 1 inch Optics to be secured to. This mount plate fits into the bottom of a 60 mm cage cube and has a protruding rectangular extrusion that the rotational mount rests flush against in order to ensure the rotational mount is oriented at 45 degrees from perpendicular with the laser beam. A 60 mm cage cube was used because the RSP-1 rotational mount was too large to fit in the standard 30 mm system used throughout the rest of the fore-optics cage system.



Following the polarizer, the waveplate needed precision pitch-rotation control in order to correctly circularize the laser beam meeting the optic. For this we used a 30 mm cage cube with a B4CRP - 30 mm Cage Cube Precision Kinematic Rotation Platform mounted on the side. We attached a standard 1 inch optical mount to this rotation platform to enable precise yaw-rotation alignment of the wave plate.



The last rotationally-dependent mounting system needed was for the beam splitter. We used a CP360R - Pivoting, Quick-Release 1 inch optic mount to support the wedge optic designed for use as a beam splitter. This allows us to easily aim (via yaw-rotation) the wedge at a 45 degree angle in order to divert a fraction of the beam into the etalon crystal and the rest of the beam into the steering mirrors towards the cavity.

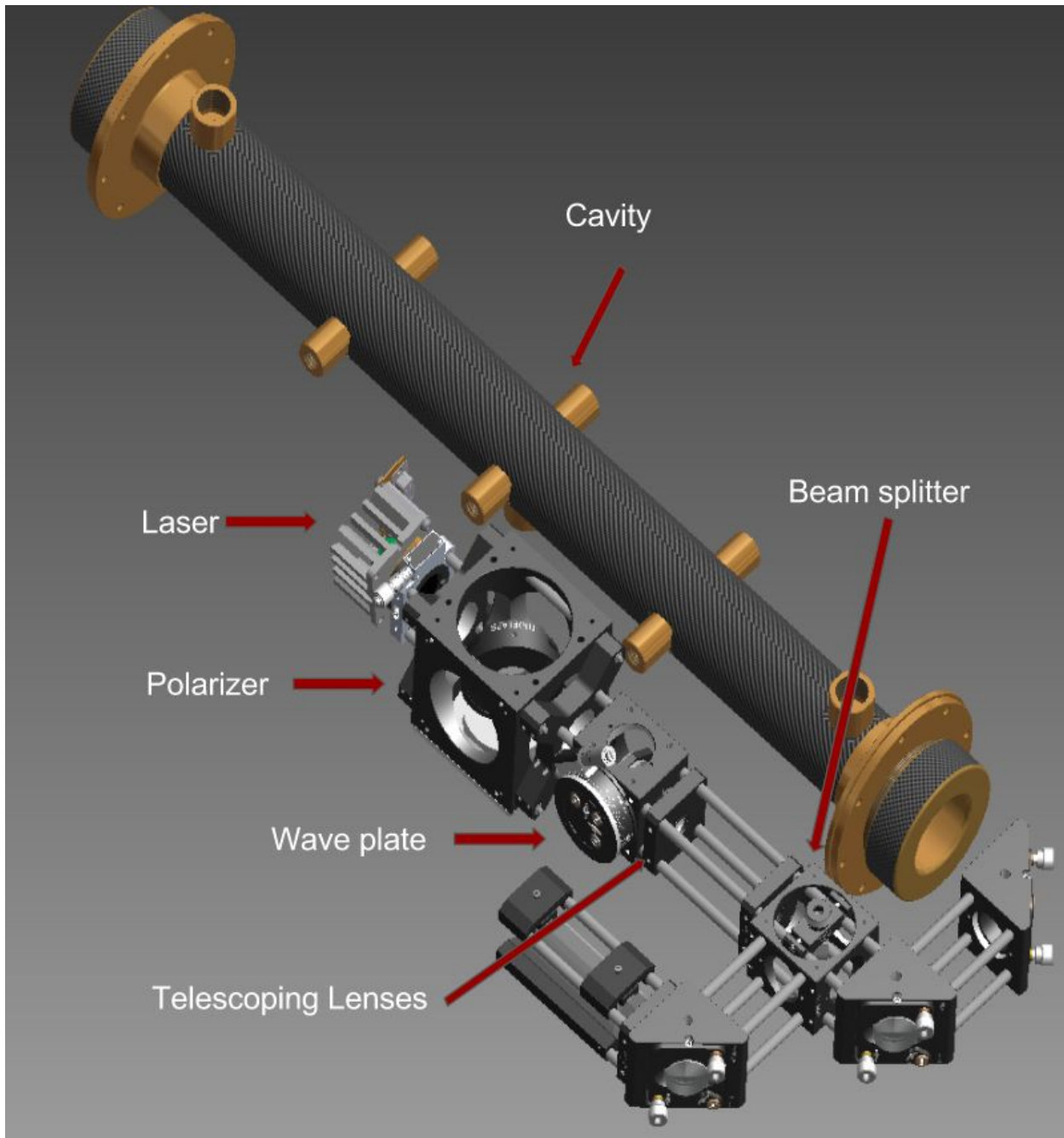


In order to properly steer the laser beam from the beam splitter into the etalon crystal and the cavity we used three KCB1 - Right-Angle Kinematic Mirror Mounts - one to direct the laser into the etalon and two to reverse the direction of the laser and aim it properly into the cavity in order to make the system more compact for flight restraint purposes.



## SCIENTIFIC REQUIREMENTS & ENGINEERING DESIGN SPECIFICATIONS

Included below is a CAD model of the complete fore-optics mechanical system:

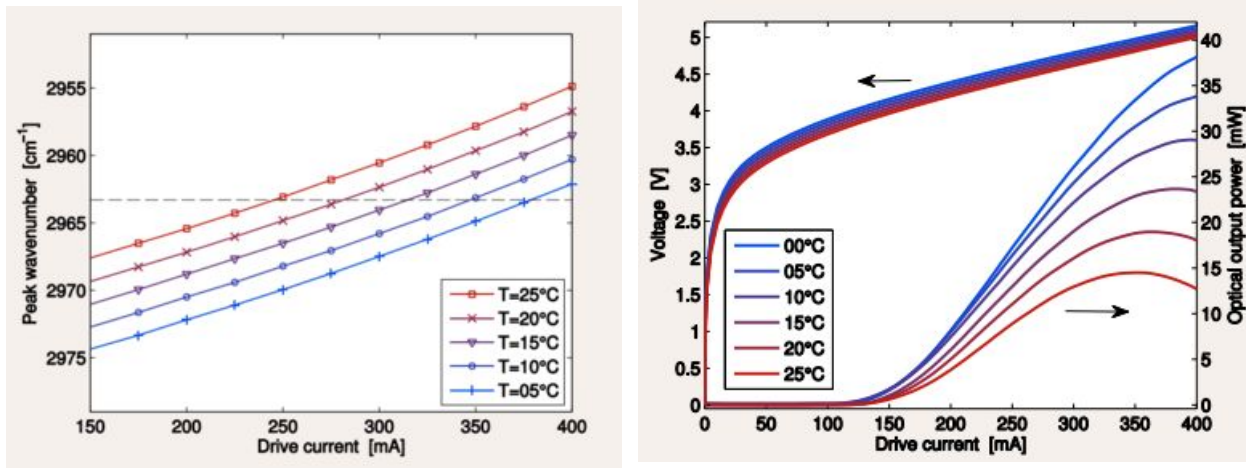


In addition to providing individual rotation adjustment control for each of the crucial fore-optic components, the overall mounting system needed structural durability to withstand any vibrations or shock incurred during the payload's experience of convection currents capable of rising at speeds of 80 m/s. The stainless steel rods and 30 mm cage system ensure that all of the individual mounts for each optical component are mechanically grounded together and locked into place. Essentially the entire fore-optics system becomes one opto-mechanical piece that, once aligned, maintains correct orientation within itself. However, the crucial component to the

functioning of the ICOS system is the correct aiming of the laser into the cavity. To prevent any risks of misalignment in flight, we designed the modular cage system for a single-point attachment to the cavity. By mounting the fore-optics to the cavity at one stable location we ensure the alignment of the optics, laser beam, and cavity despite and in-flight disruptions. Although time did not permit the design of the connection between the fore-optics cage and the cavity, this single-point attachment capability provides a simple solution to ensuring correct laser alignment for maximum effectiveness of the ICOS system.

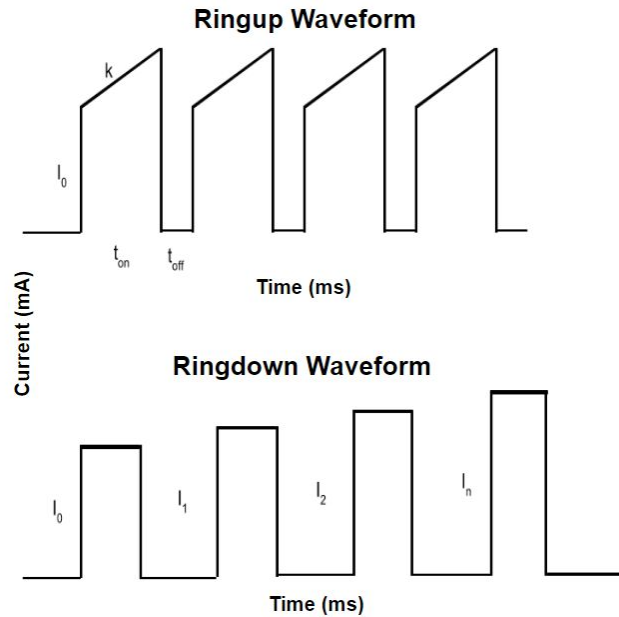
### 3.4.4 Laser Driver

In order to have fine control over the output wavelength of the laser, a laser driver system is vital, providing a means to actually control the wavelength of the laser. The wavelength spectrum of the beam produced by the ICL will be chosen experimentally after testing with the detector. The final instrument is controlled by changing the current driven through the laser - our laser driver system is designed with this in mind, changing the drive current of the laser to change the laser's wavelength. In addition to the laser drive current, the wavelength of the laser beam is extremely sensitive to variations in temperature, and it is extremely important that the temperature of the laser is kept reasonably static. In order to be able to function, the laser also needs a certain compliance voltage at various currents - our laser driver needed to be designed with this in mind, ensuring that there is a large enough voltage drop across the laser.

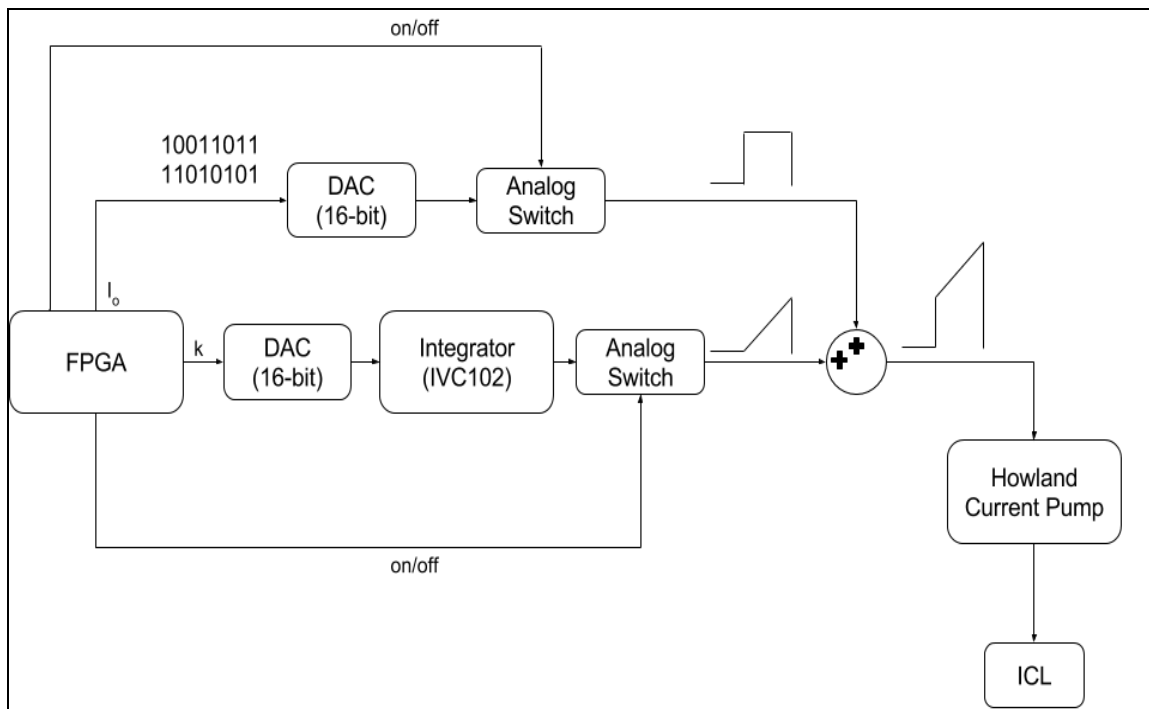


Our laser driver was designed with the ability to produce two particular current waveforms that provide different methods to control the laser's operation. The first - our ringup waveform - allows the laser wavelength to be swept along some pre-defined interval. This behavior allows collection of absorption data within a particular spectrum of interest that the laser can produce. The second - our ringdown waveform - drives the laser at one specific wavelength, allowing observation of the instrument's response at a particular wavelength. For both waveforms, operation at zero current is important to gain a baseline of the detector response

with which to compare results against. The laser driver was designed with the intention to run the waveforms at a frequency of 1kHz - in order to collect sufficient data - and at a rise/fall time of at most 1us - in order to ensure the laser driver is capable of operating faster than the detector.



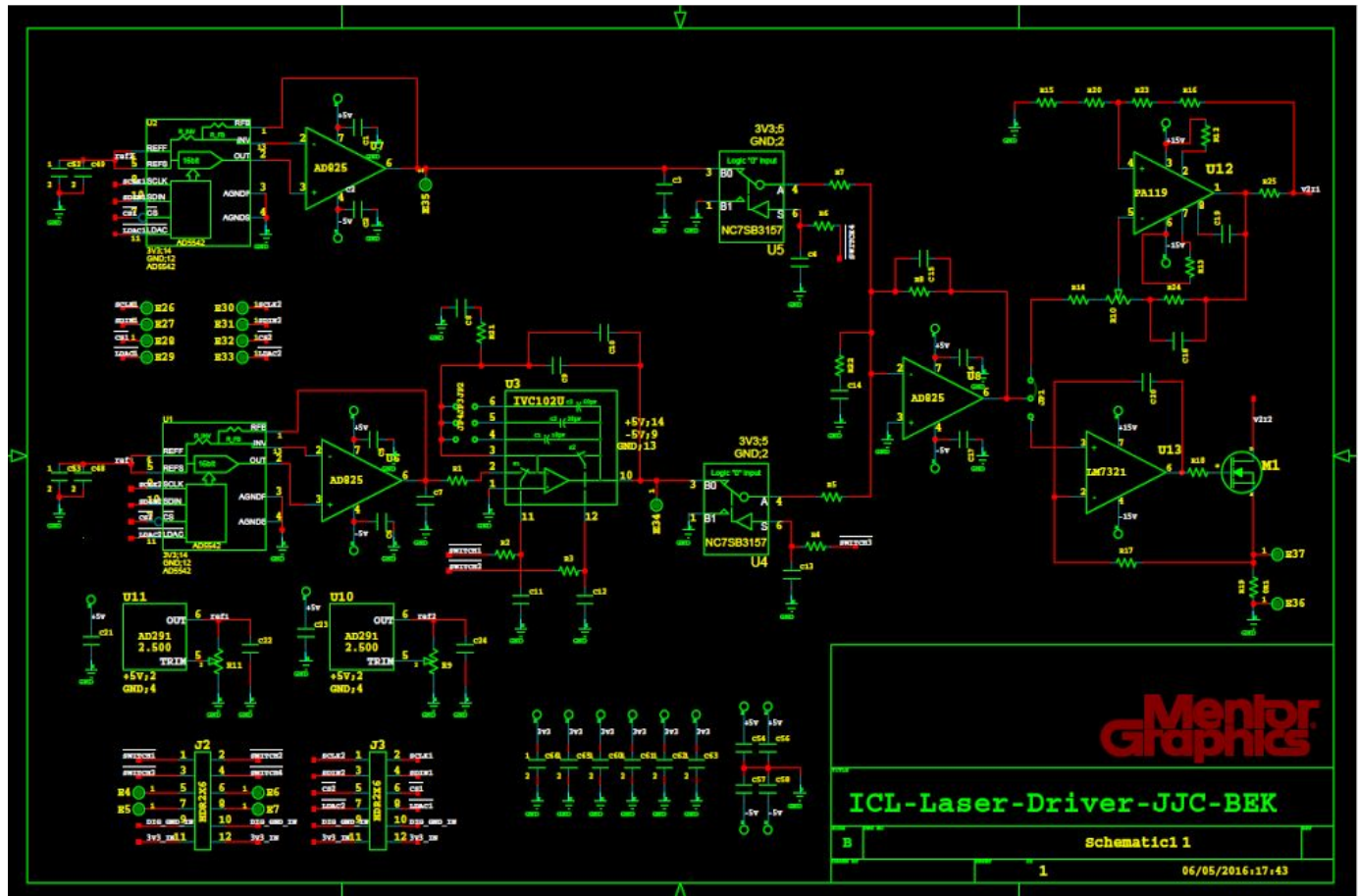
### 3.4.4.1 Design and Schematic



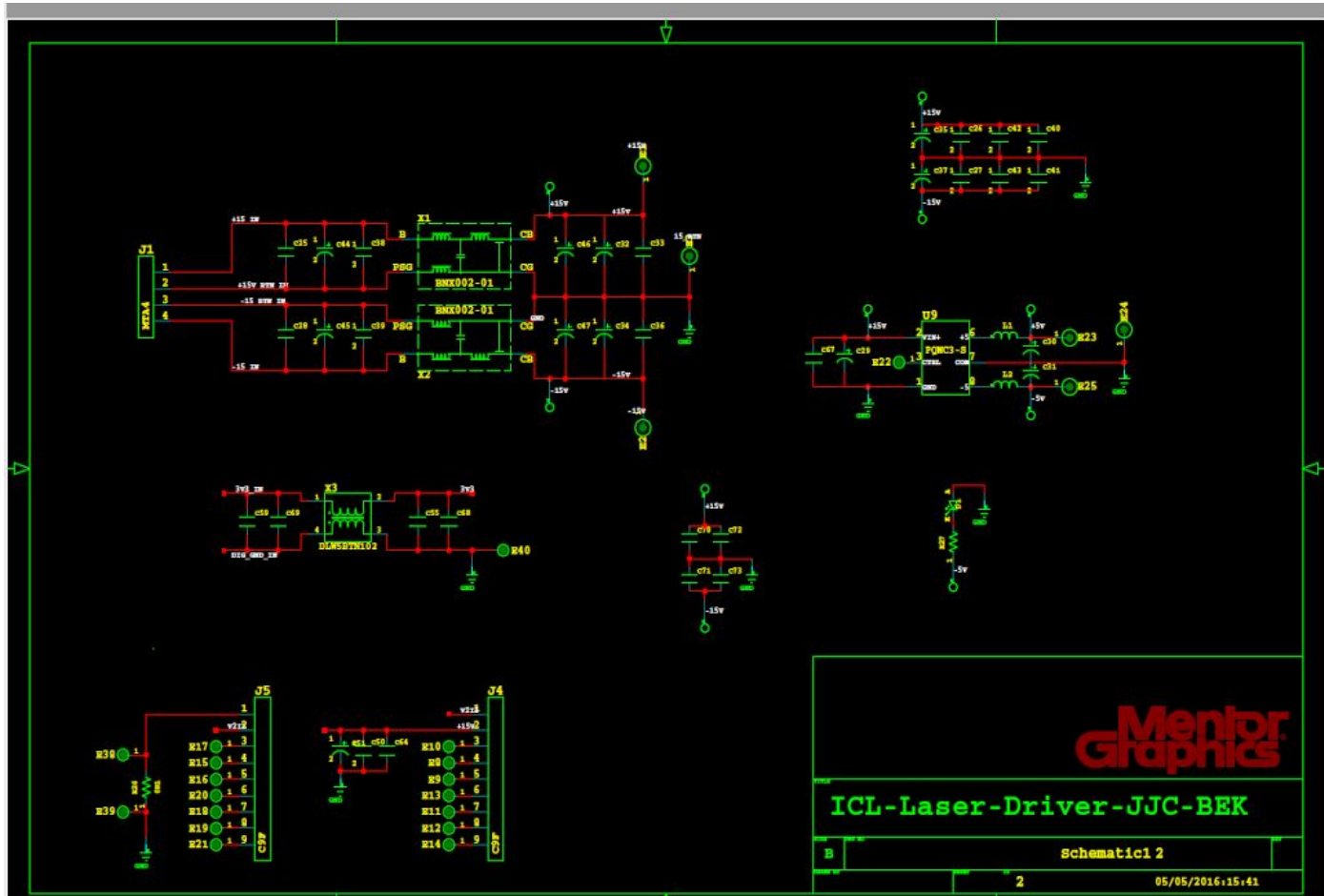
Above is the block diagram of our laser driver system, annotated with waveforms in order to demonstrate how the relevant waveforms are produced. An FPGA allows for

programmable control over the various properties of the current waveforms driving the laser, while providing the necessary low latency to produce precise waveforms. The FPGA also controls a pair of analog switches, allowing control over whether certain parts of the circuit are producing portions of the waveform or not. Additionally, the FPGA feeds the inputs of two separate DACs - necessary to convert the digital signal output by the FPGA into a usable, corresponding analog signal.

Each of the two DACs produces a voltage offset corresponding to the sixteen bit sequence output by the FPGA. One of these voltage offsets is used to offset the final waveform by some amount, while the other voltage offset is used to control the slope of a ramp waveform, produced by an integrator component. As mentioned earlier, each of these two waveform components can be individually controlled directly by the FPGA through the use of analog switches. In order to be able to produce the ringup waveform, each of the two components is summed together. This does not impede the operation of the laser with the ringdown waveform,



since we can control whether the ramp or offset components are present in the final waveform.



The resulting waveform once summed needs to be converted from a voltage signal to a current signal in order to actually drive the laser properly. Our preferred method for voltage to current conversion is the use of a Howland current source - a classic voltage controlled current source perfect for this application. The resulting current waveform can then be used to drive the ICL.

As can be noted from our schematic, an additional voltage to current converter is present, another design (courtesy of Jim MacArthur) we wanted to have present on a prototype board. The secondary design uses an n-channel MOSFET directly controlled by an op amp to convert the voltage signal into a current signal across the load (laser). A potential strength of this design is a greater flexibility with choice of op amp, since the MOSFET is the device actually driving the laser and not the op amp. However, its bipolar operational capabilities are questionable, and certainly subpar when compared to the Howland current source. On the other hand, the Howland current source does limit the choice of amplifiers to large power amps that can handle heavy power dissipation.

In order to avoid the need to re-wire connections to the voltage to current converter if current needs to be driven in the negative direction - say the laser is plugged in backwards - we

decided to use the AD5542 DAC. This particular DAC can output both positive and negative voltages with the addition of an inverting amplifier placed along the output and specialized feedback pins of the part.

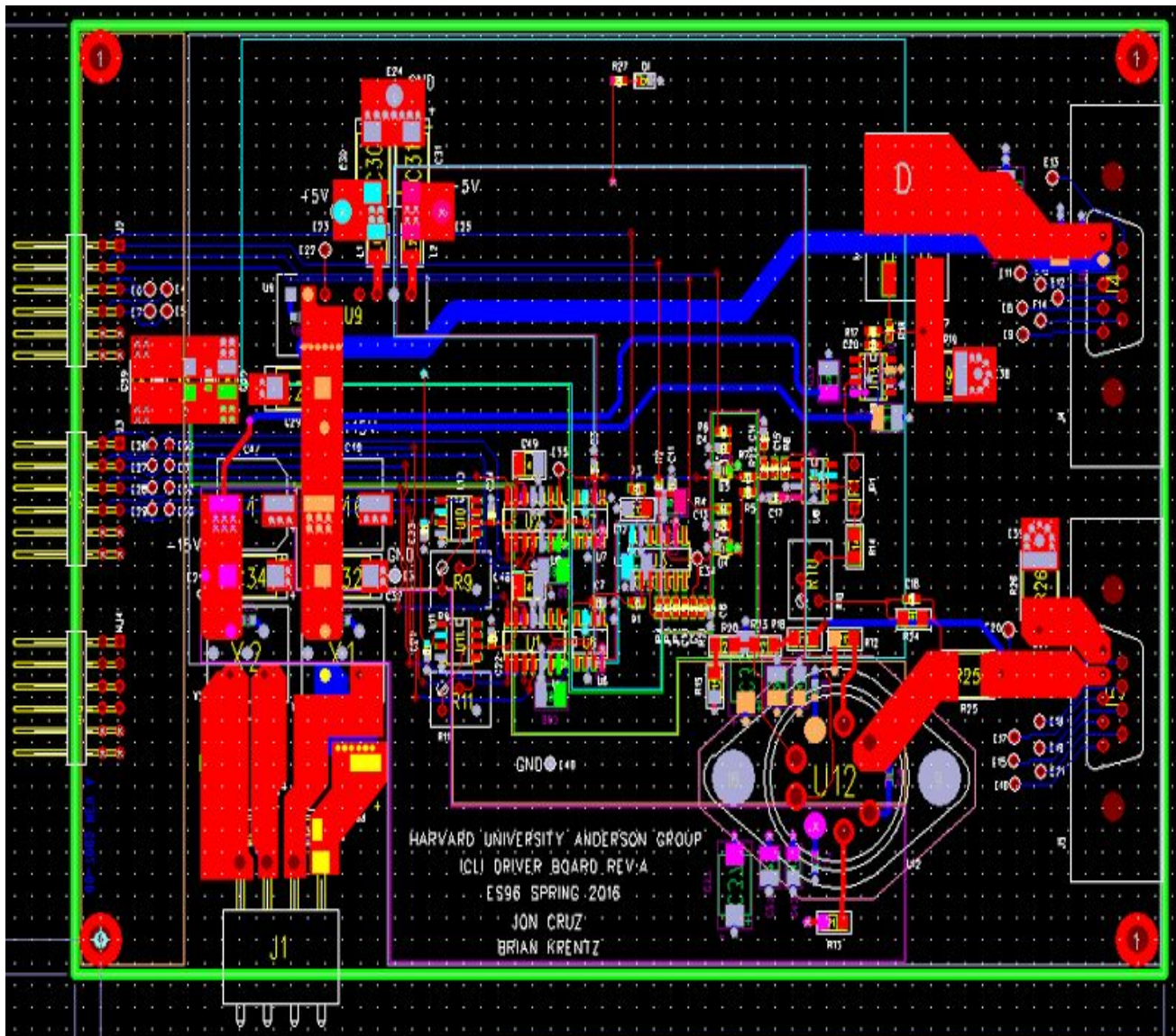
Originally, we intended to design the laser driver with separate grounds for the analog and digital components, as is common practice. However, after several schematic iterations, we ultimately decided to keep things simpler by using a single ground for all of the components. A common mode choke 3.3V and digital ground from off-board filter out differential noise on the power lines, while passing common-mode signals, allowing the use of the same ground for all components.

The summing functionality from the driver block diagram is implemented through the use of a simple summing op amp circuit. The PA119 was chosen to be the op amp used within our Howland current source - it is a good power amplifier with the desired slew rate and power specifications. The PA119 also has the added benefit of integrated overcurrent protection through the use of external resistors. The LM7321 was chosen for our secondary voltage to current converter as an op amp good at driving MOSFETs and within our slew rate specifications. The IR510 MOSFET was chosen for our secondary converter due to its ability to handle the required currents and low capacitance.

The final design will likely need to incorporate protection and sensing circuitry near the laser to prevent accidental destruction of the laser and to send relevant diagnostic readings back to the flight computer. Our prototype incorporates no protection, except for what is integrated in our components and measures only the voltages across relevant resistors for sensing purposes.

#### 3.4.4.2 PCB Layout

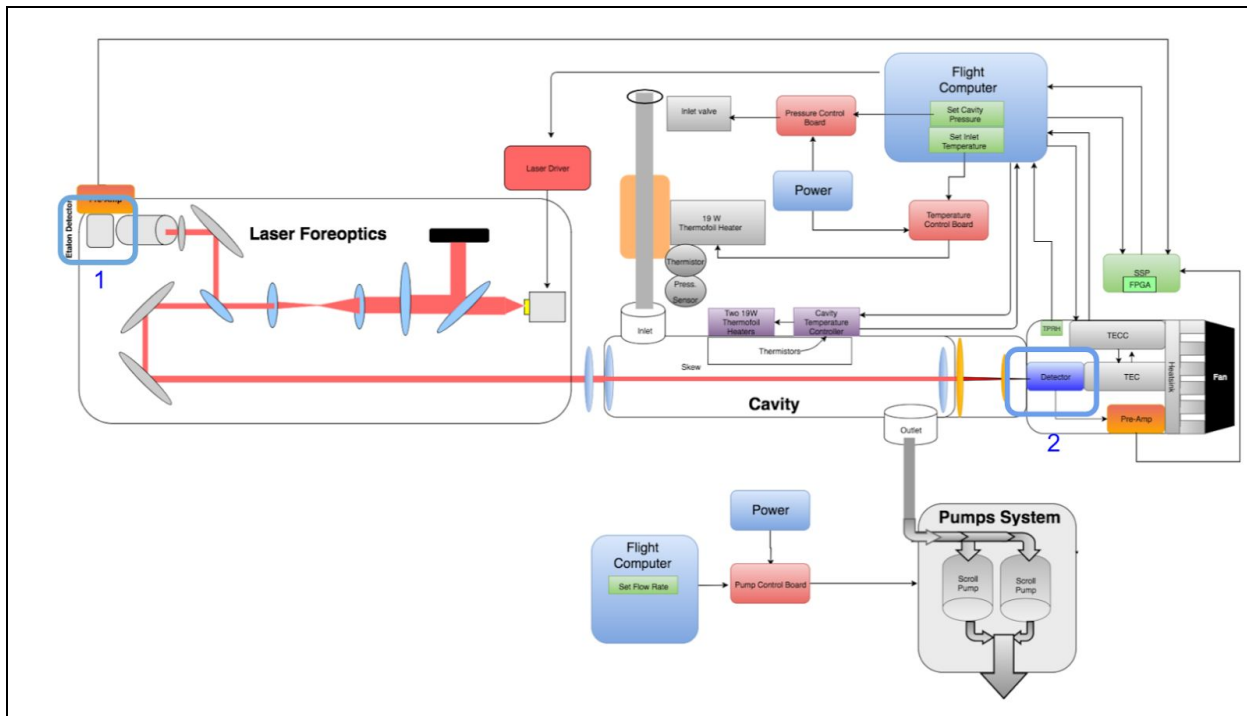
With significant assistance from Marco Rivero and Roy Laurent (an outside PCB designer) we designed a prototype PCB for our laser driver system. In general, the inputs are towards the left of the board, with the outputs towards to right of the board - following the general scheme of our schematic. The PCB has four layers, a top, bottom, signal, and ground layer, and was designed with the intention to keep noise to a minimum. Space for a heat sink on the PA119 was also specified and indicated on the board.



## 3.5 Detector Systems

### 3.5.1 Subsystems

The HCl detecting instrument has two separate detectors--one that measures the IR laser beam before it enters the ICOS cavity (1) and another, more precise detector that measures fluctuations in signal that exits the cavity (2).



These are both photovoltaic detectors that act as passive elements within the circuitry that handles signal from the laser and outputs a recordable measurement. When IR light enters the detector, the inherent resistance of the detector is altered--this is the measurable signal of our system. The researchers harnessed the signal by running a bias voltage through a circuit in which the detector is in a voltage-splitting configuration. This allowed for a voltage signal to be both buffered and magnified with a pre-amplifier, which could then be passed to a signal processing board, or an SSP.

#### 3.5.1.1 Optical Alignment

In both lab setup and proposed flight setup, one of the most important concepts to keep in mind is the alignment of our detector system. As determined experimentally, our detectors have limited acceptance angle, and our post-optical lenses need to be precisely placed so that the signal is correctly handled into the 2mm x 2mm detector plate. To do this, we plan to utilize Thorlabs, Inc. mounts and alignments. These provide us with an already-optimized setup of connecting elements of the detector in alignment with the rest of the system. As schematics of

these parts are well-documented and thoroughly dimensioned, we are also able to machine custom parts to hold unique parts such as detectors and heatsinks, which can then be interfaced with the rest of the Thorlabs caging.

### 3.5.2 Etalon Detector

#### 3.5.2.1 Design Requirements

##### 3.5.2.1.1 Wavelength Sensitivity

In order to have a high signal:noise ratio and reliable measurements of the concentration of the species, both detector systems have to be able to detect light and produce strong signals at the range of wavelengths over which our ICOS system is scanning. Detectors, made of various materials and operating over a range of temperature conditions, are well characterized with regards to their sensitivity. This measure, referred to as a detector's specific detectivity, does vary among manufacturers, but can be roughly estimated using Figure.

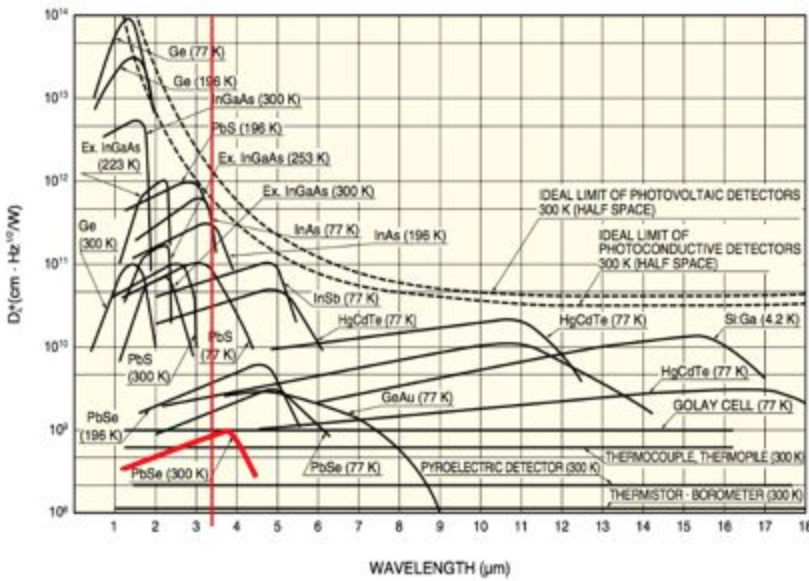


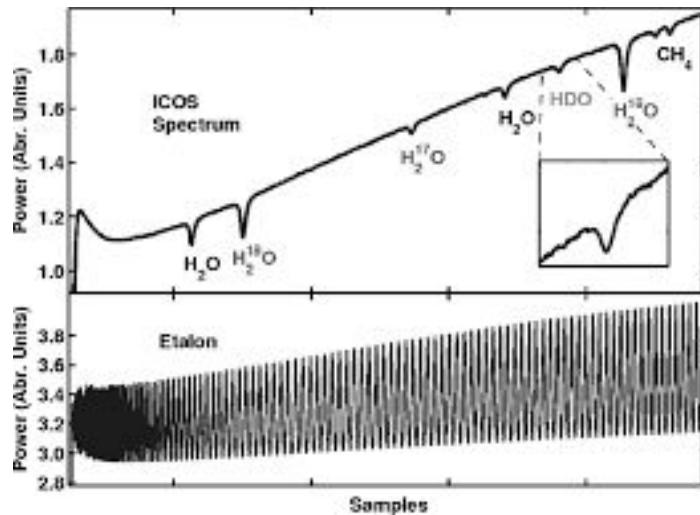
Figure. Specific Detectivity plotted against wavelength of light.

The red vertical line indicates the wavelength of light at which our system will be centered ( $3.375 \mu\text{m}$ ), and the red curve is the specific detectivity curves of the detector material that we ultimately selected. Though we would ideally prefer detectors that are highly sensitive at the given wavelength of light, we may select a detector with relatively low sensitivity (the red curve;  $\text{PbSe}$  at room temperature) to detect the signal at the end of the etalon system. We expect the etalon signal to be attenuated roughly by a factor of 100 from the laser's full power; this light intensity should be sufficient to produce a very distinct signal, far above the background noise signal.

### 3.5.2.1.2 Speed

The speed of our etalon subsystem is characterized by the etalon and the laser driver. The etalon detector must be faster than the system in order to ensure that any features that we observe are characteristics of the system and not simply an electrical lethargy imposed by our detector system.

The speed of the etalon system is dictated by the laser driver, and our system's need for accurate detection of etalon fringes. As our laser driver sweeps through its wavenumber range, the photons pass through the etalon, where they undergo constructive and destructive interference, as pictured in Figure.



*The deconvolved signal observed at the end of a detection setup with water molecules (top) and the signal observed at the end of the etalon setup (bottom). The etalon's fringes are caused by constructive and destructive interference, and allow for the accurate determination of the distance between peaks in the deconvolved spectrum.*

The etalon's fringes are crucial for the success of the instrument. The distance between fringes, known as the Free Spectral Range (FSR), is constant and is a property of the etalon material. Having a reliable scan of the etalon fringes, matched to the spectrum that will be obtained from the post-cavity detector, allows for the accurate and precise determination of the wavenumber difference between peaks shown in the spectrum. These peaks can then be matched to the peaks given by published lab spectra of the known species in the sample, which conclusively would prove the presence of the species of interest and lend credence to claims made about the concentration of the species.

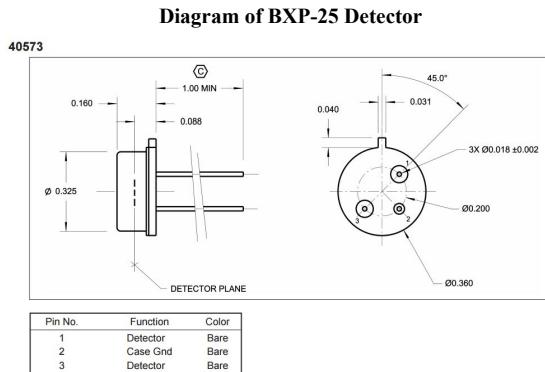
Given that our laser will sweep over  $1\text{cm}^{-1}$  in 1ms, and that the length L of the etalon is 7.62cm, and the index of refraction n is 4, the time between two subsequent peaks would be:

$$\frac{t_{full-sweep}}{\Delta\nu_{wavenumbers}} * FSR = \frac{t_{full-sweep}}{\Delta\nu_{wavenumbers}} * \frac{1}{2nL}$$

The resulting value of  $16\mu\text{s}$  is the rough time-scale over which we want the detector to be responsive; ideally, we desire the detector to be a factor of 10 faster than the time over which the fringes will evolve.

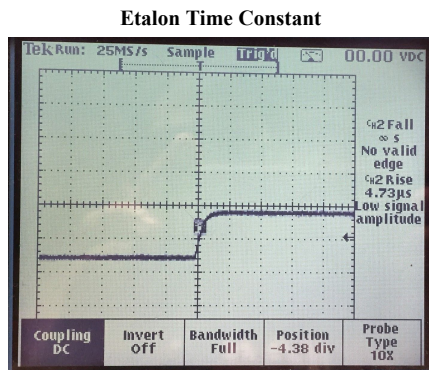
### 3.5.2.2 Detector Selection

The chosen etalon detector was a BXP 25 from Optodiode. The detector is a  $2\times 2$  mm PbSe photoconductive uncooled detector. It has a TO-5 3-pin pinout package. The detector was specified to have a  $2.0\ \mu\text{s}$  time constant and peak sensitivity at wavelength  $3.8\ \mu\text{m}$  as well as a dark resistance of  $100\text{-}300\ \text{k}\Omega$ .



### 3.5.2.3 Characterization

In the lab we were able to characterize the etalon detector in order to verify the specificity sheet. The detector was placed in an IR void area and a dark resistance of  $300\ \text{k}\Omega$  was measured. Using a JPL53\_4 waveform from the laser set-up we measured the time constant of the detector. With 7 V across the detector and a pull-up resistor of  $100\ \text{k}\Omega$  we measured a  $2.0\ \mu\text{s}$  time constant based off of a  $4.73\ \mu\text{s}$  rise time.



### 3.5.3 Post-Cavity Detector

#### 3.5.3.1 Design Requirements

##### 3.5.3.1.1 Wavelength Sensitivity

In much the same manner as was used to determine an appropriate detector for the etalon subsystem, the below Figure was used to identify candidate post-cavity detectors.

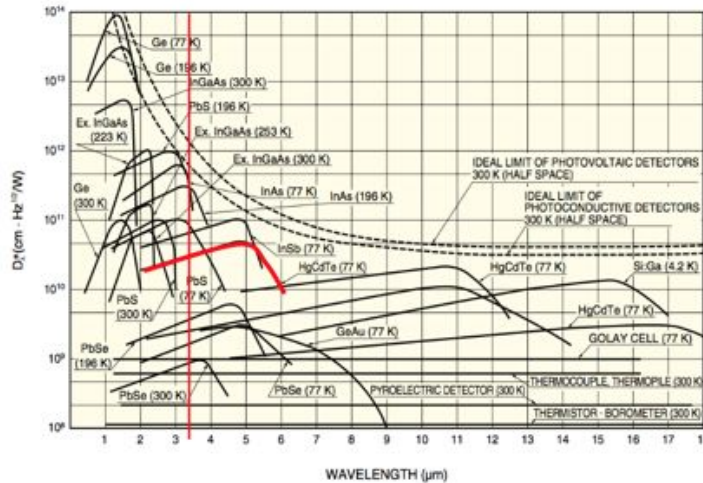


Figure. Specific Detectivity plotted against wavelength of light.

The post-cavity detector expects to see a light intensity attenuated by at least a factor of 100,000 compared to the full-power of the laser, and so must be more highly sensitive than the etalon detector, which expects to see light intensity attenuated by about a factor of 100.

##### 3.5.3.1.2 Speed

The speed of the cavity system is dictated by its geometry and the reflectivity of our mirrors. Just as with the etalon detector, the post-cavity detector must be faster than the cavity time constant in order to ensure that the features gleaned from the spectrum can unequivocally be attributed to the spectrum of the species inside the cavity, and not an electrical issue of the detector.

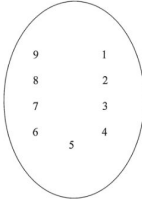
The speed of the post-cavity detector is dictated by the ring-down time of the cavity. The ring-down time, which is the time over which the light is reflected in the cavity and the signal decays, is dependent on the effective path length, which is in turn dependent on the reflectivity of the mirrors. Given reflectivities of between 99.992%-99.994%, the ringdown time constant is between 17 $\mu$ s-21 $\mu$ s. In order to obtain reliable spectra and ensure that artifacts measured by the detector are consequences of the chemical species and not any electrical effects of the detector, we would hope to have a detector with a time constant up to 10x smaller than the ring-down time.

#### 3.5.3.2 Detector Selection

The cooled detector we chose was an MCT-4.5-TE4-2.00 from InfraRed Associate.. It is a 2x2 mm Mercury Cadmium and Tellurium photoconductive detector with a TO-66 8 pin package. The detector is mounted with a 4 stage TEC setup to cool it to the required temperature

of -75C. It is specified to have a time constant of 2  $\mu$ s with a resistance of 1.2 k $\Omega$  with 7 V across the detector.

TO-66  
BOTTOM VIEW

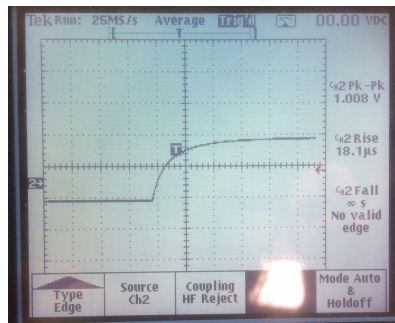


PIN 1 THERMISTOR  
PIN 2 MCT DETECTOR  
PIN 3 n/c  
PIN 4 COOLER NEGATIVE  
PIN 5 n/c  
PIN 6 COOLER POSITIVE  
PIN 7 n/c  
PIN 8 MCT DETECTOR  
PIN 9 THERMISTOR

### 3.5.3.3 Characterization

In the lab we were able to characterize the cooled detector in order to verify the specificity sheet. The detector was placed in an IR void area and a dark resistance of 1.2 k $\Omega$  was measured. Using a JPL53\_4 waveform from the laser set-up we measured the time constant of the detector. With 7 V across the detector and a pull-up resistor of 100 k $\Omega$  we measured a 8.7  $\mu$ s time constant based off of an 18.1  $\mu$ s rise time. This was significantly off from the specified number.

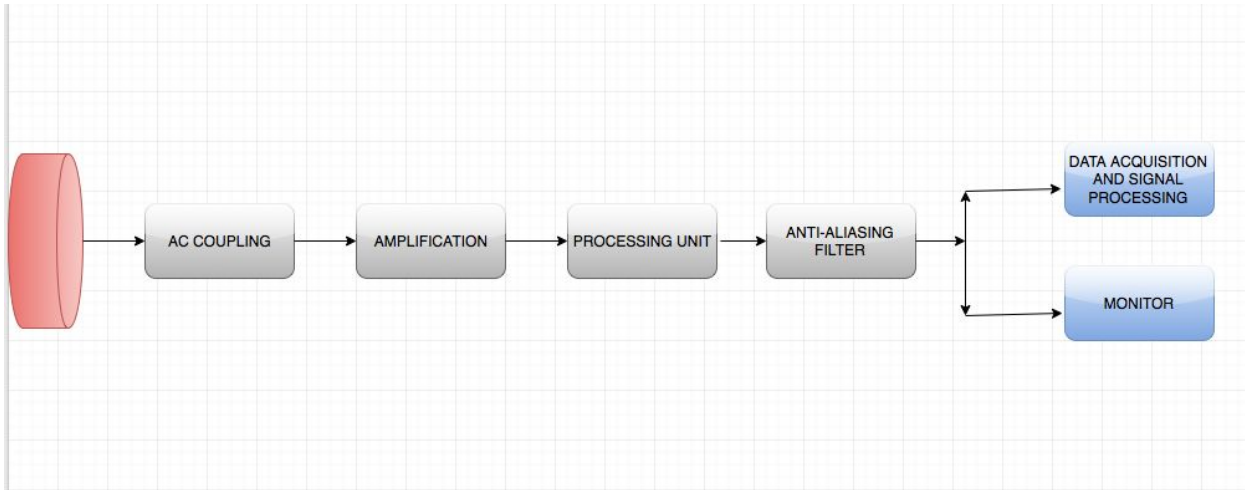
Etalon Time Constant



### 3.5.3.4 Signal Amplification

The signal that comes out of the detector is small- in the order of microamps. It also contains a substantial amount of noise that needs to be eliminated so that our analysis at the end gives an accurate depiction of what needs to be measured in the first place. Hence before our signal is actually analyzed, we need to pass it through a preamplifier. Designing the amplifier also entails knowing the specific properties of the detector being used. This means we have to design parameters like impedance, noise and bandwidth that matches the detector.

### 3.5.3.4.1 Design Schematic



*Pre-Amp Schematic*

*This schematic shows all the stages of the pre-amplifier. Each stage is essential when it comes to producing a clean amplified version of the signal. Each stage will now be explained in brief detail.*

#### AC-Coupling

Our detector is an MCT hence it is photo-conductive in nature. Hence for it to be able to work (or being excited), it needs to be biased. Biasing the detector gives a dc bias that becomes part of noise. This dc bias is removed by passing the signal through a blocking capacitor and this process is called ac coupling. Another method of eliminating the dc bias is called baseline restoration. By so doing a DC path is maintained.

#### Amplification

Once we have a signal that is free of bias, we pass it through the amplification stage. In this stage we have an amplifier of variable gain. In choosing a specific amplifier to use, the amplifier chip to be used needed to have a high bandwidth, small input bias current, high gain, low input capacitance and high input impedance. However in choosing the chip, a lot of trade off has to be done between the input bias current and bandwidth since the amplifiers with high bandwidth has a larger input bias as well. Hence an AD8065 was ideal for this implementation.

#### Processing Unit

This unit basically contains a unit buffer that reproduces the input signal as it is. The buffer used here is a one input to two outputs component. These two outputs are exactly the same. One of these outputs is then passed through an inverting amplifier. This inverting amplifier only serves to invert the signal and not really amplify it. A comparison between this output and

the other output from the one to two buffer that was not inverted will help to eliminate any noise that might have been picked up as our signal was passing through the different stages that we have in the pre-amplifier. Noise that the signal contained from the detector and the noise it might have picked up is consequently eliminated.

#### Anti-Aliasing Filter

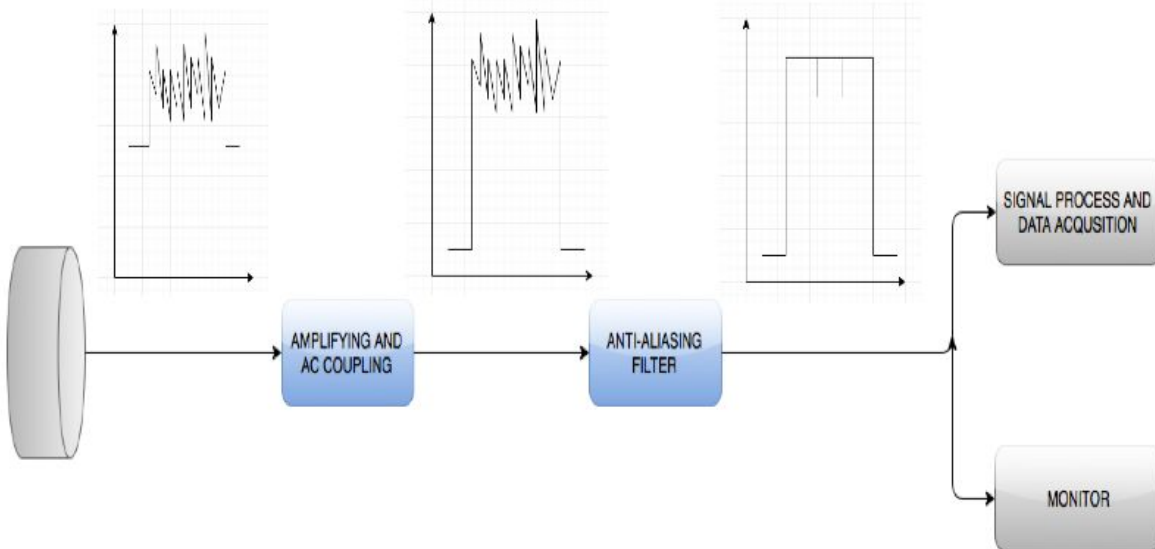
An anti-aliasing filter is a low pass filter that prevents high frequency signals from aliasing with our signal. This helps clean up our signal more as well as producing a fine tuned and perfectly sampled signal.

#### Outputs

The signal that comes out of the anti aliasing filter is clean and amplified and ready for be analyzed. The signal is split into two. One signal goes to the data acquisition and signal processing unit. This is the flight computer system. The other signal goes to the monitor, which in the most basic form is the oscilloscope in the lab. This is the signal we use for our preliminary testing and ensuring that the pre-amp is working as it should be. Subsequent changes to our pre amplifier circuit are made after testing this signal.

#### **3.5.3.4.2 Condensed Schematic**

A look at the signal as it comes out of each stage helps understand this process clearer.



The signal from the amplifier is small, noisy and has a DC bias. The one from the Amplifying and AC coupling stage has been amplified and the DC bias is removed. However it's still noisy. The signal from the Anti-Aliasing filter is the cleaned signal that is ready for processing.

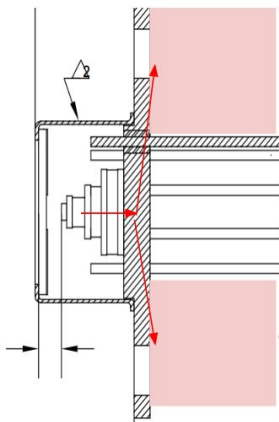
### 3.5.3.5 Thermal Management

The differentiating factor between the etalon detector and the cooled detector, obviously, is the cooling of the detector. As we require a much more precise and powerful measurement from the detector following the ICOS cavity (due to attenuation through the reflections between the mirrors of the ICOS), our initial detector choice (MCT-4.5-TE4-2.00) has a much higher D\* (specific detectivity) than our etalon detector. This higher detectivity brings problems as well as solutions to our device--while it has the ability to accurately measure the signal that leaves the ICOS cavity, it is also more liable to detect latent IR radiation. Energy in the form of heat is produced by the detector (as it is a resistive element), and has the ability to be transferred through IR radiation.

The way to combat detector noise through IR radiation is through a mixture of both thermoelectric coolers (TECs) and heatsinks. TECs operate through the *Peltier* effect--in short, when current is applied between two conductors of different Peltier coefficient, a cold face and a hot face of the conductors form. This is governed through:

$$Q = (\pi_a - \pi_b)I$$

Where  $Q$  is the heat created per unit time,  $\pi_a$  is the Peltier coefficient of one of the two conductors, and  $I$  is the current that runs through the TEC. This process allows for the local area of the detector to be made into a “cold point.” Energy that could become IR radiation, and by extension, noise, is transferred away from the detector (through conduction) into the casing of the detector. We can amplify the thermoelectric effect through “stacking” multiple TECs on top of each other--below we see an example of a cooled detector that has multiple (3) TECs stacked below a detector:



Figure

However, the TECs only do so much through moving heat to the casing of the detector. As the entire casing is a conductive material, merely conducting heat to the casing of the cooled detector allows for IR radiation of energy to occur and still create noise in the detector’s signal.

This is where a heatsink can be utilized for further energy conduction. When a conductor is placed against the casing, its high thermal conductivity drastically reduces the amount of possible IR radiation near the detector. As copper is both cheap and easy to machine in a laboratory setting, we are using a copper heatsink placed in the red-shaded area in the above figure. This allows for energy to follow a line of conduction (see the red arrow of the figure above) from the detector all the way to the fins of the heatsink.

Once energy reaches the heatsink fins, it is further dissipated via fans attached to the rear of the heatsink. These convectively transfer energy to the surrounding housing.

### 3.5.3.6 Post-Cavity Optics

Immediately following the ICOS cavity, beam pattern of the IR laser can be approximated as a circle of dots with a diameter approximately equal to that of the cavity. However, we need to focus this pattern onto our detector, a 2mm x 2mm plate, while maintaining as much of the signal as possible. Utilizing a software algorithm created by Norton Allen, the researchers determined that utilizing two lenses would provide optimal focusing onto the detector. Zinc selenide lenses also provide optimal wavelength transmission through the lenses.

We also determined that one lens needed to be situated directly following the ICOS mirror. This is due to the rear mirror being plano-concave--when the IR beam is transmitted through the mirror, it angles away further away from the detector, creating a larger diameter of the beam pattern. We place one lens directly after the ICOS to immediately begin angling the signal toward the detector. We then have a second lens roughly 40%-60% between the end of the ICOS and the position of the detector. This allows the signal to reach the detector at a shorter distance from the end of the cavity, reducing the footprint of the overall instrument.

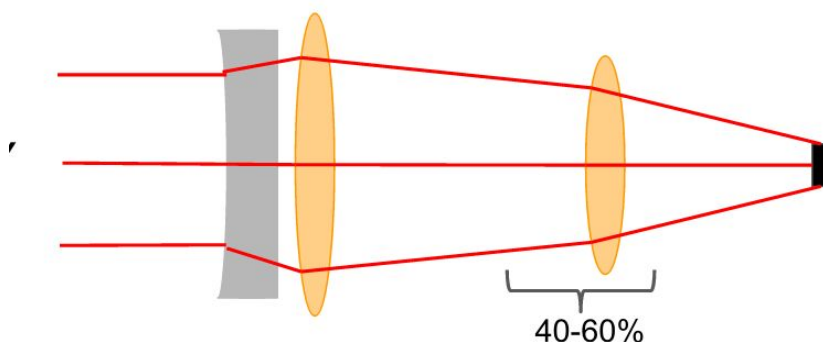


Figure: Here we see the general setup of the focusing lens setup--the plano-concave mirror of the ICOS cavity is the grey shape furthest to the left, increasing the diameter of the beam pattern. The two lenses that follow the cavity focus the signal onto the detector, the small black shape on the right hand side.

Our researchers have decided to purchase 3 different lenses: ZC-PM-25-150, ZC-PM-38-200, and ZC-PM-38-63. The PM in each stands for positive meniscus, the first

number indicates the diameter of the lens, and the final number indicates the focal length. We will be utilizing two of the three lenses to focus signal onto the detector--the optimal pair will be determined via experimentation once all lenses arrive.

#### **4. IMPROVEMENTS AND NEXT STEPS**

##### **4.1 Improvements**

Throughout the semester with ES96, students have learned about teamwork, iterative design and practical research through a real engineering challenge. By designing, testing, and experimenting on a prototype device for HCl detection in the upper stratosphere, students gained both hard and soft engineering skills valuable to a future career in engineering.

While the Anderson Group at Harvard University has created Integrated Cavity Output Spectroscopy devices for years, this is the first successful prototype ever created to measure HCl. Many improvements were made to this device compared to older models used to measure components of the stratosphere such as water, ozone, BrO, and others. Some improvements to the design, broken down by subsection are listed below.

*Pump:* lighter, smaller pump. Higher flow rate than older ICOS systems

*Fore optics:* Now use independent mounting for all components, telescope to decrease mirror spotting, and a fully incorporated, minimized cage system for modularity and ease of assembly

*Laser Driver:* simplified to one board, faster response time to voltage changes

*Cavity:* smaller, reduced weight (hardware), updated locations of temperature probes

*Simulation:* New MATLAB cavity script, refined ray tracing model

*Sensing:* Pressure feedback loop for flow control

*Detector:* Cheaper, faster etalon detector

This updated model of ICOS will continue to be used in future systems. Do adapt the current model to other airborne species, many components can remain the same. The laser, mirrors, cavity length, and detectors will need to be retrofitted to meet the specifications of the species in question, but the overall setup and design of the system can very much be kept constant. These improvements will allow for an overall lighter, more efficient system, more closely specified to the species in question. In the long run all of these improvements will lead to a more effective and accurate ICOS device.

##### **4.2 Future Steps**

In April, 2016, students were notified that the HCl detection device had been accepted into the NASA Undergraduate Student Instrument Project. This program guarantees funding, mentorship, and a flight opportunity in the coming year through NASA. With the boost of this grant, the project will continue in its development from the current prototype stage into a flight ready instrument by the spring of 2016. In order to reach that stage of development, students will

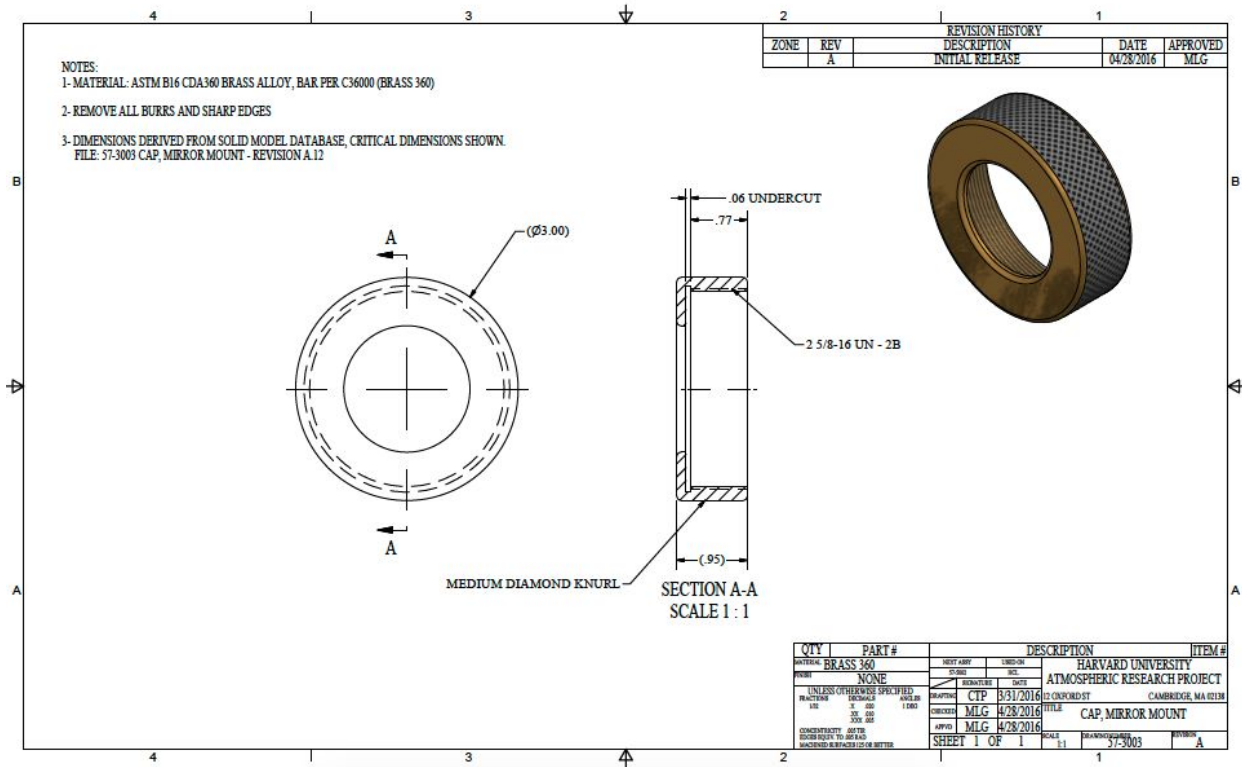
continue to work on the instrument throughout the summer as well as next year. In summer of 2016, 5 students will work in the Anderson Group to begin the transition from a lab bench prototype into a fully contained flight-ready instrument. In the following year, select students will work on the project as a senior thesis and bring the device to completion, readying it for a balloon test flight in Spring 2017 before it launches on the StratoCruiser ASCENA mission at some point in the near future.

In order to bring the instrument from prototype to final flight-readiness, all subsystems will need to be fully contained, tested, compacted, and controlled remotely via the flight computer and radar data. This work includes building pressure vessels for all subsystems, mechanically securing the instrument safely together, reducing any size and weight requirements to meet the ASCENA proposal, and linking all subsystems to the flight computer with new software. While lengthy in its requirements, a great deal of work has already been done in setting up the device to become an instrument ready for its first flight in New Mexico during the spring of 2017.

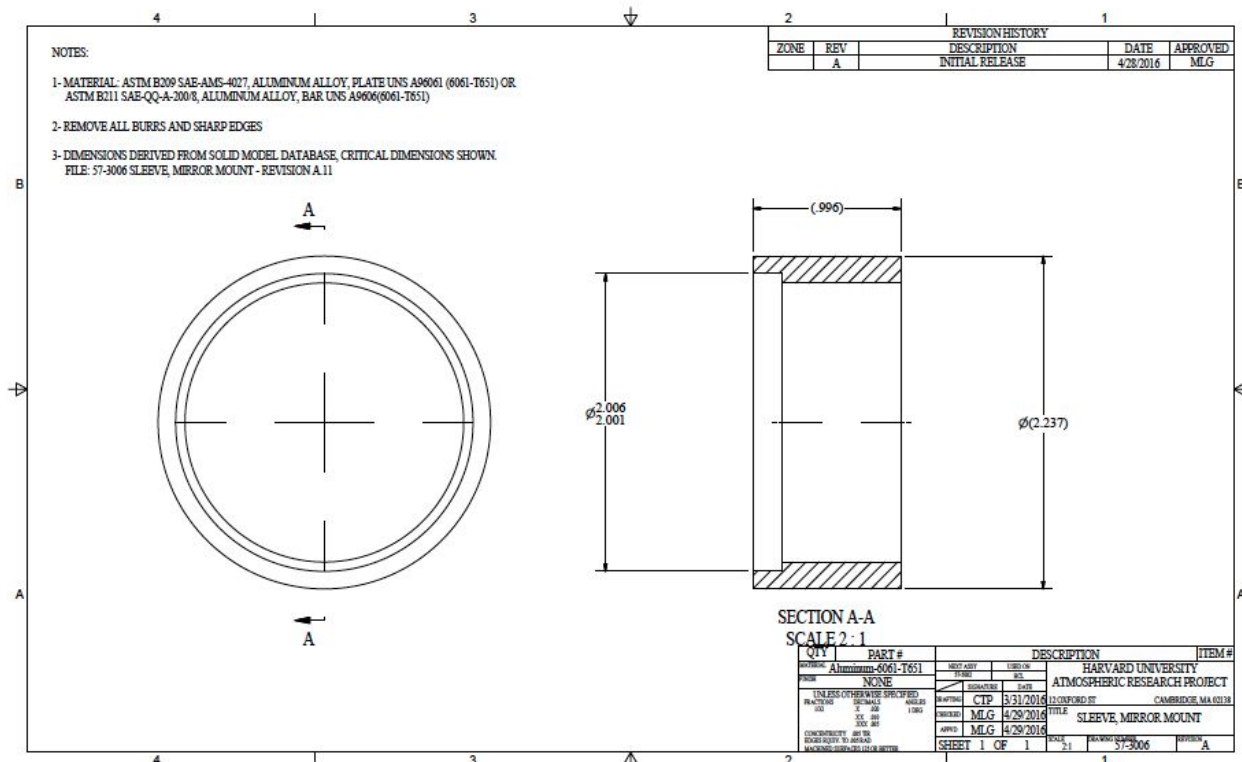
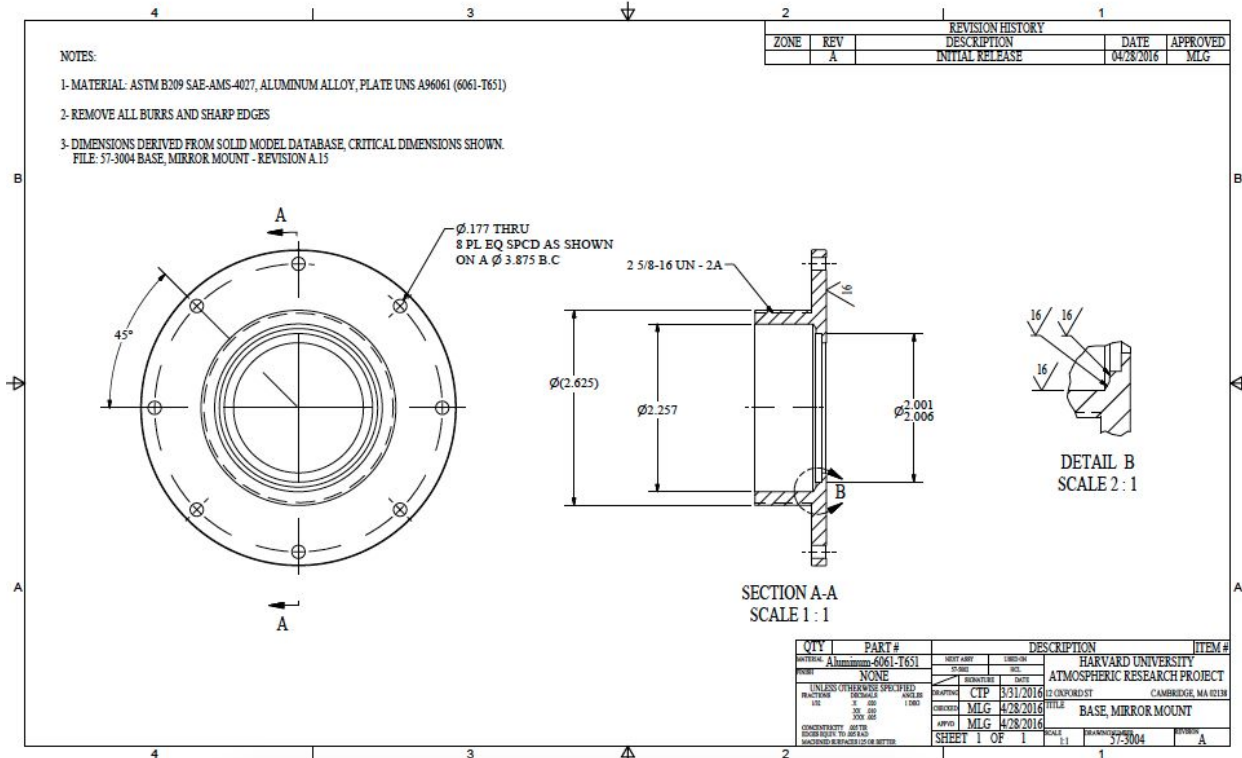
This semester, ES96 has worked with the Anderson Group with help from NASA to design and implement a prototype for a hydrogen chloride detection instrument for lower stratospheric monitoring. As stated earlier, the increased catalyzation of inorganic chlorine over the midwestern United States is leading to the depletion of ozone in the stratosphere. This ozone depletion leads to proven decreases in human health. It was the goal to create a device to help learn more about this phenomena and with numerous technological advances, the class made major steps towards helping solve this pressing global issue. This semester, the students of ES96 learned that through teamwork, extensive research, and iterative design, it is possible to discover impactful, project oriented solutions to difficult problems. This research will continue and soon be developed into a tool that scientists can use to learn more about HCl in the lower stratosphere.

## 5. APPENDIX

### 5.1 Endcap Drawings



# SCIENTIFIC REQUIREMENTS & ENGINEERING DESIGN SPECIFICATIONS



# SCIENTIFIC REQUIREMENTS & ENGINEERING DESIGN SPECIFICATIONS

